LRP 610/98 July 1998

Papers presented at the

24th EPS CONFERENCE ON CONTROLLED FUSION AND PLASMA PHYSICS

Praha, Czech Republic,
June 29th - July 3rd, 1998

LIST OF CONTENTS

Effect of Localised Electron Cyclotron Heating on Energy Confinement and MHD in TCV

A. Pochelon, Z.A. Pietrzyk, T.P. Goodman, M. Henderson, J-P. Hogge, J-M. Moret, H. Reimerdes, G. Tonetti, M.Q. Tran, H. Weisen, R. Behn, S. Coda, B.P. Duval, I. Furno, F. Hofmann, B. Joye, J.B. Lister, X. Llobet, A. Manini, Y. Martin, Ch. Nieswand, J. Rommers, O. Sauter, W. van Toledo

Y.V. Esipchuk†, A.A. Martynov†, A. Sushkov†

F. Porcelli*

Centre de Recherches en Physique des Plasmas, Ecole Polytechnique Fédérale de Lausanne
Association EURATOM-Confédération Suisse, CH-1015 Lausanne, Switzerland
† Russian Research Centre Kurchatov, 12182 Moscow, RF
**Politecnico di Torino, Italy*

Introduction - This paper reports the effects of localised power deposition on the heating, MHD activity, and confinement in TCV. Initial ECRH studies concentrated on low elongation plasmas, including positive and negative triangularities: this is a necessary step before investigating more strongly shaped plasmas. ECRH power of up to 1 MW at 82.7 GHz (second harmonic X2) was injected, representing up to 14 times the Ohmic power during the heating pulse [1]. When complete, the ECW system will provide 3 MW second harmonic and 1.5 MW third harmonic at pulse lengths of 2 s [2]. For TCV (R = 0.89 m, a = 0.25 m, I_p < 1.2 MA), the nominal field of B = 1.44 T and the frequency of 82.7 GHz place the resonance slightly off-axis on the high-field side (HFS) of the magnetic axis ($\Delta\rho$=-0.16 to -0.2). This allows us to scan the power deposition location on the HFS, above and below the magnetic axis, on a shot-to-shot basis; or, to sweep it during one shot. Sweeping is done using *1)* steerable launcher mirrors (primarily the poloidal angle θ), *2)* vertical plasma translation in the TCV vessel and *3)* radial displacement of the cyclotron resonance by changing the magnetic field.

The *power deposition location* was determined using the soft X-ray response at the EC shut-off (plus Thomson electron temperature profiles); when not coincident with a sawtooth crash, which perturbed the measurement. The maximum of the power deposition location coincides with the ray tracing prediction to within a few percent in normalised radius ρ, as shown in the example of **Fig. 1**. The low sampling rate of 10 kHz causes the measured deposition profile to appear wider due to the large time window needed for the measurement. The location of the maximum, however, is not affected by the window choice.

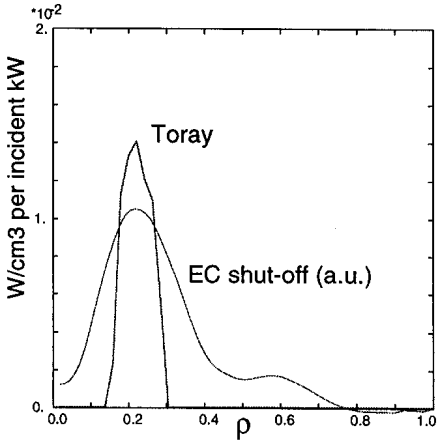

Fig. 1. Typical power deposition from Toray ray tracing (W/cm^3 per incident kW) and from soft X-rays at EC shut-off, as a function of normalised radius ρ.

Absorption location - The absorption location of the EC power strongly affects the resulting central temperature, confinement and sawtooth behaviour, as shown in **Fig. 2**, depicting a B-field scan (0.5 MW). The deposition is swept across the sawtooth inversion

surface (deduced from soft X-ray tomography) on the HFS of the magnetic axis. The *central electron temperature* T_{eo} is maximum for power deposition somewhat inside the sawtooth inversion radius ρ_{inv} (**Fig. 2a**), i.e. towards magnetic axis (R_{res}-R_{inv}>0). The *global electron confinement time* τ_{Ec} (**Fig. 2b**) is relatively independent of the resonance position when heating inside ρ_{inv} and drops when heating outside ρ_{inv}, implying efficient heating requires deposition roughly inside ρ_{inv}. Data in **Fig. 2 a, b**) cover a large range of q_a values: 2.3<q_a<6.7. The *sawtooth period* is maximum for a deposition slightly outside ρ_{inv} (**Fig. 2c**). Note from the Kadomtsev sawtooth-crash reconnection model that $\rho_{q=1}=\rho_{inv}$ for peaked parabolic profiles of T_e and q, and $\rho_{q=1}>\rho_{inv}$ for a flat q profile inside q=1 [3].

Despite the obvious importance of the inversion radius, an additional effect is seen when heating above or below the midplane: central temperature and pressure respond differently to top or bottom q=1 deposition. Relative to on-axis deposition, top q~1 heating produces large normal sawtooth relaxations and degrades central T_{eo}, whereas bottom q~1 heating produces reduced amplitude central relaxations of the humpback type and increases central T_{eo}. The good central performance of bottom q=1 deposition coincides with central relaxations of lower amplitude. This top-/bottom- asymmetry may have its origin in the small co-/counter- current drive component generated even with purely poloidal injection, due to the poloidal magnetic field component arising from the plasma current [4].

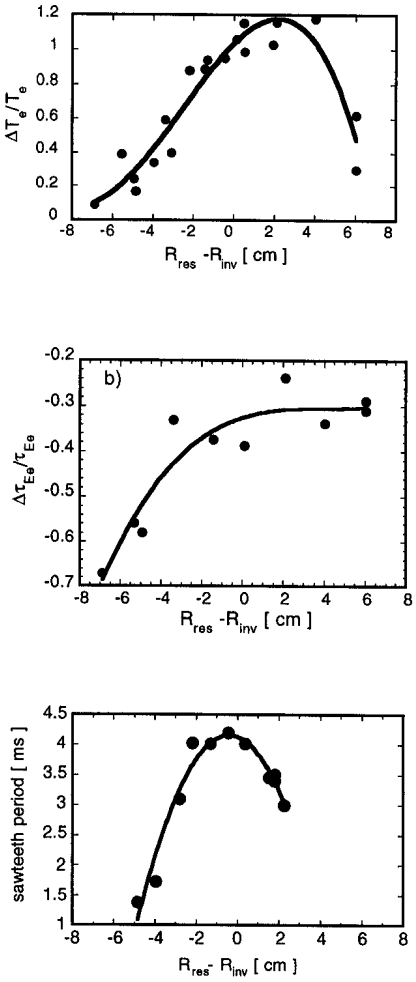

Fig. 2 Radial deposition scan through bottom HFS inversion surface, by varying B_φ (κ=1.32, q_a=5, n_{eo}=2 10^{19}[m^{-3}], P_{EC}=360kW):
a) Relative T_{eo} increase (2<q_a<6)
b) Relative global τ_{Ee} degradation
c) Sawtooth period.

Basic confinement dependencies (B, q_a, n_e, P) - A small plasma placed in front of the launcher with a quasi-horizontal launch was studied in order to minimise refraction effects at high density (θ=18°, z=38, κ=1.31, δ=0.15, θ=0° is horizontal). Scan domains were: 1.32<B_φ<1.45 T (deposition displacement of 20% of the plasma radius around q=1); 1.5×10^{19} m^{-3} < n_{eo} < overdense; 2.2<q_a<6; P_{EC}≤1 MW. In the q_a-scan, ratios of P_{tot}/P_{OH} from 3 to 14 were obtained during ECRH with 1MW power injection.

As a function of the *safety factor* q_a, the electron confinement time τ_{Ee} increases with q_a to a maximum at q_a~5 and drops for q_a>5 (**Fig. 3**). In the high q_a shots of this scan (P_{EC}=500 kW, 0.77<R_{res}<0.84 m), the power was deposited outside the inversion surface, which probably explains the drop at high q_a by analogy to the drop observed during the radial B-field scan at constant q_a, when heating outside q=1 (see **Fig. 2b**). **Figure 3** also contains

the corresponding ohmic-confinement-time q_a dependence, showing saturation at q_a>5. Even though confinement exhibits the neo-Alcator-like q_a scaling as in ohmic plasmas [5], confinement improvement with q_a is not as high during corresponding ECRH plasmas. It is likely that higher additional power will further degrade the favourable scaling with q_a. In the present heating experiments, however, this beneficial ohmic scaling feature still holds for ECRH power ratios $P_{ECRH} / P_{OH} > 9$.

The dependence of τ_{Ee} as a function of *density* on-axis is shown in **Fig. 4**. Low elongation plasmas (κ=1.16 and 1.32, $q_a \approx 5$), located in front of the launcher to minimise refraction effects at high density, were chosen for this scan. Stationary density just below cut-off density was not possible to obtain, due to the ECRH-induced density pump-out, explaining the absence of data just below cut-off (TORAY predicts full absorption for $n_{eo} \leq 4.0 \times 10^{19}$ m^{-3}). The confinement time scales linearly with density, as observed in previous low density EC experiments [6].

Power-induced confinement degradation was studied with 1MW of additional power, with a power deposition profile maximum at a radius of ρ=0.23. Heating results with P_{EC}>500kW contained a counter-ECCD component for one of the two launchers. This may however be of reduced significance on confinement, since power degradation in ECCD was observed to be similar to ECRH [7]. The power-induced degradation exponent α_P, ($\tau_{Ee} \sim P^{\alpha_P}$), measured for q_a=5 at n_{eo}=2 and 3×10^{19}m^{-3} (see **Fig. 5**), and at q_a=2.5 for a density close to 2×10^{19} m^{-3}, is as usual: $\alpha_P \sim -0.5$, or possibly somewhat lower. Note that this confinement degradation may have been favourably influenced by the effect of slightly off-axis heating on profiles and MHD-activity. In particular, the sawtooth period is lengthened for a deposition close to q=1, and when raising the power, sawtooth activity is observed to convert to humpback relaxations before disappearing at the higher powers.

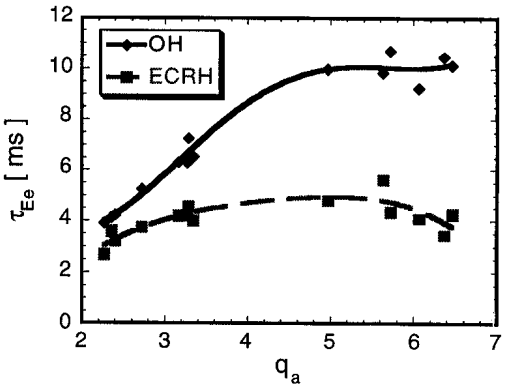

Fig. 3 τ_{Ee} versus q_a, for different deposition radii in a B_φ scan in ECRH, and OH plasmas.

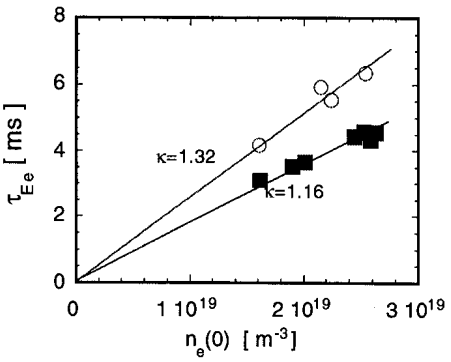

Fig. 4 τ_{Ee} as a function of n_{eo} for two elongations (κ=1.16, 1.32; δ=0.07, 0.16, q_a=4.7, 5.2)

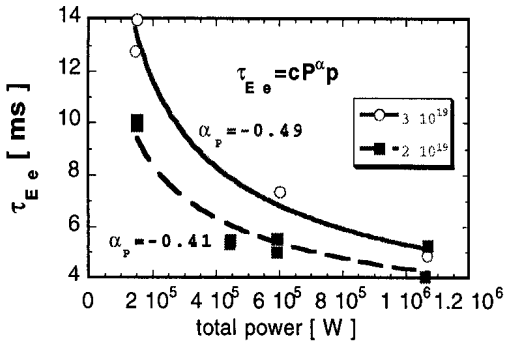

Fig. 5 τ_{Ee} power degradation for two densities, q_a=5.

period is lengthened for a deposition close to q=1, and when raising the power, sawtooth activity is observed to convert to humpback relaxations before disappearing at the higher powers.

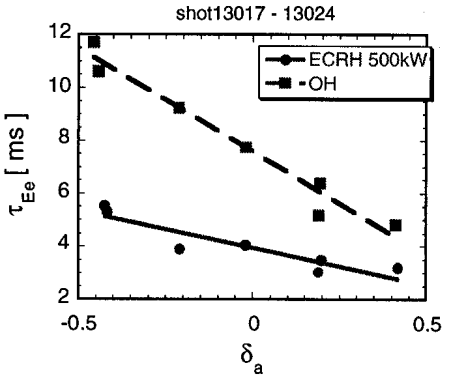

Fig. 6
τ_{Ee} as a function of δ, ohmic and ECRH data. (P_{EC}=500 kW, κ=1.32, q_a=3.5 (227<I_p<255 kA), n_{eo}=2 10^{19} [m^{-3}]).

Plasma shape: triangularity - The study of confinement with triangularity was done with medium q_a, q_a=3.5, at 500kW. The power was also deposited close to the inversion surface. Both ECRH and ohmic cases are shown in **Fig. 6**. As with ohmic heating, confinement improves with increasing negative triangularity during ECRH. Note that from this scan, the improvement of confinement with ECRH appears less than with purely ohmic heating. The real trend however is probably more favourable with negative triangularity than shown here, since power deposition occurred inside ρ_{inv} for δ>0 and outside ρ_{inv} for δ<0 (recall **Fig. 2b**).

Conclusions - Confinement, central heating and MHD-activity depend strongly on the location of the EC power deposition. Sawteeth periods are the longest for power deposition just outside ρ_{inv} and mode activity is enhanced for deposition inside ρ_{inv}. Dramatic increases in central electron temperature T_{eo} occur when power is deposited close to ρ_{inv} on the HFS or below midplane; small amplitude central relaxations of humpback type also occur here.

Within the range of plasma shapes and plasma currents investigated, the electron confinement time, τ_{Ee}, increases with safety factor, density and negative triangularity similar to the Ohmic heating case. There is little dependence of τ_{Ee} on the heating location provided power deposition occurs inside the q=1 surface; as power deposition moves out of the inversion surface, τ_{Ee} decreases. The power-induced energy confinement degradation exponent (τ_{Ee}~P^{α_P}) is as usual: α_p~ -0.5. As a general trend, central relaxations decrease in amplitude with increasing q_a, P_{EC}, or negative δ, in a situation where the confinement time increases.

This work was partially supported by the Fonds National Suisse pour la Recherche Scientifique.

References

[1] A. Pochelon et al., 2nd Eur. Top. Conf. on RF Heating and Current Drive of Fusion Devices, Brussels, **22A**, 253 (1998).
[2] T.P. Goodman et al., Proc. EC-10 Conf., Ameland, 305 (1997).
[3] Z.A. Pietrzyk et al., this Conference.
[4] T.P. Goodman et al., this Conference.
[5] J.-M. Moret et al., PRL **79**, 2057 (1997), H. Weisen et al., NF **37**, 1741 (1997).
[6] V.V. Alikaev et al., 10th Int. Conf. on Plasma Phys. Cont. Nucl. Fus., **I**, 419 (1985).
[7] Y. Esipchuk, Plasma Phys. and Contr. Fus. **37**, Suppl. 11A, A267 (1995).

Observations of Up-down Differences in Plasma Response during ECRH on TCV

T.P.Goodman, **M.A.Henderson**, Z.A.Pietrzyk, A.Pochelon, M.Q.Tran, J-Ph.Hogge, J-M.Moret, H. Reimerdes, O.Sauter, W.van Toledo,

Centre de Recherches en Physiquedes Plasmas, Ecole Polytechnique Fédérale de Lausanne

Association EURATOM-Confédération Suisse, CH-1015 Lausanne, Switzerland

Introduction: During initial experiments with electron cyclotron resonant heating (ECRH) on the TCV tokamak the plasma was swept vertically through a stationary microwave beam and the beam was swept vertically through a stationary plasma. Results from these vertical sweeps revealed an asymmetry in the plasma response when beam deposition was above or below the plasma midplane. The up-down asymmetry is observed on the sawtooth shape, soft x-ray intensity, central electron temperature and pressure, and ion tail temperature. The likely source of the asymmetry is the poloidal component of the magnetic field being either parallel or anti-parallel to the launched beam direction. For the current TCV geometry this introduces a co-counter electron cyclotron current drive (ECCD) component when the beam is above-below the plasma midplane, respectively. ECCD efficiencies (η) from the ray tracing code TORAY, during these sweeps are comparable to those calculated for ECCD experiments performed earlier[1] with low x-mode coupling. Likewise, both experiments exhibited similar plasma response with respect to the sawtooth shape, soft x-ray intensity, central electron temperature and pressure, and ion tail temperature. Future experiments are proposed to further explore the asymmetry and isolate its source.

Experimental setup: The TCV ECW system[2] when complete, will provide 3MW X2 (six 82.6GHz gyrotrons) and 1.5MW X3 (three 118Ghz gyrotrons) for 2s. These experiments used 0.5MW up to 1s pulse lengths. Each gyrotron is equipped with a matching optics unit including a two mirror universal-polarizer, an evacuated transmission line (30m) which includes a multihole power monitor, and an antenna comprised of a four mirror system which allows the launching of the beam in both the poloidal and/or toroidal directions. The so-called poloidal motion allows the beam deposition to be swept vertically through a circular plasma or two-thirds of the way through an elongated (κ=3) plasma several times during a shot. The toroidal rotation permits current drive experiments in either co or counter directions from shot to shot. The TCV vacuum vessel can accommodate various plasma shapes and elongations. These

experiments were performed on low density ($2*10^{-19}$ m^{-3}), low elongation ($\kappa \approx 1.3$), moderate q_a (≈ 4) plasmas; centered between the equitorial and upper lateral ports. The antenna used is located on an upper lateral port. Another antenna will be available on an equitorial port.

Experimental results: Scans of the deposition location through the plasma were performed to determine the optimum heating location. In particular three sweeps were performed: 1) "swept plasma" - sweep of the plasma position keeping the beam launching angle fixed, 2) "swept beam" - sweep of the beam launching angle keeping the plasma location fixed, and 3) "B_ϕ sweep" - sweep of radial deposition by varying B_ϕ while keeping q_a constant. Each sweep was performed in both directions with no noticeable hysteresis. The x-ray intensity, sawtooth shape and period, electron central temperature and pressure, and energy confinement time are all strongly dependent upon the heating deposition location relative to the inversion radius[3]. All of these parameters were optimal when heating was localized near or within the inversion radius. However, during the vertical sweeps an asymmetry in several of the above parameters was observed. The soft x-ray signal and sawtooth shape shown in Figure 1 exemplifies the up-down asymmetry. Humpbacks occur when heating on the bottom of the plasma; normal to partially saturated sawteeth when heating on the top. A corresponding asymmetry was observed with the central electron pressure (product of soft x-ray T_{e0} and FIR interferometer n_{e0}; see Figure 2), which was at a maximum when the deposition was below the plasma midplane. An asymmetry on T_{e0} was confirmed with Thomson scattering when several similar swept plasma shots were plotted together (Thomson, @20Hz, can not follow the rapid evolution of a single swept plasma). Since the ECRH power is dominate (500kW vs. 250kW ohmic) we can say that this may imply a significant asymmetry in confinement[3].

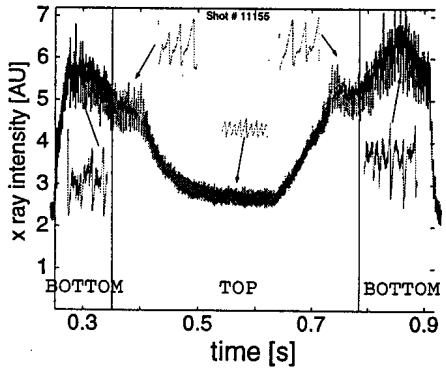

Figure 1 Up-down asymmetry in sawtooth shape and x-ray intensity while plasma is swept vertically. Humpbacks (normal sawteeth) are observed when beam deposition is below (above) the plasma mid-plane.

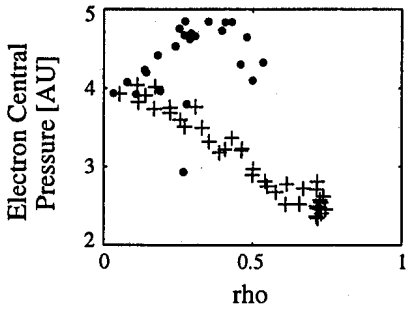

Figure 2 An up-down asymmetry is evident in the central electron pressure during a swept plasma shot. Pressure is significantly higher when heating below(•) than above(+) the plasma midplane.

In trying to understand the up-down asymmetry different potential sources are identified; sys-

tem geometry, ion drift direction and ECCD due to B_θ, among them. The asymmetry of sawtooth shape during ECRH is similar to the behavior observed during co/counter ECCD experiments in which a significant difference on the sawtooth shape between co and counter ECCD was observed. Despite a low theoretical (TORAY) efficiency $|\eta|<15*10^{-3}$ A/W (~15% of optimal coupling), normal and partially saturated sawteeth were seen during co ECCD and humpbacks during counter ECCD. This difference is similar to the up-down asymmetry during the swept plasma: normal sawteeth with deposition on top correspond to co ECCD and humpbacks on the bottom correspond to counter ECCD (as expected due to B_θ). Furthermore, TORAY ray tracing code models a small co/counter ECCD component with similar $\eta(13.1/-6.55*10^{-3}$ A/W) when the deposition location was on the top/bottom half of the plasma (see Figure 3).

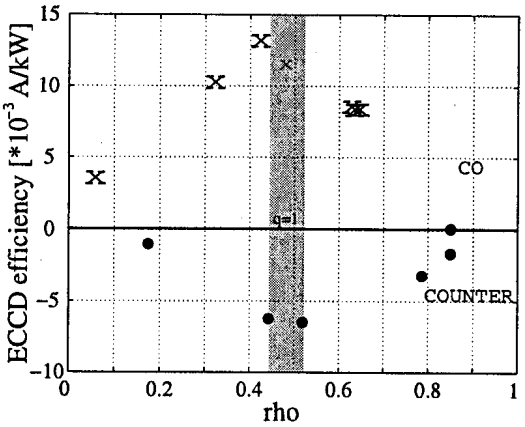

Figure 3 Co/counter ECCD efficiencies computed from TORAY during a swept plasma shot, with ECRH beam deposition above(X)/below(•) the plasma midplane.

To further suggest that co-counter ECCD as the source of the up-down asymmetry, the behavior on the central electron and ion tail temperatures during the sweeps are comparable with the low η ECCD discharges. T_{e0} increased with the x-mode coupling fraction and rose above ohmic during counter ECCD, while T_{e0} remained constant with x-mode coupling fraction during co ECCD. The same behavior is seen when heating below (counter) and above (co) the midplane during the plasma sweep: highest T_{e0} occurred when deposition was located below the midplane (see Figure 4). The ion temperature, which is Maxwellian during ohmic plasmas, develops a hot tail during both co and counter ECCD. The tail temperature is larger for counter

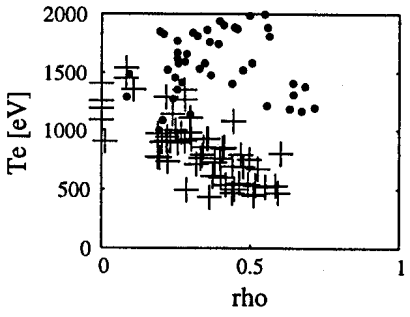

Figure 4 The asymmetry is seen on the T_{e0} when heating below(•) versus above(+) the midplane. The high T_{e0} signal when deposition is on the bottom corresponds with the increase in T_{e0} during counter ECCD above ECRH levels.

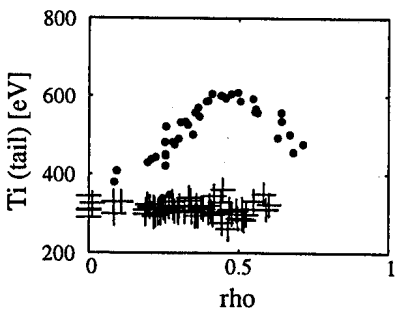

Figure 5 The ion tail temperature is higher when heating below(•) the plasma midplane than above(+). This corresponds with the ECCD experiment when counter ECCD produced larger ion tail temperatures than co ECCD.

ECCD than for co, which is also seen when heating below or above the midplane respectively (see Figure 5).

Future experiments: During the next campaign on TCV experiments are planned to fully characterize the up-down asymmetry and determine its source. For example: a shot to shot scan of the vertical deposition with an improved time resolution (x3) on Thomson scattering and with particular attention to possible confinement asymmetry; reversing B_ϕ; utilizing the equitorial launcher to separate out system asymmetries; etc.

Conclusion: An up-down asymmetry in central electron temperature and pressure, sawtooth shape and ion tail temperature has been observed when scanning the beam deposition along a vertical cord of the plasma. The plasma response in the bottom/top ECRH experiments follow the behavior for counter/co ECCD experiments. Only a small co-counter current drive was needed during the ECCD experiments to change from normal sawteeth to humpbacks. It follows that the sawtooth shape asymmetry may be due to the poloidal component of the magnetic field which introduces a counter/co ECCD component when heating on the bottom/top. TORAY ray tracing calculated η = -6.55 / +13.1 $*10^{-3}$ A/W when heating on the bottom /top (these values for η are comparable to the low η discharges of the ECCD experiments). The highest central electron temperatures occur when heating off axis on the bottom side of the plasma (counter ECCD). Large differences in co/counter ECCD temperatures occurred only with full sawtooth stabilization due to high η. In contrast to the present results which show high T_{e0} difference even at low η. This may be due to the high first pass absorption in the present experiments compared with the low η ECCD experiments. Further experiments are planned to fully characterize the asymmetry and isolate its source during the next TCV campaign.

This work was partially supported by Swiss National Science Funds

References

1. T.P. Goodman et al., 2nd EPS Conf. on Radio Freq. Heat. and CD of Fus. Div. Brussels **22A** p.245 (1998)
2. T.P. Goodman et al., 19th Symposium on Fusion Technology Lisbon p.565(1997)
3. Z.A. Pietrzyk et al., 2nd EPS Conf. on Radio Freq. Heat. and CD of Fus. Div. Brussels **22A** p.249 (1998)
4. A. Pochelon et al., 2nd EPS Conf. on Radio Freq. Heat. and CD of Fus. Div. Brussels **22A** p.253 (1998)

Effects of ECRH and ECCD on the MHD Relaxation Phenomena in TCV

Z.A.Pietrzyk, R.Behn, T.P.Goodman, M.A.Henderson, J-Ph.Hogge, A.Pochelon, F. Porcelli*, H.Reimerdes, M.Q.Tran, I. Furno, J-M.Moret, J.Rommers, O.Sauter, H. Weisen

Centre de Recherches en Physique des Plasmas, Ecole Polytechnique Fédérale de Lausanne
Association EURATOM-Confédération Suisse, CH-1015 Lausanne, Switzerland
**INFM and Politecnico di Torino, 10129 Torino, Italy*

This paper describes studies of MHD relaxation oscillations in the TCV tokamak (R=0.89m, a=0.25m, I_p<1.2MA, B_ϕ=1,44T) during ECRH (> 1MW power) and ECCD[1]. Observation of the temporal evolution of the soft-X emissivity revealed various characteristic features apart from the standard "sawtooth" shaped relaxation oscillations. In many cases the appearance of particular shapes, like inverted sawteeth, humpbacks, and hills could be attributed to changes in the power deposition with respect to the inversion surface (or q=1 surface). These studies have taken advantage of the flexibility of TCV to move the plasma in vertical direction during a shot. The power deposition has also been varied by sweeping the launching angle of the ECW beam (using steerable mirrors) and by varying the toroidal field strength. Different types of relaxation oscillations as seen on the soft-X emissivity signals[2,3] are shown in Fig. 1.

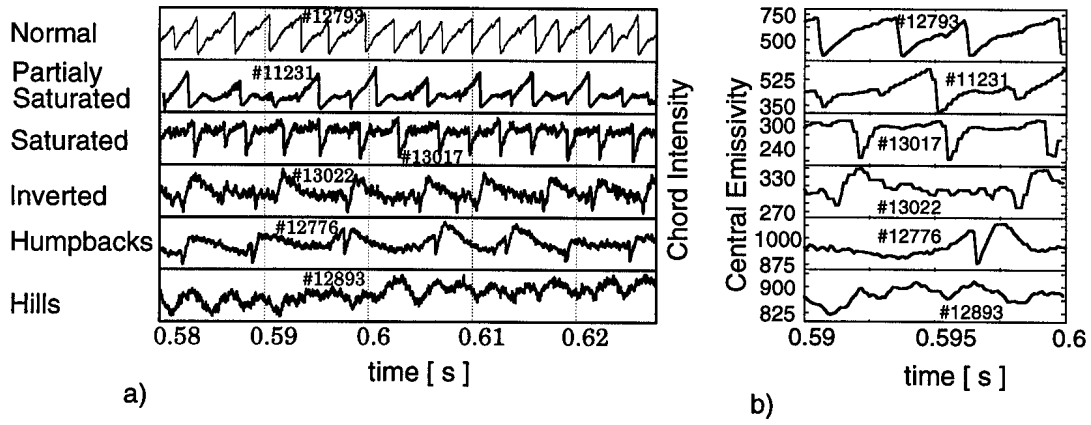

Figure 1. Different relaxation shapes observed during ECRH a) as seen by line integrated measurements, b) central (magnetic axis) emissivity from tomographic reconstruction show similar time dependencies.

In the case of ordinary sawteeth the variation of soft-X emissivity is usually interpreted as a variation in electron temperature. Our measurements indicate that this is no longer true for some of the other types of relaxation oscillations (such as humpbacks). Since the plasma emissivity in the soft-X range of wavelength is influenced not only by the electron temperature, but also, by the electron density and the effective ion charge, periodic variations of these parameters could, in principle, also influence the appearance of the relaxation oscillations. However, there are no other indications for rapid changes in electron density or Z_{eff}. Still, from a comparison between soft-X emissivity and temperature from Thomson scattering we find that in the case of the humpbacks the soft-X signal rises after a crash to a higher value than it would from the electron

temperature alone. The evolution of central T_e (from Thomson scattering) and X-ray emissivity (at the same time steps) are shown in Fig.2. In this figure the data taken from several humpbacks are represented on a normalized time scale (period fraction). Crashes occur at the normalized times "0" and "1".

Trying to generalize the temperature evolution during the cycle of a relaxation oscillation in the presence of ECRH, we find : $T_e(0)$ rises during the interval t1 after a crash, then saturates (interval t2), and finally rises again before the next crash (t3). Different shapes of sawteeth are just different combination of these times and the amount of non-thermal radiation: Normal "triangular" sawteeth do not have a saturation phase (t2=0); Saturated sawteeth have little or no temperature rise before a crash (t3≈0); Inverted sawteeth and humpbacks have a lot of non thermal radiation after crash; and hills are gentle fluctuations of a hot plasma (no instability, but SVD shows the inversion surface on large hills), representing the plasma behavior during fully stabilized sawtooth phase.

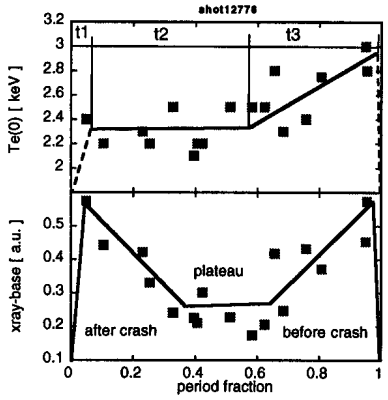

Figure 2. Central electron temperature as a function of the period fraction collected for many humpbacks of one shot, and central X-ray emissivity taken at the same time as temperature. Lines represent schematic behavior of both values.

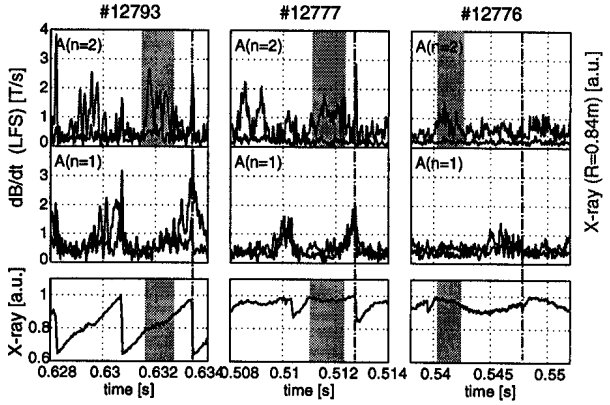

Figure 3 Toroidal mode activity during some of the sawtooth shapes. Vertical line indicate times of the crash in one of the sawtooth at each shot and gray lines indicates the strong n=2 mode activity. Modes activities seen by magnetic and X-rays are shown.

The saturation of temperature is caused by n=2 mode activity, present at the time of saturation, see figure 2. The mode (n=2) which creates saturation later decays and the temperature starts to rise again until the sawteeth crash. The mode n=1 is visible as a precursor to the crash and is growing during the second temperature increase. There is an apparent separation of modes, n=2 for temperature saturation and n=1 as a precursor to a crash.

The shape and the sawtooth period are not correlated. The sawtooth period is longest when heating near the inversion surface, and is the same in all positions on this surface. The sawtooth shape for the same shot, however, may be different when heating on different part of this surface, see figure 3.

As expected, the sawtooth period is function of the current density profile, while the sawtooth shape is influenced by the n=2 mode which causes the temperature to saturate, and the amount

of non-thermal radiation. This non thermal radiation seems to be correlated to a small amount of current drive which changes with the heating position on the flux surface. That is the current drive changes from the co to counter direction when heating below or above the midplane. The humpbacks and inverted sawteeth have been observed only with some amount of counter current drive on TCV.

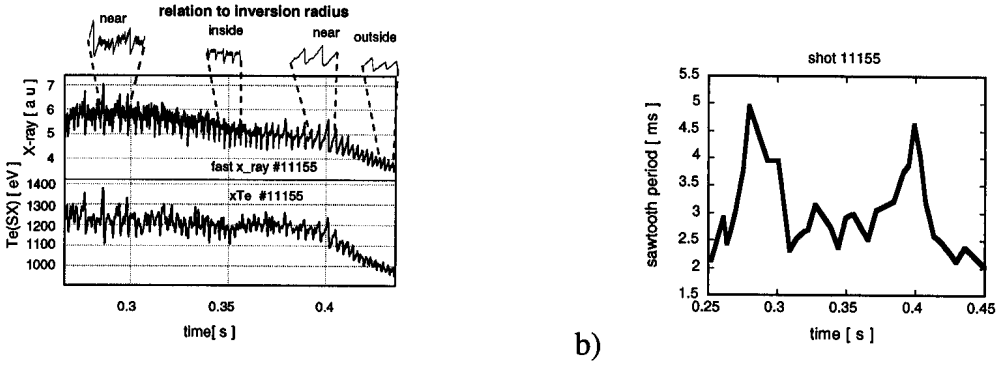

Figure 3 a) time dependence of X-ray radiation and soft X-ray temperature, beam crosses the inversion surface and 0.28 s "down" and 0.4 s "up". b) sawtooth period for the same shots.

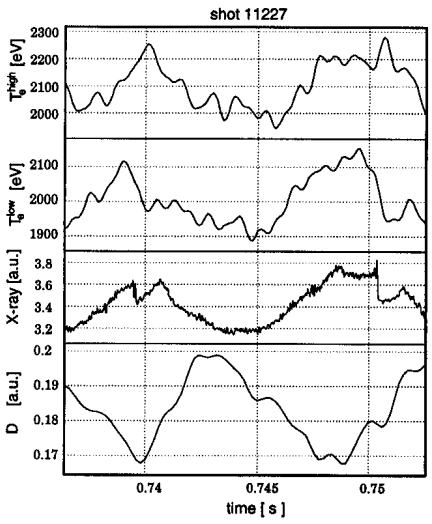

Figure 4. Time dependence of X-ray temperature, difference between "high" and low temperature and x-ray intensity for a shot with humpback sawteeth.

There are four wavelength channels of X-ray intensity for X-ray temperature measurements. As the X-ray temperature can be determined by only two spectral points, two "temperatures" may be calculated from measured signals and these two "temperatures" could be the same for a Maxwellian electron plasma. In figure 4 two of these "temperatures" are plotted as a function of time for a shot with humpbacks relaxation. The "low" temperature refers to a combination of filters with lower pass cutoff energy than the "high" temperature combination. In this figure the D_α signal is also plotted. One can see that just after the crash the difference in temperatures rises rapidly (the maximum value of the "high" temperature is after the crash in humpback) indicating an excess of the high energy photons at that time. This could indicate the presence of high energy electrons which produce radiation in excess of the Bremsstrahlung radiation of a single temperature of Maxwellian plasma. The "low" temperature corresponds closely to "Thomson" temperature, which is measured from the bulk electron distribution function. The high energy tail may exist before the crash, but is not effected by the crash and this is why the difference is larger after the crash; or, the crash may generates fast electrons which are enhanced by ECRH in certain heating conditions (small amount counter current drive).

The size (average radius) of the inversion surface during heating (ECRH) and co or counter current drive (ECCD) in the plasma center. The typical changes are visible in figure 5. With ECRH the inversion surface expands when heating inside and has the largest radius when heating at inversion surface. It shrinks when the heating moves outside and it may even disappear, (q(0) is pushed above one).

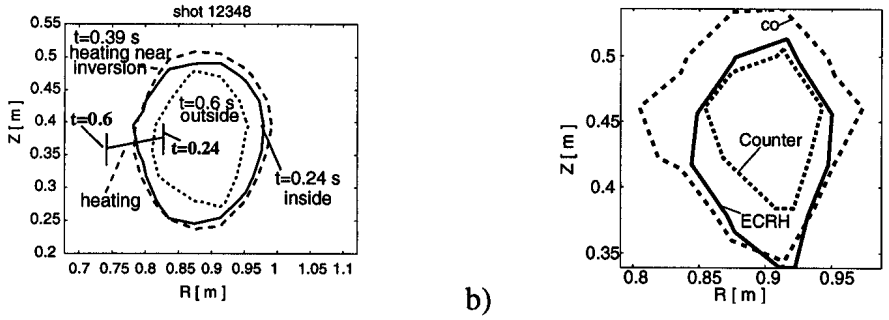

Figure 5. Inversion surfaces for a) shot with sweeping radial position of heating and b) for shots with ECRH Co and Counter CD.

Similarly for co ECCD the surface expands since a larger fraction of the total current is inside this surface and the surface shrinks with counter ECCD. The sawtooth shapes with co CD are either normal or saturate, while for the same target plasma counter CD produces full sawtooth stabilization (Hills) with the optimum wave elipticity, or humpbacks when most of the power is in the O-mode [4].

As mentioned befire during ECRH the maximum sawtooth period is obtained with the heating position at the inversion surface. With enough power the sawteeth may disappear completely, giving full sawteeth stabilization by modification of the shear near the q=1 surface. On the other hand we can drive q(0) above one by heating outside of the inversion surface and also obtain full sawteeth stabilization. Thus, two approaches to sawteeth stabilization are possible; by increasing sawtooth period to infinity, or by reducing it to zero.

In some situations humpbacks appear at two different normalized radii, when moving the power deposition location during a shot. The first one with power deposition near the inversion surface and the second series of humpbacks appears near the q=2 surface as calculated from magnetics. This second series may not be related to the q=2 surface but rather to the q=1 surface, since for a flat q-profile the inversion surface and q=1 surface are largely separated and the q=1 surface calculated by the magnetics may be too small.

This work was partially supported by Swiss National Science Funds.

References

1. T.P. Goodman et al. Proc. EC-10 conference, Ameland (1997)

2. A.Pochelon et al. 24th EPS Conf. on Contr. Fusion and Plasma Phys. **21A** partII 537 (1997)

3. Z.A.Pietrzyk et al., 2nd EPS Conf. on Radio Freq. Heat. and CD of Fus. Dev Brassels.**22A** p.249 (1998)

4. T.P.Goodman et al 2nd EPS Conf. on Radio Freq. Heat. and CD of Fus. Dev Brassels.**22A** p.245 (1998)

5. Z.A.Pietrzyk, A.Pochelon, T.P.Goodman, M.Henderson, et al. Nuclear Fusion (submitted).

Observation and interpretation of "profile consistency" features in the TCV tokamak

H. Weisen, R. Behn, I. Furno, J.-M. Moret, O. Sauter and the TCV team

Centre de Recherches en Physique des Plasmas
Association EURATOM - Confédération Suisse
École Polytechnique Fédérale de Lausanne
CH-1015 Lausanne, Switzerland

A large variety of plasma conditions has been created in TCV (Tokamak à Configuration Variable, B_T<1.5T, R_0=0.88m, a<0.25m). They include limited and diverted discharges with elongations in the range 1 to 2.58, triangularities between -0.7 and 1 as well as 'square' shapes with plasma currents in the range 0.1-1MA. Over the entire range of quasi-stationary ohmic conditions investigated we observe a correlation between electron pressure profiles and conductivity profiles, suggesting that $\langle p\rangle/p(0) \approx \langle j\rangle/j(0)$, where $\langle\ \rangle$ refers to an average over the volume or respectively the cross sectional area of the plasma. The profiles become broader as the average current density is increased. These "profile consistency" features are in apparent agreement with theoretical considerations based on minimum energy states of the plasma [1,2] or on stationary entropy [3]. We show that these observations can also be accounted for by the effects of sawtooth activity.

Experimental observations and theoretical models supporting the idea that electron temperature and/or the pressure and/or current density in tokamaks preferentially assume certain privileged profile shapes have been reported for more than two decades [1-5]. Arunasalam et al [5] have proposed a practical working definition of this principle motivated by tearing mode stability considerations. It postulates the existence of unique, natural profile shapes for j(r) and because of ohmic relaxation, for the shape of $T_e(r)$ or $T_e^{3/2}(r)$. The consequences of the postulate, as given in [5], are 1) that the normalized sawtooth inversion radius, $\rho_{inv}= r_{inv}/a$ and 2) the broadness of the temperature profile $\langle T_e\rangle/T_e(0)$ are device independent and are functions of $1/q_a$ only. The same authors propose a third consequence expressed as $T_{e0}^{3/2} \propto I_p R_0/(c_\sigma a^2 V_{loop} F(1/q_a))$, which merely combines the postulation of universal current profiles characterized by $\langle j\rangle/j_0 = F(1/q_a)$ and the assumption of Spitzer conductivity, $\sigma_{Spit} = c_\sigma T_e^{3/2}$. The widths of "natural" current and pressure profiles from minimum energy models [1,2] are given by $j/j(0)=p/p(0)=(1+(q_a/q_0-1)\rho^2)^{-2}$ with profile widths equal to $1/q_a$ if q_0=1 is assumed for the safety factor on axis. Stationary entropy models [3] also lead to the observable prediction j/j(0)=p/p(0). Such a relation is indeed observed in ohmic L-modes in TCV. The observation is expressed as $\langle p_e\rangle/p_e(0) \approx \langle T_e^{3/2}\rangle/T_e^{3/2}(0)$, where the brackets indicate a volume (or practically equivalently cross sectional area) average and is shown in fig. 1 for a wide range of plasma shapes including elongations up to 2.54, triangularities in the range -0.5 to +0.7, 'square' and 'rhomboidal' shapes and diverted ohmic L-mode plasmas. The

electron temperature and density measurements were obtained using a multichord Thomson scattering system with 10-25 measurement locations in the plasma depending on plasma size. The confinement properties of this set of some 300 discharges have been reported in ref. [6].

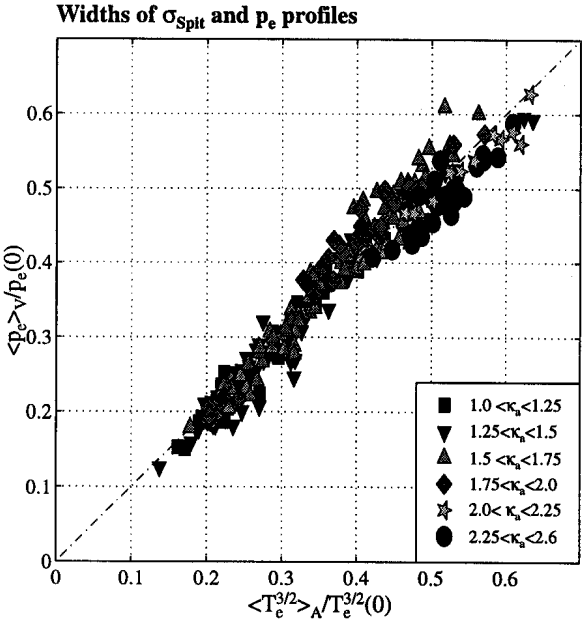

Fig.1 Width of electron pressure profile versus width of Spitzer conductivity profile.

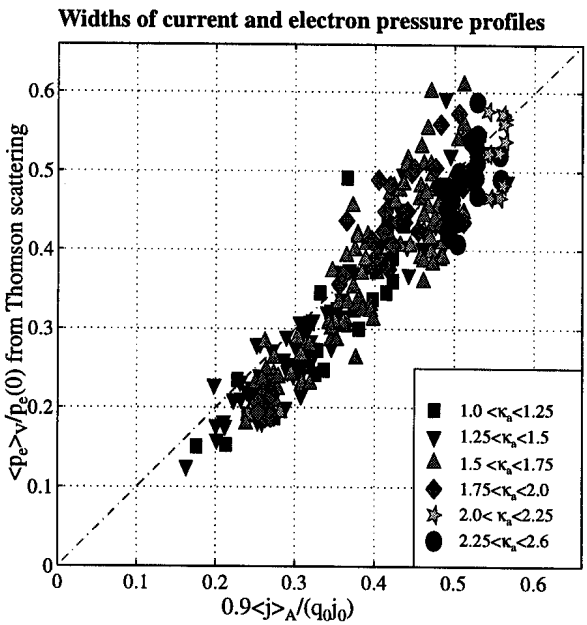

Fig. 2 Width of electron pressure profile versus width of current profile (assuming q_0=0.9).

The widths of the pressure and Spitzer conductivity profiles increase approximately as the inverse safety factor at 95% of the poloidal flux, $1/q_{95}$. A better scaling, shown in figure 2, is expressed by a relation directly with the width (up to a factor q_0) of the current profile,

$$\frac{\langle p_e\rangle}{p_e(0)} \propto \frac{\langle j\rangle}{q_0 j_0} = \frac{\langle j\rangle^* \cdot B_{0vac}}{(\kappa_0 + 1/\kappa_0)\cdot B_0} \quad (1) \text{ where } j_0 = \frac{(\kappa_0 + 1/\kappa_0)B_0}{\mu_0 R_0 q_0} \text{ and } \langle j\rangle^* = \frac{\mu_0 R_0 \langle j\rangle}{B_{0vac}}$$

is the dimensionless average current density, j_0 being the current density on axis, B_0 the toroidal field on axis, B_{0vac} the corresponding vacuum field, R_0 the major radius of the magnetic axis and κ_0 the central elongation.

TCV is equipped with a 200-channel X-ray tomography system which was used to measure the sawtooth inversion radius in these discharges [7]. For shaped plasmas we define the effective inversion radius as $\rho_{inv} = \sqrt{A_{inv}/A_p}$ where A_p is the plasma cross sectional area and A_{inv} is the area enclosed within the flux surface at which sawteeth invert. Remarkably (fig. 3), ρ_{inv} scales as already shown for $<p_e>/p_0(0)$. We could declare that the mechanisms implied in the various theories are responsible for shaping these profiles and that the only generalisation required is to replace $1/q_a$ by $<j>/(q_0 j_0)$ as a scaling parameter in shaped plasmas. Such a view is unsatisfactory because neoclassical conductivity, not Spitzer conductivity, should apply. Moreover, because of sawtoothing, the tokamak core, although quasi-stationary on average, is never in resistive equilibrium.

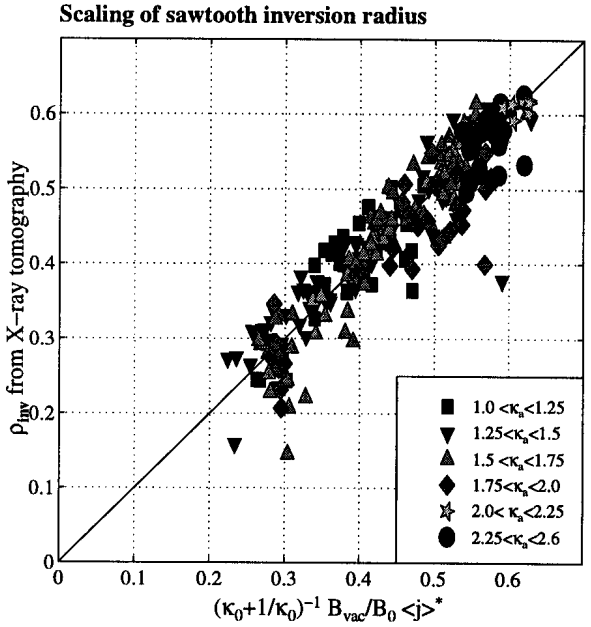

Fig. 3 Inversion radius from X-ray tomography versus width of current profile in shaped plasmas.

Another concern is the applicability of the above theories to plasmas dominated by gross MHD phenomena. As we'll show the effects of sawtoothing can lead directly to profile relationships which are not distinguishable from the above mentionned predictions. We propose a temptative model current profile given outside the sawtoothing zone as $j=E\sigma_{neo}+j_{boot}$ where $E = V_{loop}/(2\pi R_0)$ is the externally induced electric field, σ_{neo} is the neoclassical conductivity and j_{boot} is the bootstrap current, which in these ohmic plasmas only contributes a few percent to the total current. Inside the q=1 surface a prescribed safety factor profile of the form $q(\rho) = q_0 + (1-q_0)(\rho^2/\rho_1^2)$ is assumed, where ρ_1 is the normalized radius of the q=1 surface. For $\rho \le \rho_1$ the corresponding current profile is

$$j_{in}(\rho) = j_0 \cdot \frac{q_0}{q(\rho)} \cdot \frac{B(\rho)}{B_0} \cdot \frac{(\kappa(\rho)+1/\kappa(\rho))}{\kappa_0+1/\kappa_0} \cdot \left\{1 - \frac{\rho^2\cdot(1-q_0)}{\rho_1^2\cdot q(\rho)}\right\}. \quad (2)$$

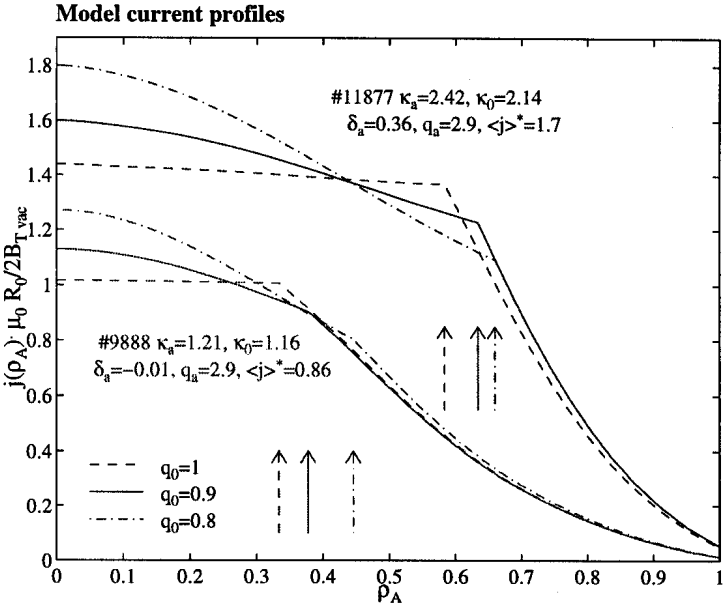

Fig.4 Examples of model current profiles for two different TCV discharges with q_a=2.7 and three choices of q_0.

For any choice of the free parameter q_0, we determine ρ_1 from the condition $\int j dA = I_p$. Examples of the resulting profiles are shown in fig.4 for κ_a=1.2 and 2.4. The figure also illustrates the beneficial effects of elongation on the current carrying capacity of the discharge. The inversion radius from the model is consistent with the first consequence [5] of "profile consistency". The best overall match of ρ_1 and ρ_{inv} is obtained for q_0=0.9. The scaling of ρ_1 (fig.5) is seen to be identical to that of ρ_{inv} (fig. 3).

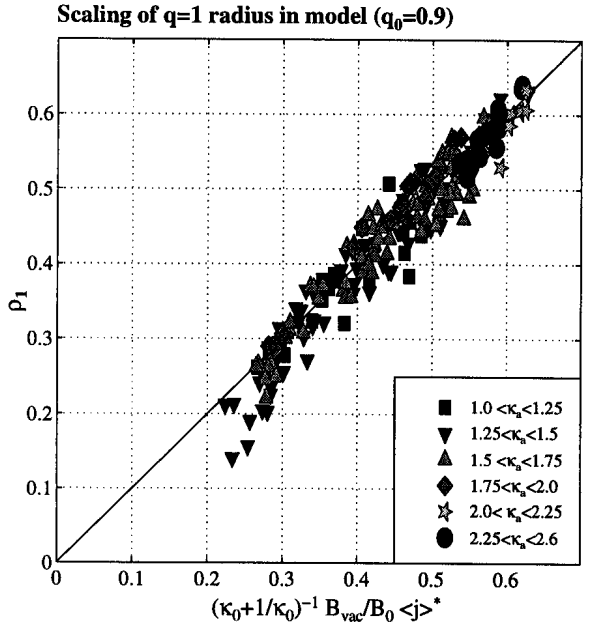

Fig. 5 Scaling of q=1 radius from model with width of current profile.

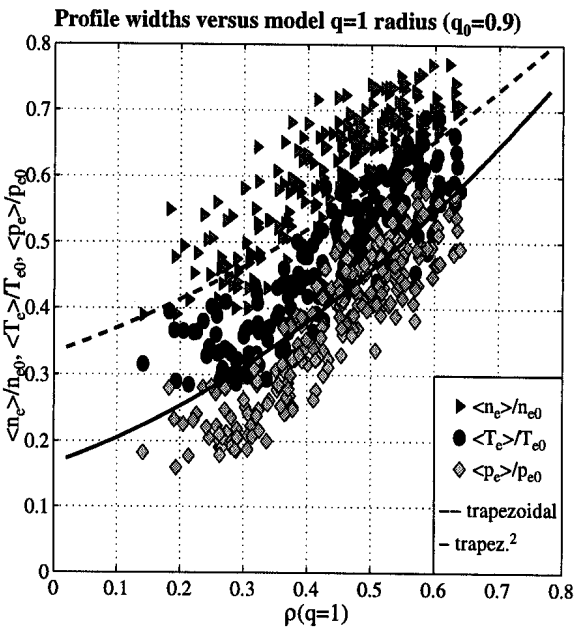

Fig. 6 Widths of electron density, temperature and pressure profiles versus q=1 radius.

We propose that the scaling of the widths of the other plasma profiles also result from the flattening effect of sawtoothing and are related to the q=1 surface. Fig. 6 shows the widths of n_e, T_e and p_e as function of ρ_1. These widths are close to those expected if the profiles were merely trapezoidal (broken line) or trapezoidal squared (continuous line) with a flat portion up to ρ_1. It appears that profile widths, expressed as $<x>/x_0$ are not very sensitive to details of the profiles and hence to transport in the confinement zone ($\rho>\rho_1$). We conclude that profile relations such as $<j>/j_0 \approx <p>/p_0$ are a consequence of sawtoothing and result from the limitation of the central current density and from the flattening of the core profiles of temperature and density. Despite the apparent agreement, the observations reported here should therefore not be considered as supportive of the above-mentioned theories.

Ackn.: This work was partly supported by the Swiss National Funds for Scientific Research.

References:

[1] Biskamp D., *Comments Plasma Phys. Control. Fusion* **10** (1986) 165

[2] Kadomtsev B., Proc. *Int. Conference on Plasma Physics,* Kiev, 6-12.4 (1987) 1273

[3] Minardi E., *Physics Letters A* **240** (1998) 70

[4] Coppi B., *Comments Plasma Phys. Controlled Fusion* **5** (1980) 261

[5] Arunasalam V. et al, *Nuclear Fusion* **30** (1990) 2111 and references therein

[6] Weisen H., Alberti S., Barry S. et al, *Plasma Physics Contr. Fusion* **39** (1997) B135

[7] Anton M., Weisen H., M.J. Dutch, *Plasma Phys. Control. Fusion* **38** (1996) 1849

Observation of β-Limits in Highly Elongated Tokamak Plasmas

F. Hofmann, O. Sauter, R. Behn, H. Reimerdes

Centre de Recherches en Physique des Plasmas,
Association EURATOM - Confédération Suisse,
Ecole Polytechnique Fédérale de Lausanne, CH-1015 Lausanne, Switzerland

1. Introduction

According to the Troyon scaling law [1], the β-limit is proportional to the plasma current and inversely proportional to the horizontal minor radius and the toroidal magnetic field, $\beta(\%)=C_T I_p(MA)/[a(m)B_t(T)]$, where C_T, the Troyon factor, is typically between 2.5 and 4.0, depending on the pressure and current profiles. Ideal MHD theory predicts that the Troyon factor is significantly reduced at high elongation or near the plasma current limit [2,3,4]. Experimentally, the degradation of the Troyon factor at high elongation has not been clearly demonstrated up to now, mainly because very few tokamaks are equipped with feedback systems allowing operation beyond $\kappa=2$. The TCV tokamak can operate routinely up to $\kappa=2.5$, and in this paper, we summarize recent experiments showing evidence for β-limits at high elongation.

2. Creation of Highly Elongated Plasmas in TCV

It is well known that the growth rate of the fundamental axisymmetric mode in elongated tokamak plasmas increases rapidly with elongation. In order to stabilize this mode, an active feedback system is required whose response time is of the same order as the inverse open loop growth rate of the unstable mode. TCV has a unique vertical position control system, using slow active coils outside the vacuum vessel and a fast active coil inside the vessel [5]. The response times of the power supplies driving the slow and fast coils are approximately 1.0 and 0.1ms, respectively. Between 1993 and 1996, TCV was operated with slow coils only. Consequently, the maximum axisymmetric growth rate that could be stabilized was of the order of 1000 s^{-1} and the plasma elongation was limited to about $\kappa<2.1$. In 1997, the fast coil became operational and, after a phase of testing and optimization, the new system allowed us to stabilize plasmas with open loop growth rates up to 4400 s^{-1} and elongations up to 2.58 [5].

3. Limits of Operation

Experiments at high elongation have shown that there are basically four conditions that must be satisfied to avoid disruptions. The first of these conditions is the well-known ideal MHD kink limit, $q_a>2$, where q_a is the safety factor at the plasma boundary. From an experimental point of view, this condition is not quite sufficient for stability, especially when one is working with highly elongated, D-shaped plasmas. In such plasmas, the safety factor rises very steeply as one approaches the plasma boundary. Thus, for $q_a=2$, we find q-values

considerably less than 2 at flux surfaces which are very close to the plasma boundary. Experience has shown that, in this case, stable operation requires that $q_{95}>2$ rather that $q_a>2$. The second obvious condition for stability is that the open loop growth rate of the vertical instability, γ, must be less than the maximum growth rate that the feedback system can handle. In TCV, this can be expressed as $\gamma<\gamma_{max}\approx4000\ s^{-1}$. However, γ is not a parameter which can be directly controlled by the operator. In low β, Ohmic plasmas, γ depends mainly on elongation, triangularity and internal inductance [6]. The internal inductance at a given elongation is in turn a function of the plasma current. The result is that at each elongation and triangularity, the plasma current must exceed a critical value such that $\gamma<\gamma_{max}$. A third condition for stable operation which has recently emerged form experiments in TCV [7], can be expressed as $I_N<3MA/(mT)$, where I_N is the normalized current, $I_N=I_p/(aB_t)$. This condition replaces the first one, $q_{95}>2$, whenever $\kappa>2.3$. The fourth operational limit finally is the β-limit. Normally, in Ohmic plasmas, ideal MHD β-limits cannot be reached because this would require operation at densities exceeding the Greenwald limit by a large factor. In highly elongated plasmas, however, β-limits can be reached under Ohmic conditions at densites which are less than 30% of the Greenwald limit. Fig. 1 shows experimentally achieved values of q_{95} vs. κ, in TCV.

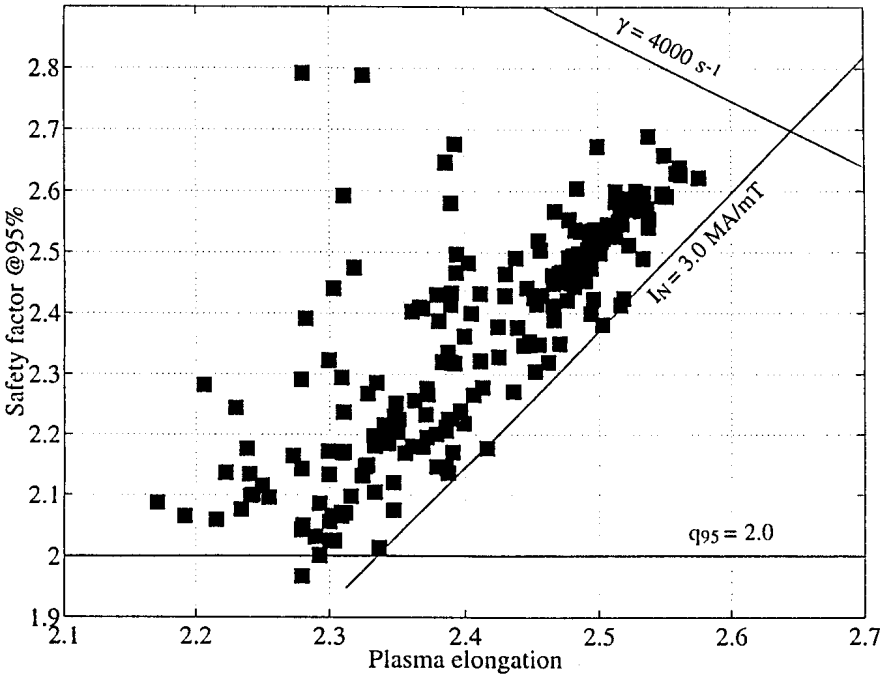

Fig. 1. Operational limits for D-shaped, Ohmic plasmas in TCV

4. β-limits at High Elongation in TCV

β-limits depend on a large number of parameters (plasma shape, q-profile, pressure profile). In Ohmic plasmas, the profiles vary somewhat with machine condition and cannot be controlled. Nevertheless, the existence of a β-limit can be clearly seen by comparing two consecutive, identical discharges, differing only in their volume averaged pressure. Fig. 2 shows three examples of such discharges. It is seen that the evolution of the plasma current and elongation of the two discharges in each pair are nearly identical, whereas the β values are slightly different. In each case, the discharge with higher β disrupted, whereas the one with lower β did not. These disruptions are usually preceeded by MHD mode activity, leading to a m/n=2/1 locked mode [8].

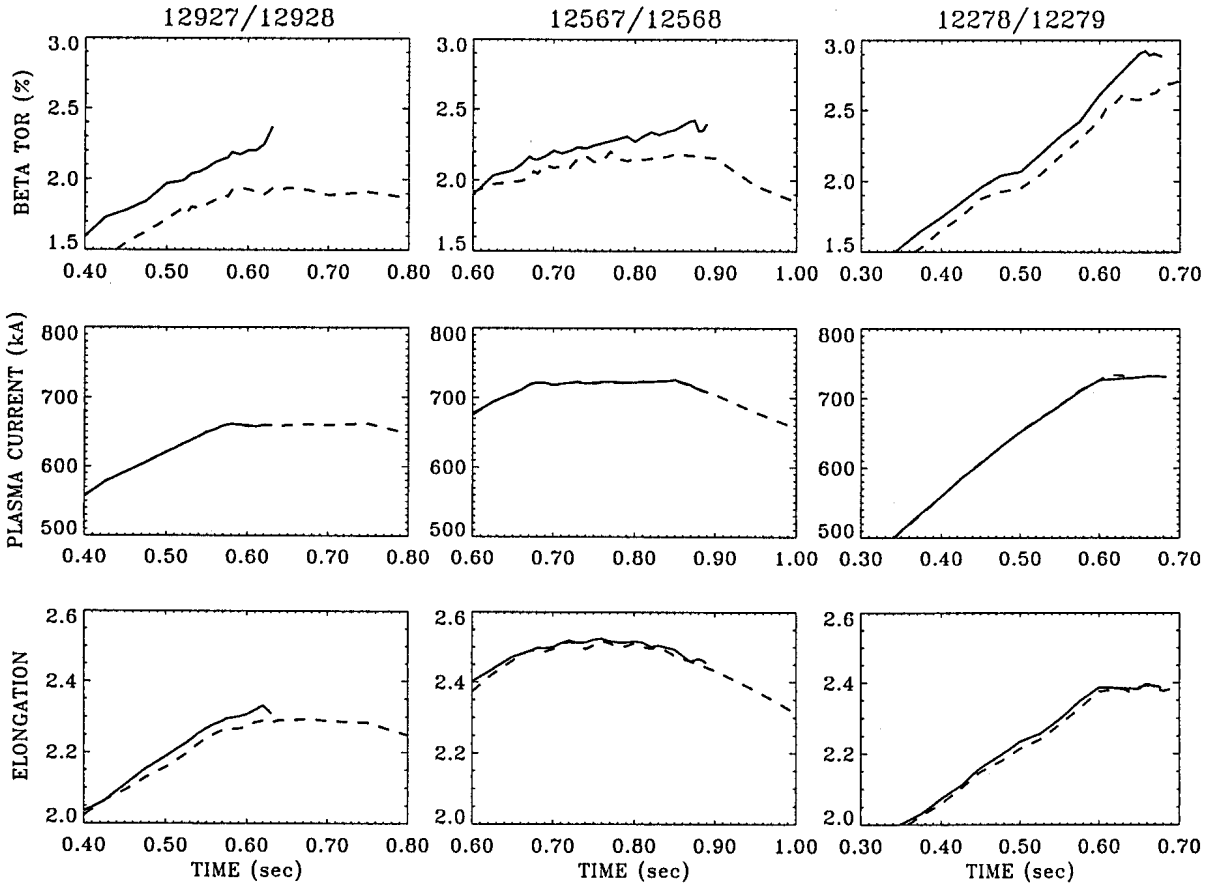

Fig. 2. Evolution of toroidal β, plasma current and elongation in three pairs of discharges. Disruptive and non-disruptive discharges are identified by solid and dashed lines, respectively.

5. Comparison with Ideal MHD Theory

MHD stability limits at high elongation have recently been calculated, using plasma shapes, pressure and current profiles of actual TCV discharges [4]. TCV experimental equilibria are reconstructed with the LIUQE code [9], then recomputed in flux coordinates with the CHEASE code [10]. Ideal MHD stability limits are computed with ERATO [11] and KINX [12]. The ideal MHD β limit, as determined by the n=1 external kink mode, is shown in Fig. 3 for two elongations, κ=2.2 and κ=2.5. The calculations were performed, using the experimental plasma boundary as well as experimental pressure and current profiles. The stability limit is given as a band with finite width to show the effect of small variations in the pressure and current profiles within experimental uncertainties. β-limits due to ballooning modes and n=2, n=3 ideal kink modes are much higher than the n=1 kink limit and are therefore irrelevant here. The experimental points shown in Fig. 3 were obtained for D-shaped plasmas with elongations between 2.20 and 2.58. We note that the theoretical stability limits are entirely consistent with the experiments in TCV. In particular, it is seen that the discharge 12414, as well as all discharges with I_N>3MA/(mT) which terminated in a disruption, are very close to the ideal limit, whereas the non-disruptive discharge 12413 is slightly further away from the limit.

6. Conclusions

Highly elongated, D-shaped plasmas have been produced in TCV. Typical shape parameters were $\kappa=2.5$, $\delta=0.35$, $\lambda=0.27$, where δ and λ are the triangularity and squareness, as defined in [3]. Since TCV has a rectangular vacuum vessel, positive squareness is necessary at high elongation in order to reduce the growth rate of the vertical instability. β-limits were found to be between 2 and 3%, in agreement with ideal MHD stability calculations, based on measured plasma shapes and profiles.

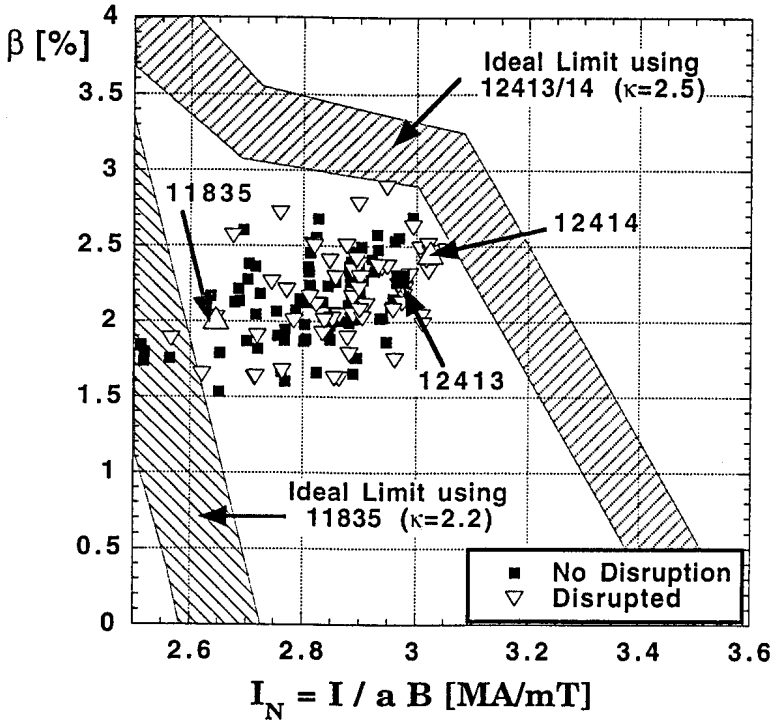

Fig. 3. Ideal MHD β limits vs. normalized current. Experimental points are shown as open triangles and solid squares for disruptive and non-disruptive discharges, respectively.

Acknowledgements

This work was partly supported by the Fonds National Suisse de la Recherche Scientifique.

References

[1] F. Troyon et al., Plasma Phys. Controlled Fusion **26** (1984) 209.

[2] A.D. Turnbull et al., Nucl. Fusion **28** (1988) 1379.

[3] G. Eriksson et al., in Europhysics Conference Abstracts, 1992 International Conf. on Plasma Physics, Innsbruck 1992 (EPS, Geneva, 1992), Vol 16C, p. I-343.

[4] O. Sauter et al., in Fusion Theory, 7th European Fusion Theory Conference, Jülich, 1997 (Forschungszentrun Jülich, 1998) Reihe Energietechnik, Vol. 1, p. 255.

[5] F. Hofmann et al., Nucl. Fusion **38** (1998) 399.

[6] D.J. Ward et al., Nucl. Fusion **34** (1994) 401.

[7] F. Hofmann et al., in Controlled Fusion and Plasma Physics (Proc. 24th Eur. Conf. Berchtesgaden, 1997) Vol 21A, Part II, EPS, (1997) 525.

[8] H. Reimerdes et al., this Conference.

[9] F. Hofmann et al., Nucl. Fusion **28** (1988) 1871.

[10] H. Lutjens et al., Comput. Phys. Commun. **97** (1996) 219.

[11] R. Gruber et al., Comput. Phys. Commun. **21** (1981) 323.

[12] L. Degtyarev et al., Comput. Phys. Commun. **103** (1997) 10.

MHD Precursor to Disruptions in Highly Elongated Plasmas

H. Reimerdes, L. Villard, F. Hofmann, O. Sauter, A. Pochelon

Centre de Recherches en Physique des Plasmas,
Association EURATOM - Confédération Suisse,
Ecole Polytechnique Fédérale de Lausanne, CH-1015 Lausanne, Switzerland

Introduction

Elongation of the plasma cross-section has become a tool to increase confinement and β-limits of tokamak plasmas. The operation at high elongation requires the stabilization

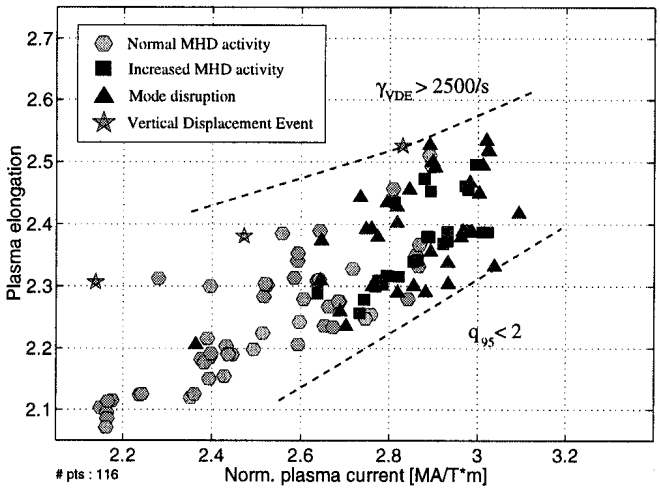

Figure 1: MHD activity in highly elongated ohmic TCV plasmas depend on elongation κ and normalized plasma current $I_N = I_p/(aB_0)$. The dependence of the growth rate of the axisymmetric mode γ_{VDE} [1] and of the safety factor on the surface including 95% of the flux on κ and I_N are indicated by one contour line each.

of the axisymmetric mode, which may lead to the loss of vertical position control, the so-called vertical displacement event (VDE). A minimum current is required for stable operation (Fig. 1) [1]. The upper current limit is imposed by the edge safety factor q_a, which has to be kept significantly higher than 2 to avoid the ideal MHD kink instability. For an elongation $2 < \kappa < 2.3$ this limit is well described by $q_{95} \geq 2$ (Fig. 1). Increasing the elongation usually allows for a higher current. However, in TCV this is only valid up to $\kappa \approx 2.3$. Disruptions, which are preceded by MHD activity, limit the operation to normalized currents $I_N = I_p/(aB_0) \leq 3\,MA/mT$ (Fig. 1). Ideal MHD stability calculations have predicted that the current limit in highly elongated plasmas ($\kappa > 2.2$) is significantly reduced by a finite β [2]. Recent calculations using TCV equilibria show that the global plasma parameters are close to the ideal limit [3]. In order to identify the disruption precursor its structure is compared with computed ideal modes. Owing to its good resolution in space and time and its high signal level during the disruption, magnetic rather than x-ray emissivity measurements, are used to characterize the experiment.

Analysis of MHD activity by magnetic measurements

TCV is equipped with pick-up coils arranged in a complete poloidal array and two complete toroidal arrays on the equatorial low (LFS) and high (HFS) field sides. The probes

were installed inside the vacuum vessel and measure the magnetic fluctuations parallel to the vessel wall $\dot{\tilde{b}}_{||}$. A biorthogonal decomposition (BD) [4] of the toroidal and poloidal measurement matrix $X(r_i, t_j)$ into spatial eigenmodes (topos) $v_k(r_i)$ and temporal eigenmodes (chronos) $u_k(t_j)$

$$X(r_i, t_j) = \sum_k E_k \cdot v_k(r_i) \cdot u_k(t_j) \tag{1}$$

reveals the corresponding poloidal and toroidal mode structure, as well as its temporal evolution. In contrast to Fourier techniques the BD does not use predefined base functions. Therefore it is more appropriate for the analysis of events which have neither a harmonic time dependence nor a spatial structure with a pure Fourier component, such as the poloidal mode structure.

The BD of the magnetic measurements reveals that all disruptions at high elongation were preceded by a locked $m/n = 2/1$ mode. (Fig. 2). The characteristic growth time is

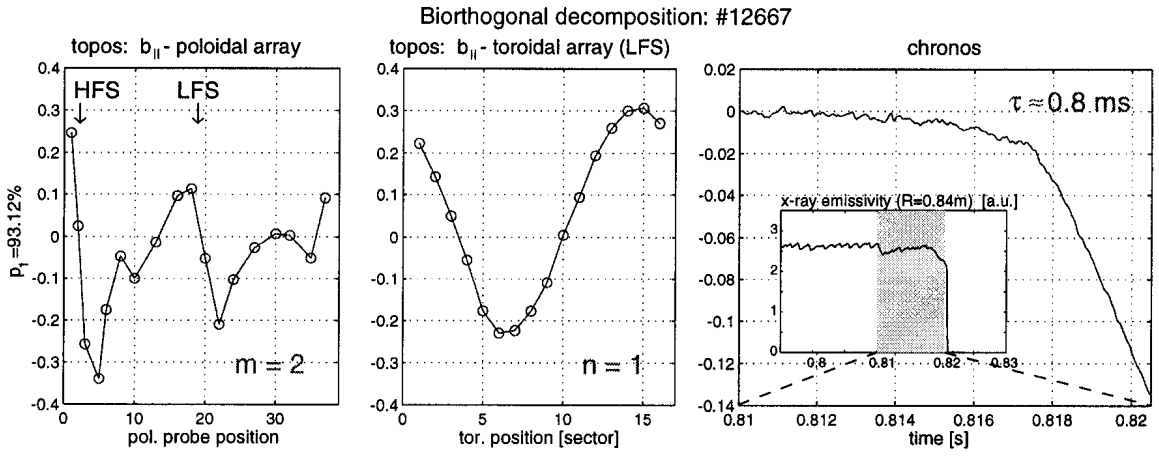

Figure 2: The dominant eigenvector of the biorthogonal decomposition of the magnetic measurements, containing 93% of the signal power, shows a m/n=2/1 disruption precursor mode, that grows locked.

derived from the corresponding chronos and varies from 0.1 to 1.5 ms. Furthermore, for $I_N > 2.7$ rotating 4/3 and 3/2 modes were frequently observed. The rotation frequencies were typically $10 - 15$ kHz and $5 - 11$ kHz respectively and the modes grew with characteristic times ranging from 0.5 to 3 ms. They did not necessarily lead to disruptions but caused crashes in central x-ray emissivity and degraded the confinement.

Comparison of measured and calculated mode structure

The magnetic measurements are compared with the linear ideal MHD global eigenvalue code ERATO [5]. The equilibrium is reconstructed from the magnetic and Thomson scattering measurements using the code LIUQE [6], and then re-calculated in magnetic co-ordinates with CHEASE [7]. An ideal TCV wall is included in ERATO. The central safety factor q_0 is fixed to 1.25 to avoid the 1/1 ideal internal kink mode. To find an unstable ideal mode, the current in the calculations for the disruptive discharge #12667

has to be increased by 5%. If q_{min} is sufficiently close to 1, the unstable mode is a toroidal kink. The displacement vectors in the plasma and corresponding contour lines of the poloidal component of the magnetic perturbation in the vacuum are shown in Fig. 3, left. The toroidal phase angle Φ of the calculated magnetic perturbation at the location of the magnetic probes is fitted to the poloidal structure obtained by BD (Fig. 2). Fit and experiment show good agreement (Fig. 3, center). However, the magnetic perturbation

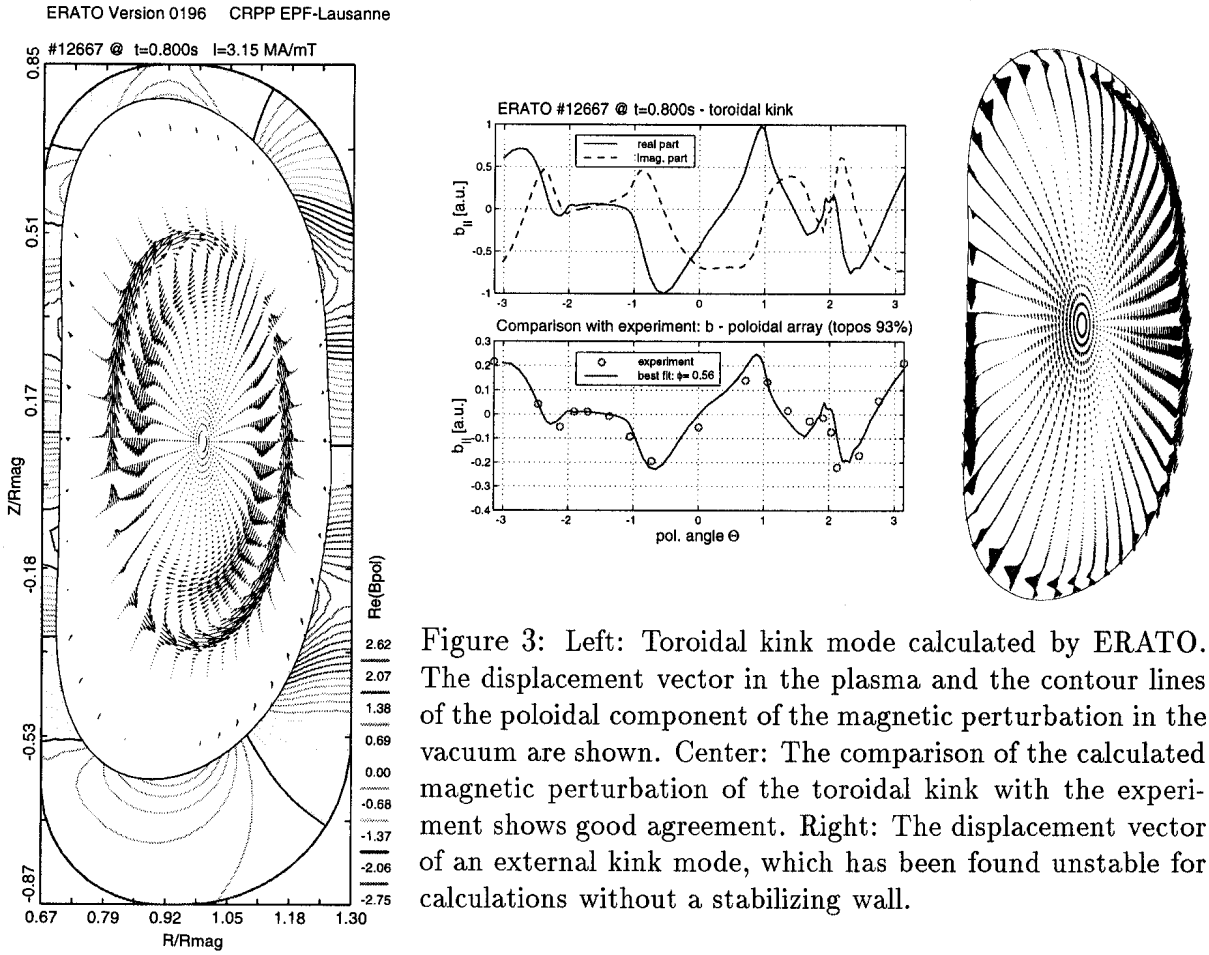

Figure 3: Left: Toroidal kink mode calculated by ERATO. The displacement vector in the plasma and the contour lines of the poloidal component of the magnetic perturbation in the vacuum are shown. Center: The comparison of the calculated magnetic perturbation of the toroidal kink with the experiment shows good agreement. Right: The displacement vector of an external kink mode, which has been found unstable for calculations without a stabilizing wall.

at the plasma edge has a strong $m = 2$ component, indicating that the comparison with magnetic measurements is not sensitive to the central activity. This is supported by the absence of a disruption related $m = 1$ component in the SXR-tomography. The external kink mode responsible for the ideal limit is found stable for an ideal wall at the TCV position. Its structure can be computed by removing the ideal wall (Fig. 3, right) which makes the direct comparison with magnetic measurements difficult. Therefore, calculations including the finite resistivity of the wall have to be made. An identification of the source of the instability also requires a comparison with resistive modes.

Resistive instabilities

Disruptions also occurred at an I_p and a β far below the ideal limit. These disruptions were always preceded by cascades of 3/2, 4/3, and occasionally 5/4 modes. An analysis of the

tearing parameter Δ' in a cylindrical approximation ($m \gg 1$) of typical q-profiles shows that within the uncertainties of q_0 and variation of the distance between the resonant flux surface and the plasma boundary the 3/2 mode is almost always unstable. Small profile variations can easily destabilize the 4/3 and occasionally even the 5/4 modes, whereas all other modes (for $m > 2$) have been found stable. This is consistent with the experimental observations. Furthermore, the island width growth rate, which is estimated in cylindrical approximation from magnetic measurements, is several *meter/second* and corresponds to an expected growth rate of tearing modes in the order of $\rho_s/\tau_{res} \approx 1\, m/s$. This suggests that in the high current discharges tearing modes are easily destabilized. These can then modify profiles to destabilize the 2/1 mode causing disruptions well below the ideal limit.

Summary and conclusion

The disruptions, that occur in highly elongated ohmic TCV plasmas and limit the current to $I_N \leq 3$, are preceded by a locked 2/1 mode. The structure of this mode at the plasma edge is obtained by a biorthogonal decomposition of the magnetic measurements. Ideal MHD calculations show that the disruptions occur very close to the current limit at finite β. The external kink, which is responsible for this limit, is stable for an ideal wall at the TCV position. This makes the direct comparison with magnetic measurements difficult. An identification of the precursor requires a comparison with calculations including the resistivity of the wall and the plasma, which is still pending. Further evidence for the testing of the ideal limit is given by the observation that disruptions occurring well below the ideal limit can be explained by preceding resistive modes, which modify the equilibrium and trigger the 2/1 mode.

Acknowledgments

The authors thank S. Medvedev for useful discussions. This work was partly funded by the Fonds National Suisse de la Recherche Scientifique.

References

[1] F. Hofmann, et al., Nucl. Fusion **38**, 399 (1998).
[2] A.D. Turnbull, et al., Nucl. Fusion **28**, 1379 (1988).
[3] F. Hofmann, O. Sauter, et al., this conference.
[4] T. Dudok de Wit, et al., Phys. Plasmas **1**, 3288 (1994).
[5] R. Gruber, et al., Comput. Phys. Commun. **21**, 323 (1981).
[6] F. Hofmann, G. Tonetti, Nucl. Fusion **28**, 1871 (1988).
[7] H. Lutjens, et al., Comput. Phys. Commun. **97**, 219 (1996).

Influence of the plasma shape on mode locking during the plasma ramp-up in TCV

Y. Martin, J.B. Lister and A. Pochelon

Centre de Recherches en Physique des Plasmas,
Association EURATOM - Confédération Suisse,
Ecole Polytechnique Fédérale de Lausanne, CH-1015 Lausanne, Switzerland

INTRODUCTION

Disruptions have to be avoided as much as possible in tokamaks, because of the huge mechanical constraints that disruptions impose on the machine design through magnetic forces. In a device like ITER, only a small number of disruptions will be allowed. It is therefore important to know where the dangerous operational regions are, in order to avoid them. Since all causes of disruptions are not yet clearly understood, a statistical approach can be useful. In this paper, we present the location of one type of disruptions, those induced by locking modes (LM), in the TCV operational diagram, as well as the technique established for TCV to prevent a repetition of shots already known as disruptive because of these modes.

LOCKING MODES IN TCV

TCV is a medium sized tokamak (R=0.88m, a=0.25m, Ip≤1MA, B_ϕ≤1.5T) devoted to the investigation of the influence of the plasma shape on plasma characteristics such as transport, confinement and stability. This tokamak has 18 independent poloidal field coils to shape the plasma up to a design elongation of 3 (achieved: 2.56) and with a triangularity between -1 and 1 (achieved -.5 and .8).

In the beginning of TCV operation, locking modes often appeared during the plasma current ramp-up. Some empirical knowledge was gained and the rate of locking mode induced disruptions dropped considerably. Plasma shaping and density programming were found to be the key parameters to avoid these disruptions.

The locking modes are characterised by an oscillation increasing in amplitude and slowing down in frequency, as shown in Fig. 1. The typical duration of the locking phase is 50 ms, with a frequency starting around 5kHz. These modes are either visible in the soft X-ray emission signal or in the magnetics measurements. Their structure is usually m=2 and n=1. Once the mode is locked, the plasma exhibits a succession of internal disruptions before a final complete crash. This disruptive phase can last from 10 ms to 50 ms. Because of their fatal issue, which is the case in more than 95 % of the onsets, the region of the operational domain to be avoided is the one crossed at the beginning of the locking mode. In order to determine this time of birth, we calculated the spectrogram of the soft X-ray emission signal, as shown in Fig. 1b. The time of the birth, t_{birth}, is determined by eye as the beginning of the frequency decrease as soon as its amplitude is significant.

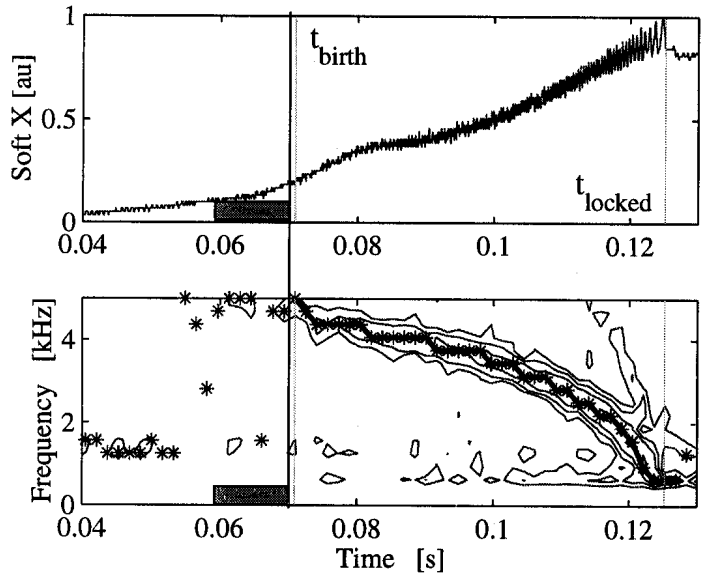

Figure 1: Soft X ray signal with its spectogram. The time used for the analysis is t_{birth}, the time when the mode starts to brake.

Over 8000 shots have been examined, locking modes occuring during the plasma ramp-up were identified and the time of birth was extracted. About 100 cases of locking modes were found and put in a database together with points in the current ramp-up for all shots reaching q_{edge} below 3.3. For these ~1500 shots, data have been sampled every 10 ms during the plasma formation, i.e. in limiter configuration and with only ohmic heating. All basic plasma parameters such as plasma current, density, shape and position were calculated at these times. Examining the database, we find that locking modes occured in a small range of: a) the plasma density and b) a shape parameter, defined as $\delta^2 + (\kappa-1)^2$, in agreement with our experience. This highly localised distribution is shown in Fig. 2.

Since locking modes originate in MHD phenomena, it is interesting to check whether they appear preferencially at given values of the safety factor. Some locking modes clearly start when the value of the safety factor at the edge crosses an integer value. These are usually observed in discharges located in the upper part of the vessel. In contrast, the locking modes growing in the lower part of the vessel seem to start at any value of q_{edge}, possibly indicating the presence of a stronger error field in the bottom of the tokamak.

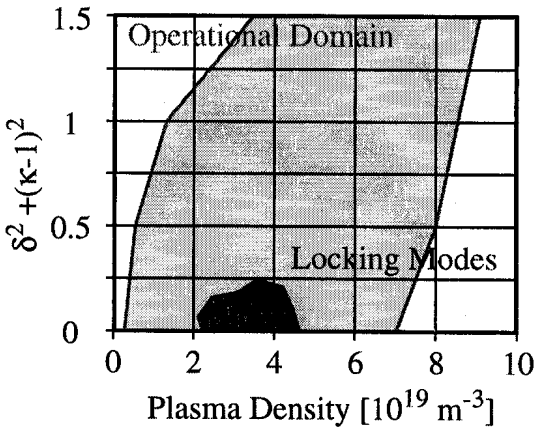

Figure 2: Locking modes locations in the plasma density and shaping domain.

The locking modes starting around q_{edge}=3 have been avoided by increasing the plasma shape parameter. Figure 3 shows the location of the locking modes as a function of the plasma shape and the rate of change of q_{edge}. It clearly shows that the locking modes which usually initiate at q_{edge}=3 appear in circular plasma cross-section with any rate of change in q and that stationary operation around q_{edge}=3 can be achieved with shaped plasmas.

DISTANCE TO LOCKING MODES

In order to decribe the dangerous regions where LM have their birth location, all the parameters presented above must be considered simultaneously. Since the representation of such regions in a multi-dimensional space is quite difficult, a simpler representation must be chosen: after a

normalisation of the parameter space (I_p, n_e, κ, δ and z_{mag}), the euclidian distance to the n closest LM, n being equal to 1 to 5, has been calculated for every point along the trajectory of a discharge. This distance decreases as long as one or more LM are approached. Fatal trajectories exhibit distances close to zero at the time of the LM birth, as shown in Fig. 4a. This LM started in conjunction with the crossing of an integer value of q_{edge}. Figure 4b presents a case where the distance diminished drastically around q_{edge}=4, but was not too close to disrupt and then, thanks to the shaping as shown in the inset, the distance to any LM increased to a large value even for q_{edge}=3.

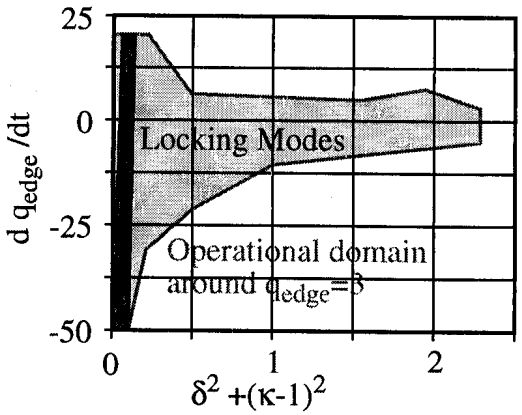

Figure 3: Operational domain covered by time slices having $2.9<q_{edge}<3.1$.

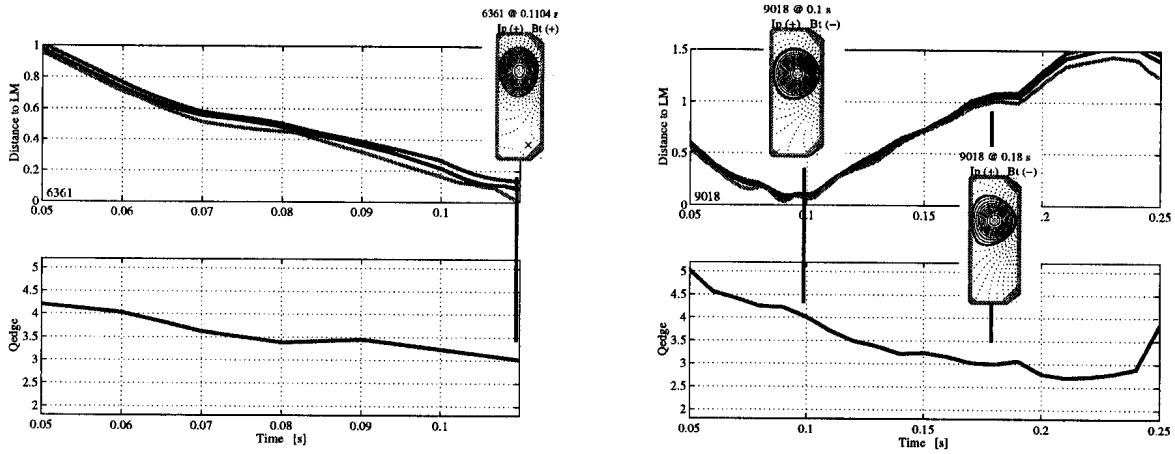

Figure 4: Time evolution of the distance to the n closest locking modes, n=1, 3 and 5, shown together with the evolution of q_{edge}. On the left, the discharge entered locking modes at 0.11 s. On the right, the shaping prevented the discharge to have these modes.

This distance to the n closest LM has been calculated for all time slices in the database. A critical distance has been defined as the distance above which the point is considered as safe. Smaller distances are considered as too dangerous and the plasma is supposed to be lost in a LM. A confusion matrix has been estimated for many values of this critical distance as well as for many values of the number n, representing the number of closest LM to account for. The best distance is found to be 0.1, with the confusion matrix expressed in table 1.

	No disruption	Disruption
No Alarm	1180	28
Alarm	65	174

Table 1: Confusion matrix

This table indicates that in 90% of the cases, the estimation of the distance is good enough to declare a trajectory as being dangerous somewhere. Although these calculations have been performed on existing data, the distance to locking modes can be calculated during the preparation of a new discharge, since all the parameters used in the distance estimation are

chosen, within the uncertainty of the control system, during this preparation. This step has been implemented on TCV and tests of the system are under way.

In order to improve the description of the regions where locking modes are born, a clustering technique has been applied to the database: when two locking modes are separated by a distance smaller than a given value, they are considered as belonging to the same cluster. One after the other the LM are attributed to clusters. Since the number of clusters is not known a priori, an algorithm scans the value of the distance. Starting at a very low value, the clusterisation finds as many clusters as starting points. With a larger distance LM start to aggregate and, finally, with a too large distance, there is only one cluster. The optimum is reached when most of the points are attributed to the maximum number of clusters. Figure 5 shows the clusters in a "multi2D" representation, in the lower part. In the upper part, the clusters are plotted as a function of the safety factor, showing that the clustering automatically grouped the LM appearing at the same q_{edge} value. This clustering technique provides a nice tool to represent the most dangerous regions. These clusters can also be used during the preparation of a discharge since they represent the dangerous regions.

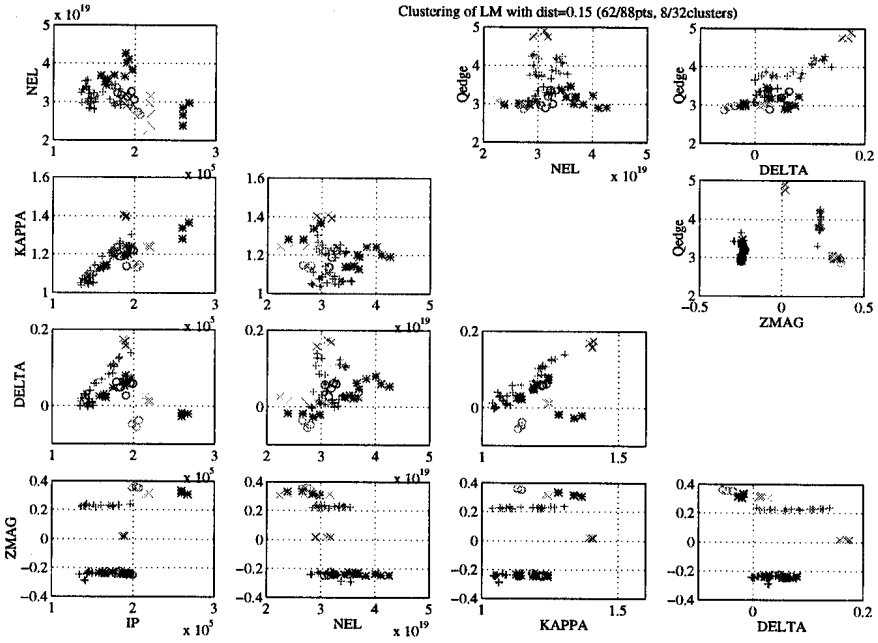

***Figure 5**: The clustering with a distance of 0.15.*

CONCLUSION

Locking modes have been observed during the plasma ramp-up in TCV. The empirical knowledge, stipulating that the plasma shape, density and safety factor are the parameters governing the birth of LM, have been verified statistically. The distance to the closest locking modes has been calculated on a large TCV dataset. This distance has been shown to adequately characterise the danger of LM creation and therefore can be used during the preparation of a discharge, in order to avoid the repetition of a locking mode induced disruption already experienced.

ACKNOWLEDGEMENTS

This work was partly funded by the Fonds National Suisse de la Recherche Scientifique.

Prediction of the ITER H-mode power threshold by means of various statistical techniques

The ITER H-mode Threshold Database Working Group
presented by Y. Martin*

* *Centre de Recherches en Physique des Plasmas, Association EURATOM - Confédération Suisse, Ecole Polytechnique Fédérale de Lausanne, CH-1015 Lausanne, Switzerland*

INTRODUCTION

The prediction of the additional heating power required to reach the H-mode regime is a key issue in the design of ITER. This prediction is usually based on power law scalings calculated from the data provided by different tokamaks. An enhancement of the international threshold database has allowed a refinement of the existing scalings [1-5]. However, even if more parameters (a, κ, δ and S_{plasma}) are taken into account, than in the former list of parameters (n_e, B_ϕ and R), and more tokamaks are represented in the database (now 10 tokamaks: ASDEX, AUG, ALCATOR C-MOD, COMPASS-D, DIII-D, JET, JFT-2M, JT-60U, PBX-M, TCV), some scattering in the data does still exist (RMSE≅25-30%), leading to a large uncertainty in the ITER power threshold prediction: P_{thr}(ITER)=90MW with a 95% confidence interval of [-40 +80]MW. With the final goal of reducing this uncertainty, completely different approaches have been investigated. This paper presents the first results obtained by 3 other statistical techniques: discriminant analysis, system identification and neural networks.

DISCRIMINANT ANALYSIS

Discriminant Analysis consists of finding a new set of co-ordinates, that are linear combinations of the input parameters and which minimises the correlation between data from different classes and maximises the correlation within a class. In the case of a "two classes" discrimination, one axis of the new set is enough to represent the classification: along this axis, the data from the two classes appear as histograms, more or less separated. The classification ability along this new axis is characterized by two quantities. One of these represents the distance between the average values of the two classes, divided by the average of the standard deviation of the two classes. The other is the rate of well classified data over the total amount of data, expressed in %. For every classification attempt, a subset (typically 80% of the data, randomly chosen) of the selected data is used for the calculation of the classifier. The remainder of the data is used as a test population. The quality of the classification is then characterised by its ability to succeed on this test population. Finally, some kind of stability of the classification is tested by repeating the calculations several times, the dataset each time being slightly different because of its random selection.

From the two histograms obtained along this new axis, a probability function is deduced [6]. By fitting a hyperbolic tangent to this function, using weights corresponding to the number of points in each bin, a smooth function is determined which is well defined all over the space. If the RMSE of the fit is too high the classification is rejected.

Knowing the co-ordinate transformation and the mapping between the new axis and the probability function, it is possible to determine the probability of being close to the LH transition

as a function of the Loss Power ($P_L = P_{heat}$ -dW/dt). This can be done for existing data, see figure 1.a-c; for new points in actual machines in order to predict the necessary additional power; or for future machines like ITER, see fig 1.d. When applied to existing data, the actual loss power and phase (L-mode, H-mode or "at the LH transition") is compared with the probability function to give an estimate of the success rate. A time slice is estimated to be in L-mode if the probability is below 0.5. When the model is applied to ITER design values, (R=8.1m, a=2.8m, B_t=5.5T, $\bar{n}_e=5*10^{19}m^{-3}$, κ=1.7, $S_{pl}=1100m^2$), the loss power which gives a probability of 0.5 is considered as the threshold power. In order to estimate the stability of the model, the probability function has been calculated for points around the design values (random 10% perturbations). The ITER predicted threshold power is then an average of 20 different power values corresponding to these random perturbations around the design values. The uncertainty in the threshold power is the standard deviation of the threshold powers.

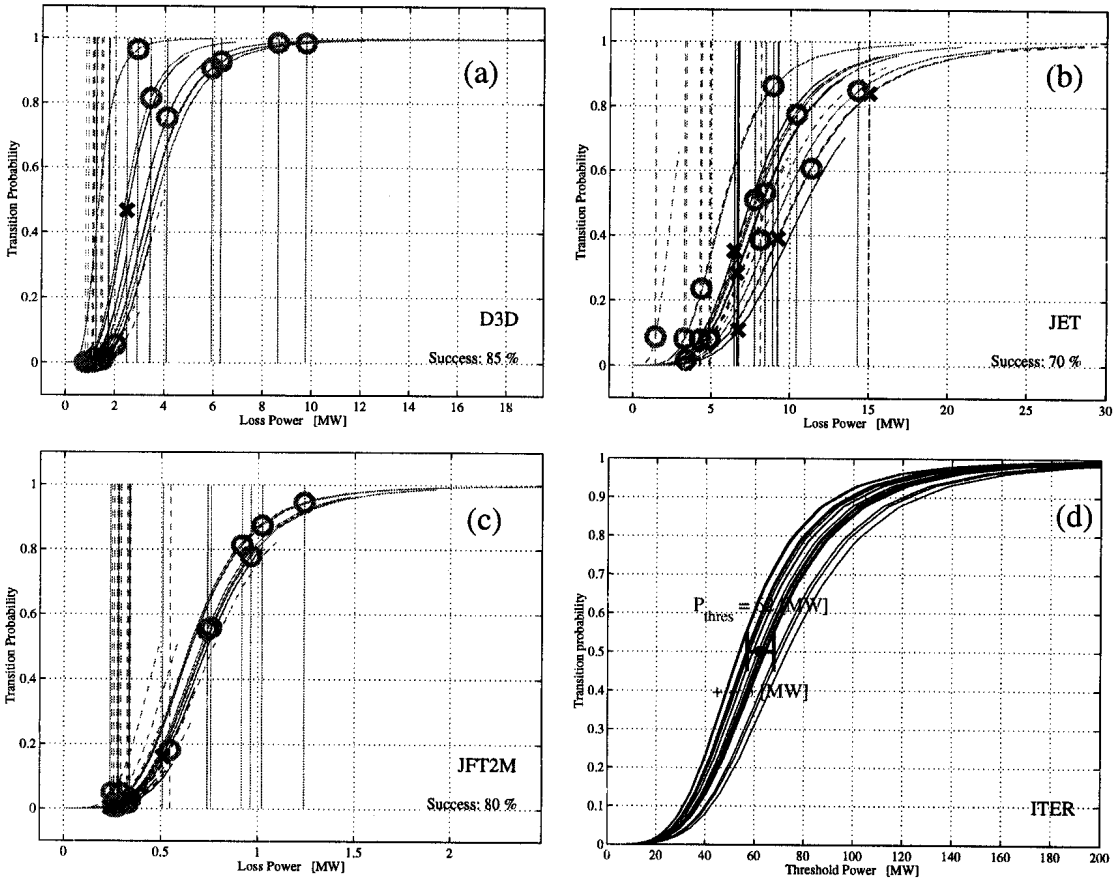

***Figure 1**: Prediction of the transition probability.*
a-c: tests for 3 tokamaks: DIII-D, JET and JFT2M. For each tokamak, 10 time slices in L-mode (dashed lines) and 10 in H-mode (plain lines) are randomly chosen. For each time slice, the Loss Power is scanned from 0 to twice the experimental value (vertical line) and the transition probability calculated over this range (curved lines). The intersection between the corresponding lines is shown by a symbol: A circle when the prediction is in agreement with the experimental phase and a cross if the test is negative.
d: application to ITER. The different lines correspond to 10% random perturbations around the ITER design values. The model described in row 3 from Table 1 has been used for these tests and application.

RESULTS FROM DISCRIMINANT ANALYSIS

At first, discriminant analysis was applied to data from the ITER threshold database and the input variables were those from the conventional scaling laws: n_e, B_t, R and P_{Loss}. The two classes consisted of time slices taken during the L mode phase and those at the LH transition. The classification ability was not good. An improvement was gained by adding the plasma elongation and surface area as well as incorporating all the pair products of the input parameters. With these additions, the classification succeeded for about 70 % of the test data, but the extrapolation to ITER values was diverging because of the linear characteristics of the classifier. This problem disappeared when the logarithm of the input parameters was used in the calculation. Utilising the SELDB2 selection criterion (SELDB2 is based on the experience gained by the experimentalists of each device to define data at the transition which are supposed to yield low power threshold values for each tokamak) and using a model without the pair products, a reasonable classifier has been found. The numbers associated with this classifier are summarised in the first row of table 1.

The second row in table 1 corresponds to the discrimination between the L mode and H mode time slices, with the "strong" SELDB2 selection criteria generally used [1] replaced by a condition which keeps dW/dt small only. The ITER power threshold lowered but the precision gained by the increase in statistics is lost by the larger diversity of the data, due to the absence of the SELDB criteria.

In order to increase the statistics without deteriorating the quality of the data, all 3 global databases (i.e. standard datasets of L-mode, H-mode and Threshold databases) have been merged together. However, only data from tokamaks represented in the L- and H-mode databases were kept. The predicted threshold power in ITER prediction based on this combined database is 63+/-5MW (row 3 of Table 1) . Figure 1 shows the transition probability for 3

	Asdex	AUG	C-MOD	Compass	DIII-D	JET	JFT2-M	JT60-U	TCV	Test 1	Test 2	Test 3	ITER
1	135 85 %	87 60 %	181 50 %	8 100 %	216 65 %	303 55 %	109 50 %	25 50 %	66 50 %	0.33 65%	0.34 53%	65%	191 +/- 75
2	298 65 %	315 70 %	465 60 %	15 55 %	309 50 %	241 55 %	778 95 %	10 100%	34 50 %	.48 72%	.47 69%	59%	103 +/- 69
3	712 85 %	302 70 %	471 70 %	31 0 %	609 85 %	902 75 %	522 80 %	19 80 %	48 50 %	.64 66%	.61 65%	70%	63 +/- 5
4	235 80 %	103 75 %	172 70 %	4 0 %	236 95 %	291 85 %	154 40 %	12 65 %	33 90 %	.97 83%	1.02 82%	75%	111 +/- 35

***Table 1**: ITER prediction results for different cases of data selection, described in the text, and numbered from 1 to 4. Under the tokamak names appear the number of points used in both classes and the rate of success of the prediction of the power threshold. The "Test 1" column shows the two quality estimators of the classification caculated on the data set. "Test 2" contains the same estimators but calculated on the test population. "Test 3" presents the global success rate of the LH power threshold on the experimental data. In the ITER column appear the predicted value of power threshold and its uncertainty (for its determination: see text)*

tokamaks and for ITER. However, the fraction of H-mode data compared to L-mode data was rather large (80%); the reduced classification quality is due to this unbalanced population. In the 4th case, we restricted the data in H-mode to a randomly selected subset with its size equal to the L-mode subset and all the pair products were used in the model. The quality of the discrimination is quite good and the uncertainty of the ITER prediction is also rather low.

From table 1, the determination of a unique value of the ITER power threshold appears as a trade-off between the classifier quality and the uncertainty in the prediction. Different tests have been performed in an attempt to get a better determined value for the ITER prediction: a) when removing one tokamak at a time, small variations in the ITER predictions have been observed (less than 25% in all the above mentioned models), b) when adding noise to the input data, the classification and the ITER prediction diverge with a certain rate from the values shown in Table 1. This rate indicates the stability of the prediction value. These different tests, performed on the 4 different models, give a large number of predicted values for the ITER threshold power. A weight, function of the classification quality, the model stability and the prediction variance, has been assigned to these predicted values. The weighted average leads to a prediction of the ITER threshold power of 80 MW +/- 25 MW.

SYSTEM IDENTIFICATION AND NEURAL NETWORKS.

Almost all the presented classifiers so far are of the 1st degree, and therefore all the parameters are important. Since the major advantage of the system identification technique [6] is the removal of unnecessary parameters, nothing is gained by this method and the results are quite similar to those obtained by discriminant analysis. Neural networks with different architectures, number of hidden layers and selection of input parameters have also been tried. With resulting success rates between 60 and 70 %, none of these models gave better results than discriminant analysis. Nevertheless, the ITER predictions were in the same range as that obtained from discriminant analysis.

DISCUSSION - CONCLUSION

The discriminant analysis, as a tool to predict the threshold power for ITER, has some advantages and disadvantages. The mathematical expression of the function is much more complicated than a simple power law (3 terms per parameter plus a mapping function between the new co-ordinate and the probability function). However, this method gives rise to more confidence in the scaling law results. The predicted values from the two methods converge to approximately the same value and the simple scaling laws are based on data taken at the transition whereas the results obtained with discriminant analysis used only L-mode and H-mode data.

[1] Ryter F. et al. Nucl. Fusion, 1996, Vol 36, No 9, 1217.
[2] Takizuka T. et al., 16th IAEA Fusion Energy Conf., Montreal, 1996, IAEA-CN-64/F-5.
[3] Snipes J. et al, Proc. 24th EPS conf. on Contr. Fus. and Plasma Phys., Berchtesgaden, 1997, Vol 21A, part III, 961.
[4] Righi E. et al, Plasma Phys. & Contr. Fus., 1998, Vol 40, No 5, 857.
[5] ITER Physics Basis (section II.4.3), submitted to Nuclear Fusion.
[6] Martin Y. & Buehlmann F., Plasma Phys. & Contr. Fus., 1998, Vol 40, No 5, 697.

Plasma Rotation across the H-mode Transition in TCV

B. P. Duval, F. Hofmann, Y. Martin, J.-M. Moret, H. Weisen

Centre de Recherches en Physique des Plasmas, Association EURATOM - Confédération Suisse, Ecole Polytechnique Fédérale de Lausanne, CH-1015 Lausanne, Switzerland

INTRODUCTION

The poloidal rotation velocity of intrinsic Carbon impurities has been measured spectroscopically across an L→H mode transition on TCV[1]. The H-mode transitions were obtained with ohmic heating only so the toroidal rotation is not expected to be important. In a tokamak, the

$$\mathbf{1)} \quad B_\Phi = B_\theta \times \frac{R}{a} \times q \approx 3\text{-}10 \times B_\theta$$

R, a are the major and minor radii
B are the magnetic field components
q is the local safety factor

toroidal magnetic field is larger than the poloidal field Eqn 1). Thus, from the first order force balance equation Eqn 2)[2] on the ion species, a measurement of the radial electric field depends most strongly on the product of the poloidal velocity and the toroidal magnetic field.

$$\mathbf{2)} \quad Er = \frac{\nabla p}{Zen} - (v \wedge B)$$

Er is the radial electric field
v, B are the velocity and magnetic field vectors
p is the local ion pressure

In the current models of plasma transport barriers[3], **ExB** velocity shear is thought to stabilise turbulence which results in reduced transport. For the H-mode, this transport barrier occurs in the plasma edge[3] where strong local $\mathbf{E_r}$ gradients are often observed. By simultaneously observing CIII and CV ion species, corresponding to different minor radial locations in the plasma, the behaviour of the radial electric field across the strong density and temperature gradients in the edge of a TCV H-mode plasma has been measured.

EXPERIMENTAL SETUP

Collimated light from TCV is fed via a 1.5mm diameter quartz fibre to a 1m Czerny-Turner spectrometer equipped with a 2400 l/mm grating and a PARC blue-enhanced OMA III detector system. This arrangement uses the proximity of line radiation from CV (227nm) and CIII (229nm) to simultaneously image two spectral features onto the detector. The ionisation energies of 392eV and 48eV respectively imply that on TCV CV is emitted from part of the plasma bulk whereas CIII reflects the parameters of the plasma boundary.

At the observed plasma region, the collection optics has a diameter of ~3cm with a strong axial emphasis. The H-mode transition was obtained with a Single Null configuration with the divertor on the machine floor and the ion gradient drift in the direction of the X-point (Fig 1). The position of the observation chord, shown in Fig 1a), was scanned from the outer plasma tangent inwards until the ratio in the observed CV/CIII line intensities increased. Since the CV radiation shell is relatively large for a 600eV central electron temperature, this procedure localises the observation chord where the pre-H-mode CV ionisation state becomes important which was found to be 2-4cm inside the LCFS with the CIII emission recorded from outside this region.

The OMA software was set to record ~50 pixels in the region of each spectral feature with a repetition time of ~2.5ms. With a spectral resolution of ~ 0.01nm/pixel and spectral HWHM in

Fig 1) SND configuration on TCV used for these experiments. The vertical lines show the lines of sight of the fibre optic telescope optics and the plasma is shown by the magnetic flux contours.

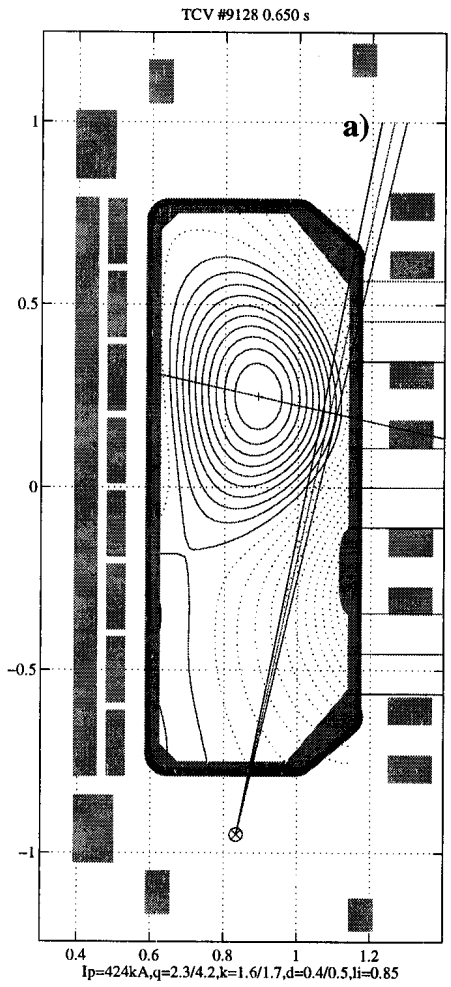

Fig 2) The main plasma parameters and the CV and CIII line intensities across the H-mode transition in TCV shot #9128. The vertical line indicates the transition time.

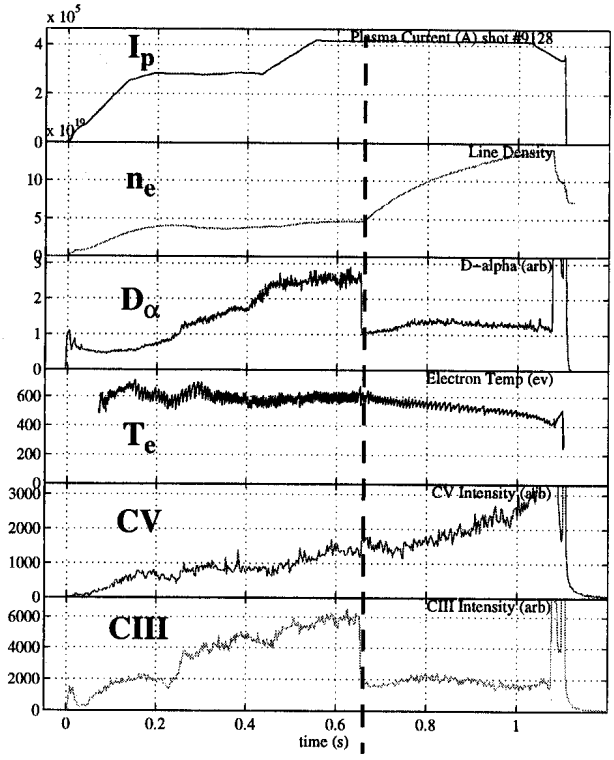

the range of 2-4 pixels, enough radiation was available to obtain good spectral fits throughout the TCV discharge. After acquisition, the data was analysed by a least squares fit code where the spectral line height, width and position were free parameters. Since the line width is >5x smaller than the spectral line feature, the fit base level could be left free or fixed at zero.

H-MODE FEATURES

Fig 2 shows the principal plasma parameters across the L→H transition for the experimental configuration. A current ramp, terminating after 0.55s, is followed by a density rise with the sharp drop in Dα at 0.65s indicating the H-mode transition. The central electron temperature, measured by a filtered diode pair, is ~600ev over the transition which is followed by the uncontrolled density rise associated with the elm-free high confinement regime[1]. The CIII intensity shows the same behaviour as Dα, dropping sharply at the transition, whereas the CV intensity is constant across the transition and rises with the plasma density buildup.

The results of the least squares fits are shown in Fig 3) with the spectral HWHM shown in pixels and interpreted as an ion temperature. The CIII ion temperature increases by less than 50% after the transition and the line intensity remains at ~30% of the pre-transition value despite the strong density rise. The CV behaviour is quite different. The ion temperature increases by ~130% and is sustained throughout the H-mode. These observations support the interpretation of the CIII radiation pertaining to a region close to or outside the LCFS and the CV radiation reflecting the plasma parameters inside the LCFS. The steep rise in the ion temperature and its gradient in the plasma edge accompanying the transition effectively squeeze the CIII emission

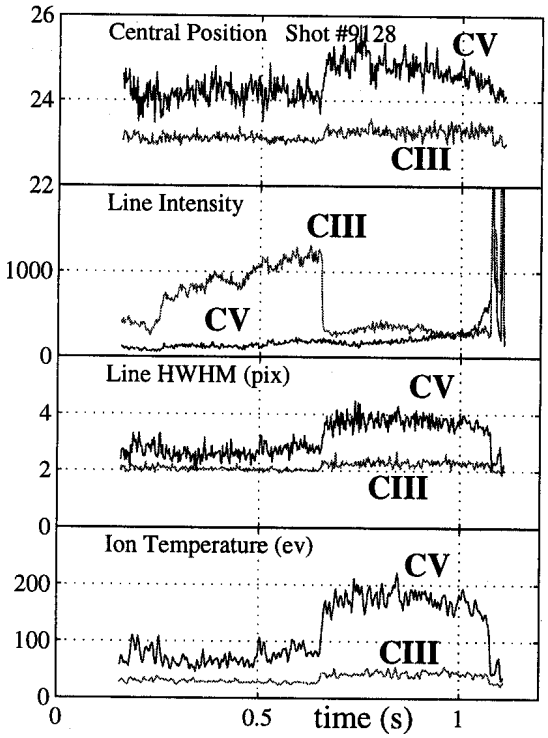

Fig 3) Shows the fit parameters for CIII and CV across the H-mode transition in shot #9128.

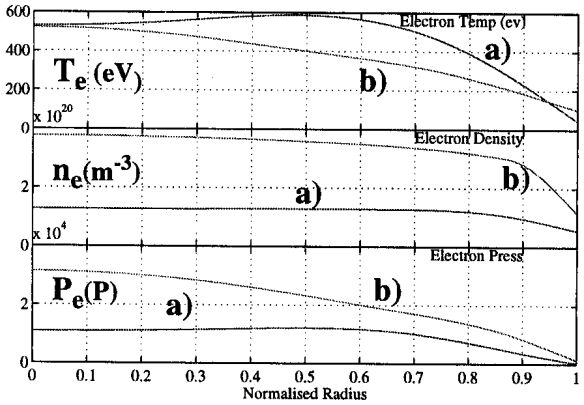

Fig 4) Electron temperature, density and pressure profiles a) at 0.6s, before the transition and b) at 1.0s, well into the density rise, from fits to the Thomson Scattering data.

region, and the ion temperature rises due to the increased collisionality and higher edge electron temperatures whose profiles were measured by Thomson Scattering, Fig 4.

POLOIDAL ROTATION

Fig 5) shows the gaussian least square fits for the CV data through the discharge and an enlargement of the period of the H-mode transition. There is evidence that the poloidal rotation spin-up occurs before the H-mode transition which was seen for several similar discharges. Since the CIII intensity drop is simultaneous with that of Dα the velocity buildup appears to commence up to 10ms before the transition itself, although it should be noted that the 2.5ms time resolution is insufficient to categorically exclude an experimental uncertainty. The raw data with the fitted profiles for each of the time slices near the transition is also shown as an indication of the good data quality. The poloidal rotation, which is unmeasurable before the transition, shows a 10km/s jump at the transition and then decreases as the plasma density increases. It is tempting to note that the high density disruption, where the plasma current is decreasing, the poloidal rotation approaches the pre-transition value, although, as noted, the electron and ion temperatures are also decreasing as the plasma density evolves to what is more probably the TCV density limit. There is a smaller 2km/s jump in the CIII poloidal velocity which evolves little during the H-mode already indicating a strong shear in the plasma edge.

RADIAL ELECTRIC FIELD

In order to calculate the radial electric field, each of the terms in equation 2) must be examined. Since there is no direct measurement of the impurity ion and temperature profiles in the plasma edge on TCV, the collisional force must be estimated from the measured electron profiles, Fig 4). The charge state profiles were calculated with a 1D transport code with a diffusion coefficient of $0.7m^2/s$, with the impurity density deduced from the Z_{eff} (value ~2) which was conservatively assigned to the Carbon impurity alone. Even in this extreme case, the contribution to the deduced E_r from the ion pressure gradient is estimated at less than 15% during the H-mode phase, where the edge gradients are strongest, and significantly less in the preceding L-mode phase.

The magnetic field in the observation region was taken from the TCV magnetic reconstruction code LIUQE. Although the current density profile is not yet directly measured on TCV, the reconstructed values are accurate in the plasma edge where almost all the plasma current is en-

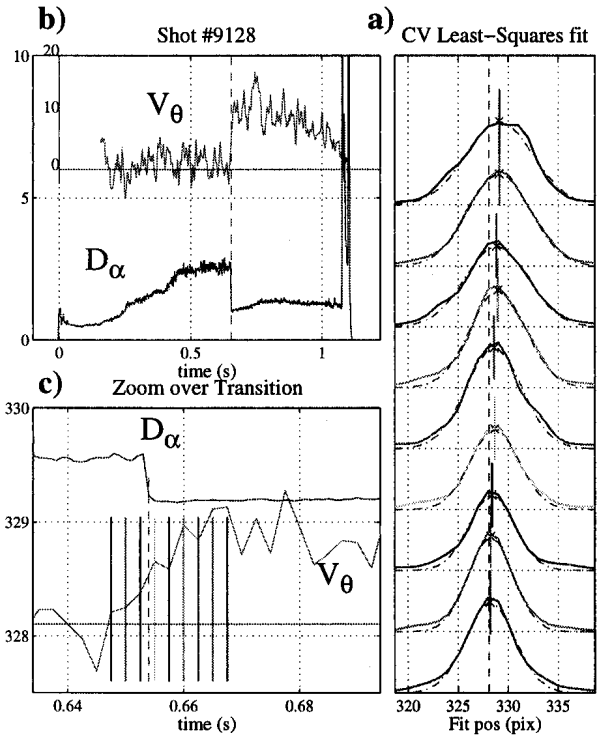

***Fig 5) CV data** a) shows the least squares gaussian fits to the 2.5ms separated time slices. b) Lower trace show Dα intensity and upper trace the calculated Poloidal rotation velocity in km/s. c) shows an expanded view of Dα and the gaussian fit position across the H-mode transition (dashed vertical line). Solid vertical lines indicate the acquisition times.*

closed by the outer flux surface. The poloidal field in elongated plasmas is higher than for an equivalent circular shape, and for TCV shot #9128 the magnetic field components at the transition time are $[B_\theta, B_Z, B_\phi]$ = [0.03, 0.3, -1]T in the observation region (B_Z is the vertical component in the poloidal plane, Fig 1).

From the doppler shift to higher wavelengths and the negative magnetic field, (observed from above the machine), an inward radial electric field is deduced. This is then in the same direction as the ion pressure derivative term since the pressure is always peaked towards the plasma centre.

The calculated radial electric fields just after the L→H transition, in the absence of toroidal rotation or an important ion pressure term are:

For CIII E_r = -2.5kV/m

For CV E_r = -10kV/m

with the field for CV falling to close to the CIII value before the high density disruption that often terminates ELM-free H-modes on TCV. These values are in agreement with measurements of the radial electric field from carbon impurities on other machines[3] in the region of the LCFS.

DISCUSSION

These results can be compared to those on the low field side of limiter and diverted L→H transition configurations[4]. Data is not available for the high field side since the port access during this TCV operation period would have obliged the viewing chord to traverse the X-point. The data is in agreement with **ExB** velocity shear stabilisation of radial, fluctuation-driven transport, resulting in a sharp drop in the particle outflux leading to a transport barrier with CV emission located inside and reflected by the sharp drop in Dα and CIII radiation intensities located outside. The increase in $\mathbf{E_r}$, (inward in this case), and thus the deduced **ExB** shear *before* the transition is in causal agreement with the role of the shear in stabilising turbulence at the plasma edge giving access to the increased confinement regime. With improved time resolution, better observation optics, a larger number of observation chords and the introduction of a diagnostic CXRS beam line, these experiments will be extended to examine the question of causality more closely and to measure the behaviour at other radial locations and of other ionic species, including the main plasma ions.

1 Moret et al. Plasma Phys. Controlled Fusion **37**, A215- (1995)
2 Hinton et al. Rev. of Mod. Physics **48**, 239- (1976)
3 Burrell Phys. Plasmas **4** (5), 1499- (1997)
4 Burrell et al. Plasma Phys. Controlled Fusion **34**, 13 1869- (1992)

Direct measurement of the plasma equilibrium response in TCV

J.B. Lister, A. Coutlis[2], I. Bandyopadhyay[1], P. Vyas, R. Albanese[3], D.J.N. Limebeer[2], F. Villone[4], J. P. Wainwright[2]

CRPP-EPFL, Association Euratom-Confédération suisse, Lausanne, Switzerland

[1]*Institute For Plasma Research, Bhat, Gandhinagar, India*

[2]*Centre for Process Systems Engineering, Imperial College, London, UK*

[3]*Associazione Euratom-ENEA-CREATE, Università Degli Studi Di Reggio Calabria, Italy*

[4]*Associazione Euratom-ENEA-CREATE, Università degli Studi di Cassino, Cassino, Italy*

ABSTRACT This paper presents a new technique and results for the estimation of the open loop frequency response of the plasma equilibrium, avoiding disadvantages of previous closed loop comparisons. The results are compared with the CREATE-L model [1]. A circuit equation model has been developed and compared with the experiments. An alternative "Grey Box" modelling method combines features of both theoretical and experimental techniques and provides further insight into the plasma response.

1. INTRODUCTION On most tokamaks, controllers are low order (proportional integral derivative), based on simple plasma response models or tuned empirically. Modern control strategies all rely on the availability of an adequately accurate linear model. The ITER reliance on modern high-order controller design methods, lead us to test the methodology in TCV. This validation involves generating an appropriate linear model, validating it against experiment and designing a controller to qualify the method experimentally. The most prevalent method for modelling the plasma response is based on establishing relevant physical laws with appropriate simplifying assumptions. A second approach is system identification. A fit to experimental data determines a suitable mathematical model with no *a priori* assumptions. The main features of TCV for equilibrium response modelling are that it is unstable with a large number of inputs (18 independently powered PF coils) and a large number of outputs (6 control parameters used in these particular experiments), Fig.1. Complete details of this work and references are available [2].

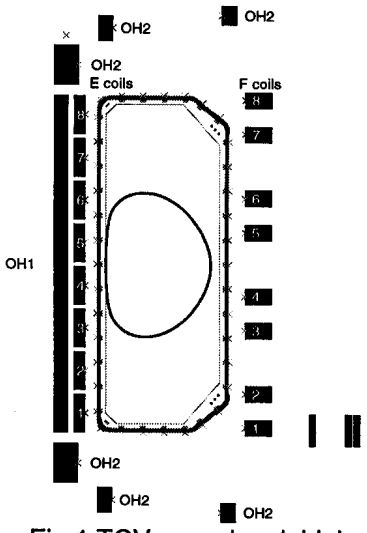

Fig.1 TCV vessel, poloidal field coils, poloidal field probes and separatrix

2. METHOD The open loop response cannot be measured by simply opening the feedback loops, since the vertical position of the plasma is unstable with an elongated plasma cross-section. However the open loop response can be recovered from closed loop data. In the block diagram of the TCV control loop, Fig.2, we identify a model for $G(s)$, using measurements of the voltage commands ($\boldsymbol{u}$) and the control parameters ($\boldsymbol{cp}$), taken at 5kHz over 0.5 s. Six electromagnetic parameters are considered: P_VERT (the radial flux imbalance measuring the radial position), TRI_OUT (the outboard field curvature) and TRI_IN (the inboard field curvature) define elongation and triangularity,

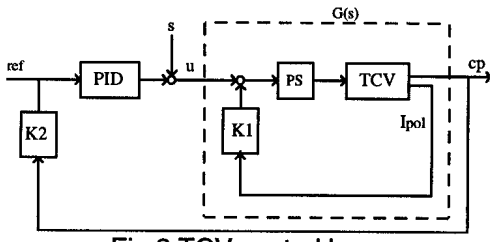

Fig.2 TCV control loop

I_p (the plasma current), zI_p (the product of the plasma current and the vertical plasma position). Ψ_R, the difference between the R^2I_p and $R_0^2I_p$ current moments, is the only parameter not under feedback control. All are estimated by linear combinations of fluxes, poloidal fields, and poloidal field coil currents. The E and F coils were excited symmetrically with respect to the horizontal mid-plane to form pairs driven in two modes, symmetric and anti-symmetric. This decouples the allowable motion for up-down symmetric and centred plasmas. A weakly shaped plasma with a low vertical instability growth rate (~$200s^{-1}$) was chosen. The main parameters were: R=0.87m, a=0.22m, B_ϕ=1.4T, I_p=200kA, κ_{95}=1.4, δ_{95}=0.23, q_a=4.6, n_e=$2.2\times10^{-19}m^{-3}$.

The excitation signal, *s* in Fig.2, contained 29 sine waves spanning the range 20 rad/s to 3000 rad/s, lying within 80% of the power supply limits. The response of all the measured signals at the driven frequencies was obtained by a least squares fit.

The frequency spectra of all of the input and output data were used to obtain the open loop frequency response. To identify a 1-output, *q*-input system we need to have performed *q* experiments. For the j^{th} experiment we define the input frequency spectrum as $U_l^j(\omega_i)$ and the output frequency spectrum as $Y^j(\omega_i)$, where *l* indexes the inputs. An estimate of the open loop frequency response at each measurement frequency is given by

$$\hat{G}(\omega_i)=\begin{bmatrix} Y^1(\omega_i) \\ \vdots \\ Y^q(\omega_i) \end{bmatrix}^T \begin{bmatrix} U_1^1(\omega_i) & \cdots & U_q^1(\omega_i) \\ \vdots & \ddots & \vdots \\ U_q^1(\omega_i) & \cdots & U_q^q(\omega_i) \end{bmatrix}^{-1} \quad (1)$$

3. MODELS We compare these measured open loop responses with those predictions of different plasma models.

A 'plasma-less' model, represents only the interactions between the applied voltages and the active currents, passive currents and diagnostic measurements.

The CREATE-L model [1] is a locally linearised representation of the response of a fully deformable equilibrium, derived from the PROTEUS non-linear model.

RZIP [2] is a circuit equation model of TCV based on the supposition that the plasma current distribution remains constant during any control action, but that its position can move vertically and radially and the total plasma current can change. Quantities dependent on the plasma current distribution are obtained by averaging over the reconstructed plasma current distribution. The Shafranov radial force balance and the conservation of poloidal flux weighted by the plasma current distribution are assumed.

4. RESULTS The plasma-less model was validated with a series of tests with no plasma. Where the variance of the estimates is low the model-estimate fit is extremely accurate. Typical errors lie within 1dB and 5 degrees for frequencies below 1000 rad/s, Fig.3. For small output responses, the estimate variance is poorer but the data never invalidate the model.

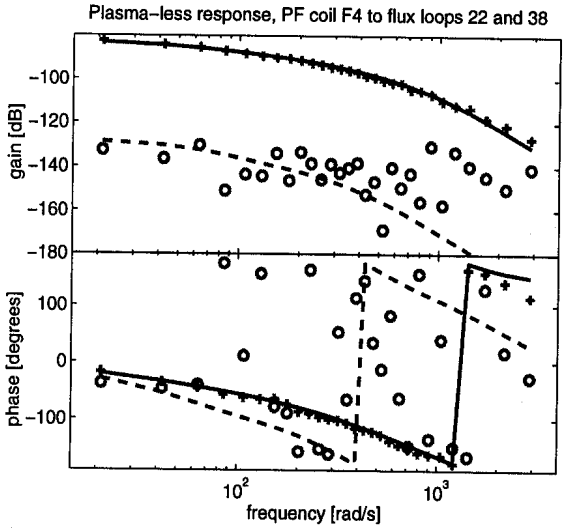

Fig.3 Modelled (curves) and measured (crosses and circles) responses of the plasma-less system

The experimental data from the anti-symmetric coil-pair experiments generated the zI_p frequency responses and a fitted model with a single unstable pole and 3 stable poles. The predictions of the growth rate are very close (213 s^{-1} measured compared with 209 s^{-1} for RZIP).

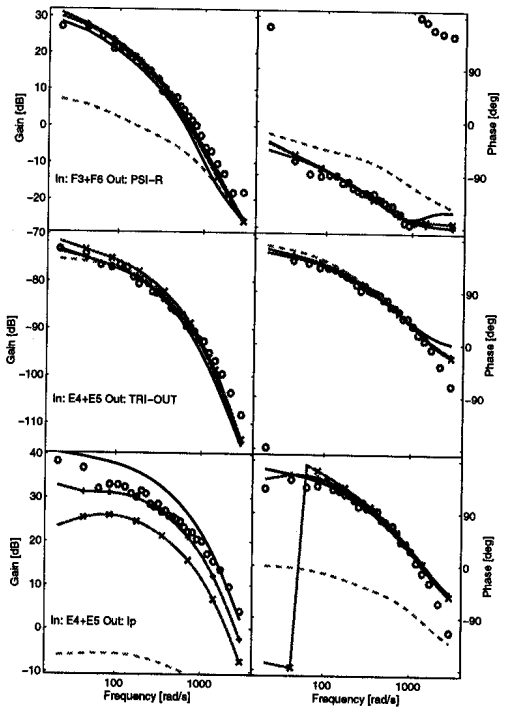

Fig.4 Symmetric frequency responses

The agreement for the symmetric responses is generally good, typified by Fig.4. The input-output pair F3+F6 to Ψ_R illustrates the most typical result - both plasma models agree with the experimental data, but the plasma-less model is incorrect. In a few cases, even the plasma-less model agrees, such as E4+E5 to TRI-OUT. For only some plasma moments the models can differ by more than the experimental variance, illustrated by E4+E5 to Ip. There is no significant difference between the reliability of the CREATE-L model or the RZIP model.

5. GREY BOX MODEL We have developed a hybrid approach to modelling which incorporates well defined *a priori* knowledge for part of the model and experimental data to identify the intrinsic plasma response. "Grey Box" modelling is particularly suited to our present problem due to the large number of known coefficients compared with the small number of uncertain coefficients. The RZIP circuit equations contain a large number of coefficients, most of which are independent of the presence of the plasma and can, in principle, be modelled or measured with unlimited precision. The plasma response part of the RZIP model is dominated by only six coefficients M_{33}, M_{34}, M_{43}, L_{p0}, Ω_p and Ω'_p [2]. Varying these defines our set of possible GBMs. We evaluated the 10×5 input-output transfer functions for up-down symmetric excitation at all frequencies. A simplex search on the six GBM parameters minimised a suitably chosen cost function and produced the 'Best GBM' (BGBM). A single parameter scan was performed on each element around the BGBM, Fig. 5. The parameter causing the most rapid variation of the cost function is L_{p0}, the plasma inductance. The next sensitive parameter is M_{33}, which defines the Shafranov equilibrium constraint. The parameters M_{34} and M_{43} have much shallower minima and predominantly define the interactions between the loop voltage and the position and between the vertical field and the plasma current. Finally, the resistive terms, Ω_p and Ω_p', are the most shallow.

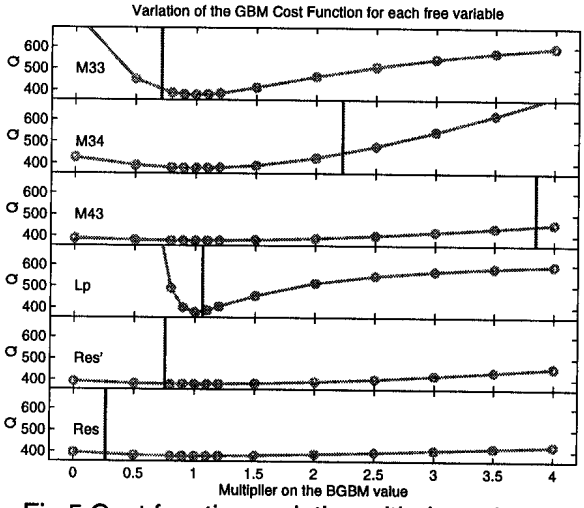

Fig.5 Cost function variation with the unknown elements of the circuit equations

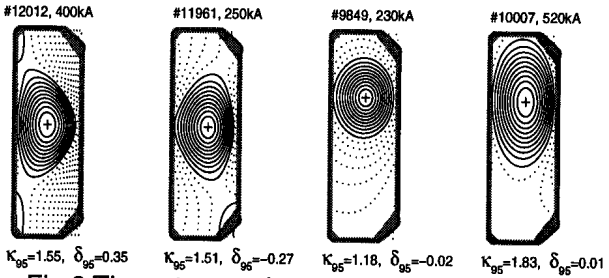

Fig.6 The extreme plasma shapes for which the RZIP model was calculated

The vertical lines indicate the values of the *a priori* model parameters. Fig.4 superimposes the BGBM model on the *a priori* transfer functions. Most are unchanged to the eye. The worst case of the plasma current response has been significantly rectified. Having located the BGBM, we floated the power supply time-constant, finding a minimum at 0.6 ms, and we floated the number of vessel eigenmodes required, finding that 15 eigenmodes should be included.

6. DISCUSSION We investigated whether the good agreement is limited to modest elongation. Fig.6 shows some extreme cases of elongation and triangularity. The dominant parameters vary little, whereas the parameters which vary the most are those with the least effect on the response. Fig.7 confirms this for selected input-output pairs. We tested two even simpler models, assuming a circular parabolic plasma current distribution and one with the ellipticity of the outer magnetic surface. Fig. 8 confirms the insensitivity to the current profile, although the model remains dependent on the plasma position.

ACKNOWLEDGEMENTS This work was partly supported by Euratom mobility contracts (FV [ENEA] and AC [UKAEA]) and partly by the Fonds national suisse de la recherche scientifique.

REFERENCES

[1] R. ALBANESE and F. VILLONE, Nucl. Fusion **38** (1998) 723.

[2] A. COUTLIS et al., Lausanne ReportRP 606/98 (1998)

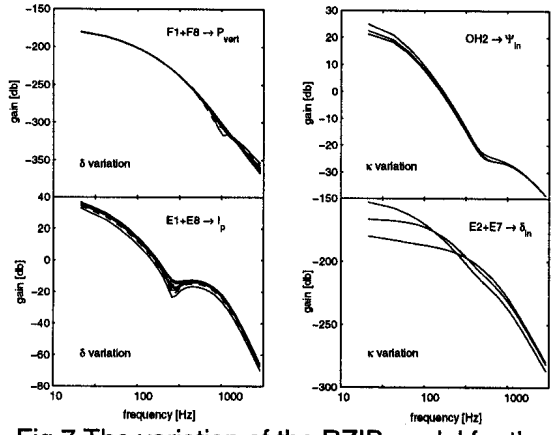

Fig.7 The variation of the RZIP model for the equilibria in Fig.6

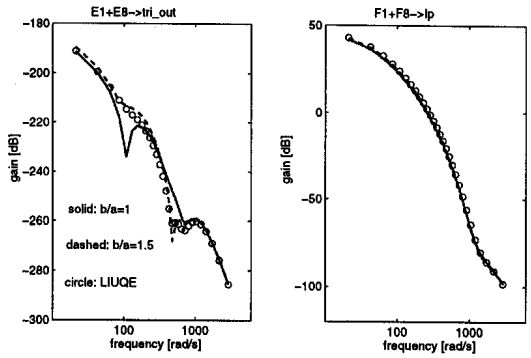

Fig.8 Transfer functions for the nominal RZIP model (circles), the model with circular current distribution (solid curves) and the model with elliptical profile (dashed curves)

First Measurements of the Faraday Rotation on Plasmas in TCV

S. Barry, C. Nieswand and S. L. Prunty*

Centre de Recherches en Physique des Plasmas, Ecole Polytechnique Fédérale de Lausanne, Association EURATOM - Confédération Suisse, CH-1015 Switzerland

**Department of Electrical Engineering and Microelectronics*
University College Cork, Association EURATOM-DCU. Ireland

1. Introduction

Polarimetry is a well known technique used to determine the magnetic field structure in tokamaks since it was first proposed by DeMarco and Segre[1,2]. Recently a far-infrared (FIR) interferometer/polarimeter technique which allows the Faraday rotation induced by the plasma to be deduced from a phase measurement was developed[3] (Method 1). The 14 channel polarimeter upgrade of the FIR interferometer on TCV is based on a modification of this method[4,5] (Method 2). It has been shown that the accuracy of the TCV equilibrium reconstruction will be substantially improved by including polarimeter data[6]. To prove a useful tool the TCV polarimeter was seen to require a precision of $\pm 0.2^0$ Faraday rotation. Due to a serious vacuum problem the TCV opening lasted much longer than predicted and we are unable to present results from actual TCV plasmas.

2. The Polarimeter/Interferometer on TCV

The Tokamak à Configuration Variable (TCV) is a compact medium sized (R=.88m, a=.24m) highly elongated tokamak capable of producing limited and diverted plasmas with currents up to 1 MA. The machine has been designed to produce many diverse plasma shapes without requiring hardware modifications.

An overview of the TCV polarimeter/interferometer system is shown in Fig. 1. The instrument is of Mach-Zehnder type where the probe and local oscillator (LO) beams are transferred from the laser room to the tokamak by means of oversized dielectric waveguides. The probe beam is then expanded into a slab-like beam and traverses TCV from bottom to top via large windows. The absorption of the operating wavelength of 214 μm in air is quite significant so all the optical elements have been placed in boxes, which, along with the waveguides, have been flushed with dry N_2. The LO is similarly expanded and combined with the probing beam on a large beam-splitter. A system of waveguides focuses the horizontal beams from the main beam combining device onto the detectors. The detection system consists of an array of 15 liquid Helium cooled InSb hot electron bolometers supplied by QMC Instr. Ltd.. A half-wave plate, mounted in a precision rotator, was placed in the path of the probe beam in order to calibrate the polarimeter measurement. A reference signal unaffected by the plasma is also provided.

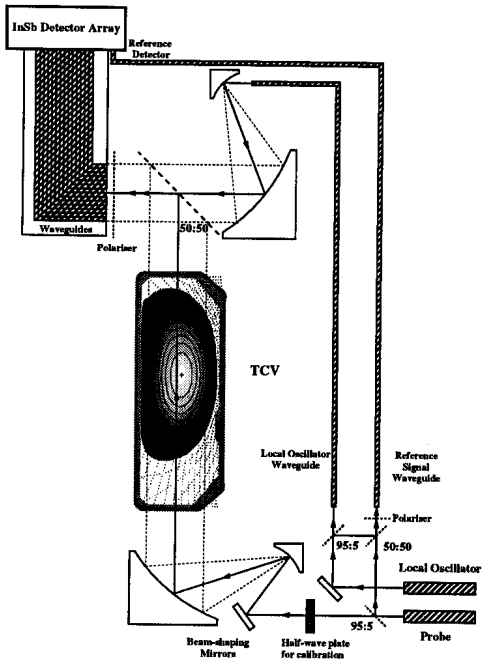

Figure 1: *Overview of the TCV polarimeter/interferometer*

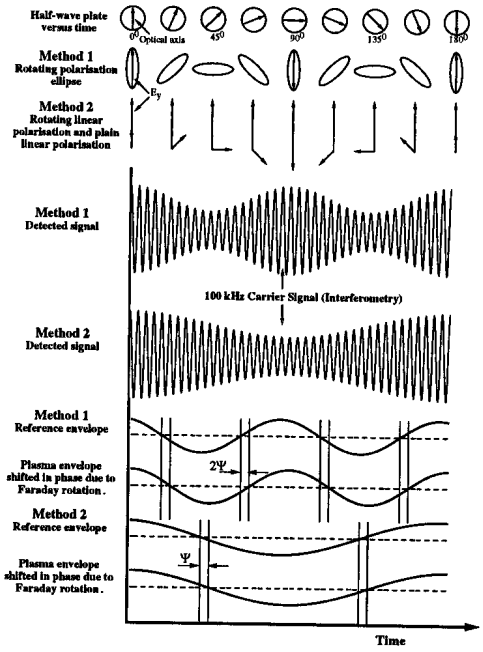

Figure 2: *Schematic of the two interferometer/polarimeter methods.*

3. System Description

Methods

Method 1, shown schematically in Fig. 2, uses a rotating elliptically polarised probing beam and a frequency shifted local oscillator (LO). The beat signal between the beams is a modulated waveform where the Faraday rotation Ψ, can, after some filtering, be extracted from the phase shift of the modulation envelope and the interferometer information from that of the carrier signal. Therefore, both the interferometer and polarimeter data can be measured using only one detector per channel. It was shown that this method is limited by an additional time-varying phase term which is superimposed on the required interferometer data[7]. This extra term can be effectively removed by low-pass filtering the interferometer data with the subsequent loss of time resolution.

Method 2, also shown schematically in Fig. 2, uses the combination of a rotating linearly polarised beam and a plain linearly polarised beam as the probing beam. This method produces signals similar to those obtained using Method 1 with the following differences; (a) the modulation is a purely cosine without higher harmonics; (b) the modulation frequency is lower by a factor of two; (c) the measured polarimeter phase shift is Ψ as opposed to 2Ψ and (d) the interferometer phase measurement is not corrupted by additional terms provided the difference in path lengths between the two probing beams is a multiple of π. Accordingly, the time resolution can be preserved.

The Optical Set-Up

The system, shown in Fig. 3, used to produce the probing and LO beams, was designed to incorporate both methods. The incident beam is split into the probing and

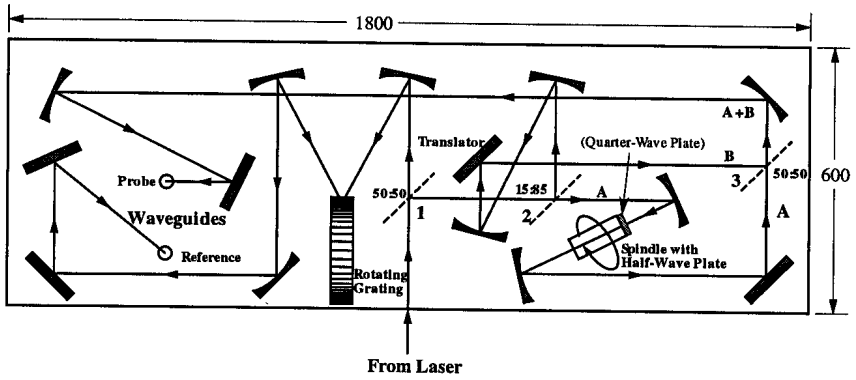

Figure 3: *The optical set-up for the production of the probe and LO beams.*

LO beams and the latter is reflected off a rotating grating to produce the frequency shift. A small fraction of the probe beam is directed through a $\lambda/2$ plate in a rapidly rotating spindle which rotates its polarisation. It is then recombined with the remainder of the beam on beam-splitter 3. The system can be changed over to Method 1 by simply removing beam-splitter 2 and turning the $\lambda/4$ plate at the entrance of the spindle to introduce some ellipticity into the polarisation of the probing beam.

4. Present State

Polarimeter

The polarimeter output for Method 1 and 2 showing steps of 0.4° Faraday rotation on two of the central channels are shown in Fig. 4 and Fig. 5 respectively. The time resolution in both cases is 4 ms. The precision of Method 1 is seen to be the required 0.2° Faraday rotation while that of Method 2 is 0.2° → 0.3°.

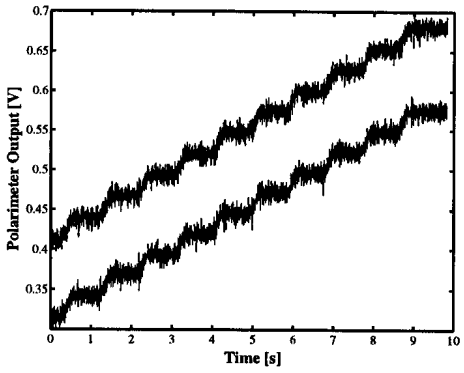

Figure 4: *Polarimeter output for Method 1 with steps of* 0.4° *Faraday rotation.*

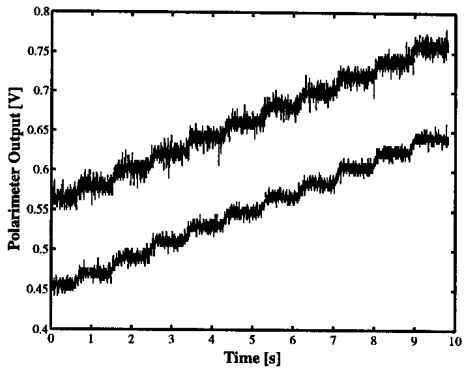

Figure 5: *Polarimeter output for Method 2 with steps of* 0.4° *Faraday rotation.*

Interferometer

The interferometer outputs for both Methods 1 and 2 with a Faraday rotation of 40° and modulation indices of 0.48 and 0.4 are shown in Fig. 6 and Fig. 7, respectively. Both signals are seen to have a additional time-varying phase terms which are dependent on both Faraday rotation and modulation depth. The additional term in Method 1 is much

larger than that of Method 2 and as it is inherent to that method cannot be removed. The term in Method 2 is probably due to a non-zero phase difference between the path lengths of the two probing beams and can possibly be reduced by a finer adjustment of the translator installed for that purpose (see Fig. 3). During bench tests it was shown that this term could be set to zero[5].

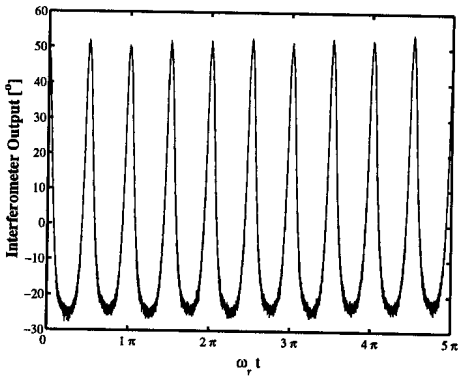

Figure 6: *Interferometer output for Method 1 with* $\Psi = 40°$ *and* $m = 0.48$ *where* ω_r *is the rotation frequency of the* $\lambda/2$ *plate.*

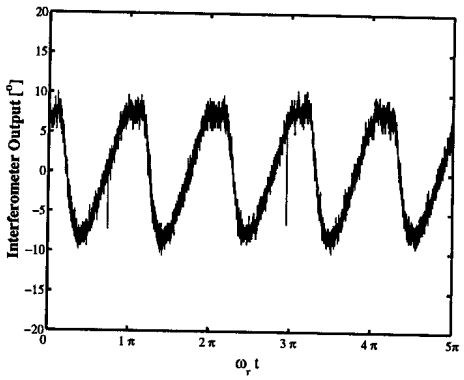

Figure 7: *Interferometer output for Method 2 with* $\Psi = 40°$ *and* $m = 0.4$ *where* ω_r *is the rotation frequency of the* $\lambda/2$ *plate.*

5. Conclusions

The method and system description of the new TCV multichannel FIR polarimeter/ interferometer has been presented. It is based on a system installed on MTX and retains its major advantages with the additional advantage that the extra interferometer phase term is much smaller and can possibly be reduced or even removed completely. The precision of both polarimeters is at or very close to the 0.2° required to enhance the precision of the TCV equilibrium reconstruction.

Due to a serious vacuum problem the TCV opening has lasted much longer than predicted and we are, therefore, unable to present results from actual TCV plasmas.

Acknowledgments

This work was partly funded by the Swiss National Science Foundation.

References

[1] F. DeMarco and S.E. Segre, *Plasma Phys.* **14**, 245 (1972).

[2] S.E. Segre, *Plasma Phys.* **20**, 295 (1978).

[3] B.W. Rice, *Rev. Sci. Instrum.* **63**, 5002 (1992).

[4] S. Barry, C. Nieswand, F. Bühlmann, S. Prunty and H. Mansfield, *Rev. Sci. Instrum.* **67**, 1814 (1996).

[5] S. Barry, C. Nieswand, S. Prunty, H.M. Mansfield and P. O'Leary, *Rev. Sci. Instrum.* **68**, 2037 (1997).

[6] F. Hofmann and G. Tonetti, *Nucl. Fusion*, **28**, 1871 (1988).

[7] W.R. Geck *et al*, *Rev. Sci. Instrum.* **66**, 850 (1995).

Simulation of Ion-Temperature-Gradient-Driven Instabilities in Axisymmetric and Helical Configurations[1]

K. Appert, S. Brunner, M. Fivaz, **T. M. Tran**, J. Vaclavik and L. Villard
Centre de Recherches en Physique des Plasmas, Association Euratom-Confédération Suisse, Ecole Polytechnique Fédérale de Lausanne, PPB, 1015 Lausanne, Switzerland

Introduction

ITG instabilities are now commonly held responsible for turbulence giving rise to anomalous ion heat transport in the core of tokamaks. As collisional transport has been optimized in modern stellerators such as W7X, ITG turbulence could become the dominant transport mechanism in these devices. We therefore started a program with the long-term goal of modeling global microinstablities in various magnetic configurations, using the gyrokinetic (GK) theory.
The linear stability analysis is conducted by two independent approaches: (1) the spectral method which consists of solving an eigenvalue problem derived from the linearized GM equations and (2) the Particle-In-Cell (PIC) simulation of the time-evolution of a plasma in phase-space. These two complementary approaches allow extensive benchmarking and comparisons. The second approach lead to the development of the `GYGLES` code for linear problems in *toroidal geometry* and a modified version to simulate the ITG in *helically symmetric* configurations.
We are also developing a new 3D *nonlinear* global PIC code in toroidal geometry to examine the saturation of the ITG instabilities and the associated anomalous transport. Our current efforts in this development are the convergence and the conservation properties which are required to validate the numerical model.
In the following, the GK equations and numerical techniques used in the PIC codes will be reported, together with some results obtained from the linear codes.

Gyrokinetic simulation model

The model is based on the gyrokinetic equation for the ions, an adiabatic response for the electrons, the quasi-neutrality condition and the electrostatic approximation. By writing the ion gyro-centre distribution function as

$$f(\vec{R}, v_{\|}, \mu, t) = f_0(\vec{R}, v_{\|}, \mu) + \delta f(\vec{R}, v_{\|}, \mu, t) \tag{1}$$

where f_0 describes the plasma equilibrium, the nonlinear time evolution of δf is given by

$$\left[\frac{\partial}{\partial t} + \vec{v}_{gc}\cdot\nabla + \dot{v}_{\|}\frac{\partial}{\partial v_{\|}}\right]\delta f = -f_0\left[\frac{\langle\vec{E}\rangle\times\vec{b}}{B}\frac{\nabla f_0}{f_0} + \frac{q_i\langle\vec{E}\rangle}{m_i}\cdot\left(\vec{b} + \frac{v_{\|}}{\Omega}\frac{\vec{b}\times\nabla B}{B}\right)\frac{1}{f_0}\frac{\partial f_0}{\partial v_{\|}}\right], \tag{2}$$

$$\vec{v}_{gc} = v_{\|}\vec{b} + \frac{1}{\Omega}\left(\frac{v_{\perp}^2}{2} + v_{\|}^2\right)\frac{\vec{b}\times\nabla B}{B} + \frac{\langle\vec{E}\rangle\times\vec{b}}{B}, \quad \dot{v}_{\|} = \frac{v_{\perp}^2}{2}\mathrm{div}\vec{b} + \frac{q_i\langle\vec{E}\rangle}{m_i}\cdot\left(\vec{b} + \frac{v_{\|}}{\Omega}\frac{\vec{b}\times\nabla B}{B}\right), \tag{3}$$

where $\vec{b} = \vec{B}/B$ is the unit vector parallel to the magnetic field $\vec{B}$, Ω is the ion cyclotron frequency. The ion Larmor radius effect is taken into account through the gyro-averaged

[1]This work is supported by the Swiss National Science Foundation

electric field $\langle\vec{E}\rangle(\vec{R},v_\perp,t)=\int\vec{E}(\vec{R}+\vec{\rho},t)\,d\alpha/2\pi$. The quasi-neutrality equation, using the second order expansion in Larmor radius for the ion polarization density and adiabatic electrons provides an equation for the self-consistent electrostatic potential ϕ:

$$-\nabla_\perp\cdot\left(\frac{1}{B\Omega}\nabla_\perp\phi\right)+\frac{e}{T_e}\left(\phi-\bar{\phi}\right)=\frac{\delta n_i}{n_0}=\frac{1}{n_0}\int\delta f(\vec{R}=\vec{r}-\vec{\rho},v_\parallel,\mu,t)\,d^3v, \qquad (4)$$

where $\bar{\phi}$ denotes the magnetic-flux-surface-averaged potential and $d^3v=B\,dv_\parallel d\mu d\alpha$.
The 2-D equilibrium magnetic field can be represented as $\vec{B}=F\vec{u}+\nabla\psi\times\vec{u}$, where $F=F(\psi)$ and $\vec{u}=\nabla\varphi$ (for axisymmetry) or $\vec{u}=(hr\vec{e}_\varphi+\vec{e}_z)/(1+h^2r^2)$ (for helical symmetry). For axisymmetry, we take tokamak ideal MHD equilibria from the **CHEASE** code[1]. For helical configurations, we consider vacuum fields:

$$\psi=\frac{1}{2}b_0hr^2-c_0\ln r-r\sum_l b_lI_l'(lhr)\cos(l\zeta),\quad F=b_0+hc_0,\quad \zeta=\varphi-hz. \qquad (5)$$

The fields ϕ and δn_i are defined on a magnetic coordinate system (s,θ) where $s=\sqrt{(\psi-\psi_{\rm axis})/(\psi_{\rm bound}-\psi_{\rm axis})}$ and θ is a poloidal angle from the magnetic axis. The third coordinate φ (axisymmetry) or z (helical symmetry) is ignorable in the linear cases. In *linear* simulations, all the terms proportional to the electric field $\vec{E}$ appearing in $\dot{R}=\vec{v}_{gc}$ and $\dot{v}_\parallel$ are discarded: only the *unperturbed* GC trajectories are considered. Furthermore, only one Fourier mode in the ignorable coordinate of the potential ϕ and the perturbed distribution δf is considered. The numerics can be made even more efficient by extracting the fast phase variation in the poloidal direction[2], allowing thus to consider very high values of the toroidal and poloidal wave numbers in the *linear* simulations.
The particle δf discretization is done by introducing a particle "weight" w_p defined by

$$\frac{\delta f}{n_0}(\vec{R},v_\parallel,\mu,t)=\frac{1}{N/V}\sum_{p=1}^{N}w_p(t)\delta^3(\vec{R}-\vec{R}_p(t))\delta(v_\parallel-v_{\parallel p}(t))\,\delta(\mu-\mu_p)/2\pi B, \qquad (6)$$

where N is the number of macro-particles, V is the volume of the plasma and n_0 is the averaged ion density. The perturbed ion density in Eq. (4) can now be written as a sum over the particles as

$$\frac{\delta n_i}{n_0}(\vec{r},t)=\frac{1}{N/V}\sum_{p=1}^{N}w_p(t)\int\frac{d\alpha}{2\pi}\,\delta^3(\vec{r}-\vec{R}_p-\vec{\rho}_p). \qquad (7)$$

Using the *splines* as test functions and Eq. (6), the weak variational form of the quasi-neutrality equation Eq. (4) is written as

$$\int d^3r\left[\frac{1}{\Omega B}\nabla_\perp\phi\cdot\nabla_\perp\Lambda_\nu+\frac{e}{T_e}(\phi-\bar{\phi})\Lambda_\nu\right]=\frac{1}{N/V}\sum_{p=1}^{N}w_p(t)\int\frac{d\alpha}{2\pi}\,\Lambda_\nu(\vec{R}_p+\vec{\rho}_p), \qquad (8)$$

where we considered the 3D (2D in the linear cases) splines $\Lambda_\nu(\vec{r})$ up to the third order. The RHS of Eq. (8) specifies completely the scheme for the particle deposition on the grid. Expanding then the electric potential, using the same splines, the discretized electric field is finally obtained from:

$$\sum_{\nu'}A_{\nu\nu'}\phi_{\nu'}=b_\nu,\quad \phi(\vec{r},t)=\sum_\nu\phi_\nu(t)\Lambda_\nu(\vec{r}),\quad \vec{E}(\vec{r},t)=-\nabla\phi=-\frac{\partial\phi}{\partial s}\nabla s-\frac{\partial\phi}{\partial\theta}\nabla\theta-\frac{\partial\phi}{\partial\varphi}\nabla\varphi. \qquad (9)$$

Results

Benchmark of the linear PIC code with the spectral code [3]

A TFTR-like deuterium plasma is considered with $B_0 = 3.8\,\mathrm{T}$, $R = 2.58\,\mathrm{m}$, $a = 0.92\,\mathrm{m}$, $q_s(s) = 1.2 + 9.6s^3$. The electron and ion density and temperature gradients peak at $s_0 = 0.315$. At this position, the relevant parameters for local stability take the values $q_s = 1.5$, $\hat{s} = d\ln q_s/d\ln s = 0.6$, $T_e/T_i = 1.0$, $\epsilon_N = L_N/R = 0.29$, $\eta = L_N/L_T = 4.0$, $A^{-1} = 0.11$, corresponding to a state well above marginal stability. The frequencies ω and growth rates γ versus the toroidal wave number n are compared in Fig. 1, for the most unstable modes, showing a good agreement throughout most of the scan.

Magnetic drift reversal stabilization

At high pressure, the magnetic drifts can be reversed locally by the plasma diamagnetism and become stabilizing [4]. On the outer plasma mid-plane, the drift reversal condition can be quantified by the dimensionless parameter α_t:

$$-\mu_0\frac{dp}{d\psi} > \frac{1}{R}\frac{\partial R}{\partial \psi}B_t^2 \quad \Longrightarrow \quad \alpha_t \equiv -\mu_0\frac{R}{B_t^2}\frac{\partial p}{\partial R} > 1. \tag{10}$$

Using the linear code GYGLES, this stabilizing effect is shown in Fig. 2 with a JET-like equilibrium in the toroidal ITG regime ($n = 48$).

ITG modes in a straight heliac

We consider a heliac configuration with the following parameters: $b_0 = 1, b_1 = .5, b_2 = -.06, c_0 = .32, h = 1$ that has a magnetic axis radius $r_m = .76\mathrm{m}$, an average minor radius $\langle a\rangle = .61\mathrm{m}$, and an almost shearless $\tilde{q} = -1.505$. This implies that, contrary to tokamaks, the parallel wavenumber $k_{\|,m} = B_z(k + hm/\tilde{q})/B$ for a given poloidal wavenumber m in straight field line coordinate χ, is nearly constant across the plasma. The T_i profile has a maximum gradient at $s = .7$ that extends over a radial width $\Delta s \approx \pm.1$. The density is taken constant. The helical version of the GYGLES code was used for various L_T and $k_{\|,m}$. For low $k_{\|,m}$ values, the growth rate of ITGs shows a remarkable behavior with $1/L_T$ (see Fig.3 for $m = 6$). ITGs are stable until a critical gradient is reached ($a/L_T \approx .77$); then γ increases, reaches a maximum for $a/L_T \approx 4$, then falls down to complete stabilization for $a/L_T > 6$. These ITG modes are in the "slab" regime but can be stabilized by favorable averaged magnetic drifts, in agreement with the fluid dispersion relation also shown in Fig. 3. The critical gradients versus $k_{\|,m=6}$ are shown in Fig. 4.

Conclusion

While the linear PIC code GYGLES is in a production state as demonstrated in this report, the non-linear code is still in a development phase: the main difficulties found so far are to maintain the particle and energy conservation after the field saturation where strong non-linear wave-particle and wave-wave interactions take place.

On the other hand, a full 3D linear code, coupled to the 3D MHD equilibrium VMEC code is being constructed to study the ITG stability in non-axisymmetric configurations.

[1] H. Lütjens et al., *Comp. Phys. Comm.*, **97**, 219(1996).
[2] M. Fivaz et al. *to appear in Comp. Phys. Comm.* (1998).
[3] S. Brunner et al. *submitted to Phys. Plasmas* (1998).
[4] M. Fivaz et al. *Phys. Rev. Lett.*, **78**, 3471(1997)

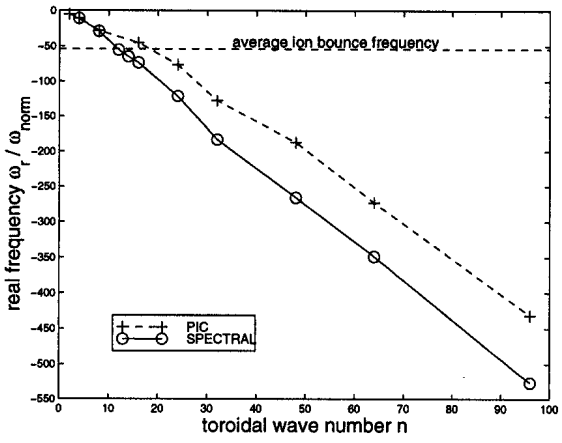

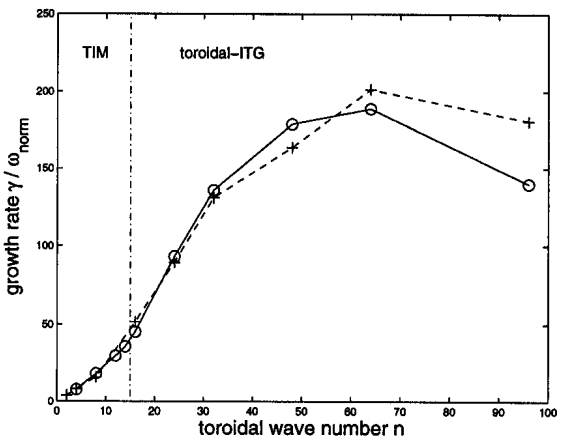

Figure 1: The most unstable modes versus the toroidal wave numbers n, compared with the the spectral code, for a TFTR-like plasma.

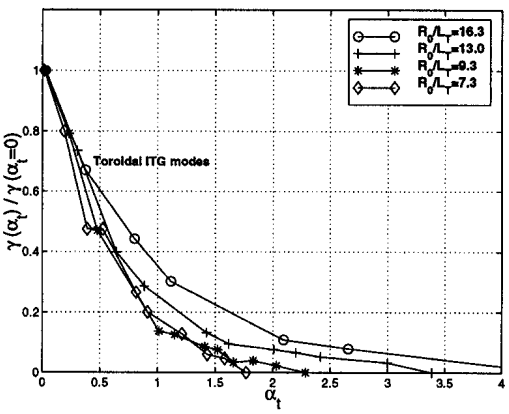

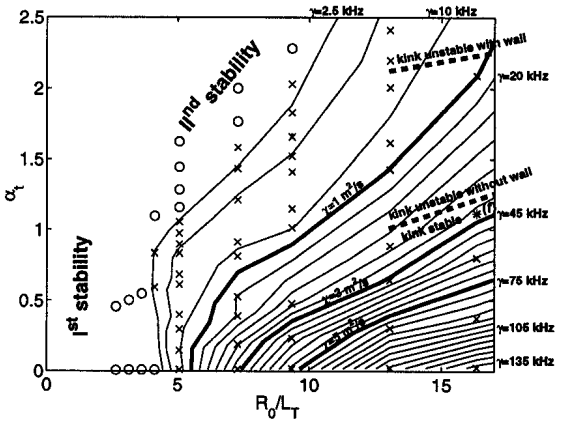

Figure 2: Stabilization by the magnetic drift reversal in the toroidal ITG regime with $n = 48$, for a JET like tokamak

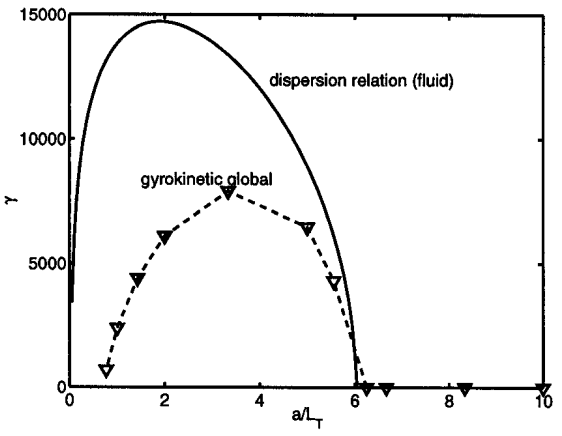

Figure 3: Growth rate versus the temperature gradient is a straight heliac for $k_{\|,m=6} = 0.03$

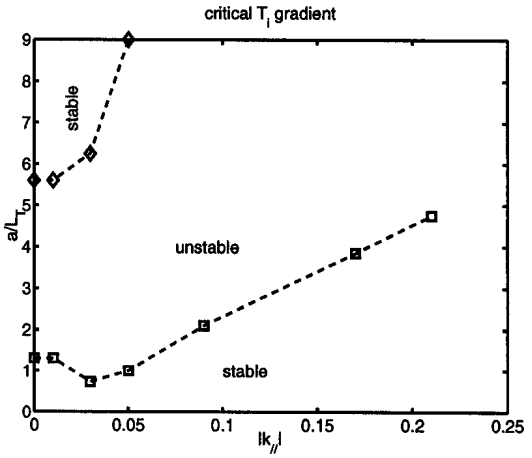

Figure 4: ITG critical gradients versus $k_{\|,m=6}$ in a straight heliac

Mapping of a Stochastic Magnetic Field in a General Configuration

O. Fischer and *W.A. Cooper*
Centre de Recherches en Physique des Plasmas,Association Euratom-Confédération Suisse Ecole Polytechnique Fédérale de Lausanne,CRPP-PPB,CH-1015 Lausanne, Switzerland

1. Introduction. The topologic study of a stochastic magnetic field is investigated by the tracing of magnetic field lines using a symplectic symmetric map. This method allows to study statistical properties of the dynamics of the system such as the number of iterations for open field lines or the local diffusion coefficient. We study the effect of the **D**ynamic **E**rgodic **D**ivertor (DED) [1] on a **TEXTOR** equilibrium computed with the VMEC code. The magnetic field of the DED is computed using the Biot-Savart law applied to the superposition of sets of current carrying filaments.

2. The Mapping Method. If we invoke the condition $\nabla \cdot \mathbf{B} \equiv 0$, we can write in a general way the magnetic field $\mathbf{B}$ as

$$\mathbf{B} = \nabla\Psi \times \nabla\theta^* + \nabla v \times \nabla\chi(\Psi, \theta^*, v)$$

where Ψ and χ constitute a measure of the toroidal and poloidal flux, respectively, and θ^* is a poloidal coordinate [2]. In this case, the magnetic field lines become

$$\frac{d\theta^*}{dv} = \frac{\partial\chi}{\partial\Psi}, \quad \frac{d\Psi}{dv} = -\frac{\partial\chi}{\partial\theta^*} \tag{1}$$

from which we recognize the Hamiltonian equations with $\chi \leftrightarrow H$, $(\Psi, \theta^*) \leftrightarrow (p, q)$ and $v \leftrightarrow t$. The Hamiltonian χ can be written in the form

$$\chi(\Psi, \theta^*, v) = \chi_o(\Psi) + \chi_1(\Psi, \theta^*, v)$$

where χ_o is the contribution from the unperturbed equilibrium such that $\frac{d\chi_o}{d\Psi} = \iota(\Psi)$, and ι is the rotational transform. The calculation of the Hamiltonian and the canonical coordinates are performed numerically [2].

If we examine now the intersections of the trajectory with the plane (Ψ, θ^*) at a cross section at $v = constant$, the equations of motion can be described by a map. This map should satisfy the same properties as the Hamiltonian equations (1), namely it must be symplectic and symmetric with respect to the toroidal angle [3, 4]

$$\hat{T}_+(J_n, \theta_n) = \begin{cases} J_{n+o} & = J_n + \frac{\epsilon}{2} f(J_n, \theta_{n+o}), \\ \theta_{n+o} & = \theta_n + \frac{\epsilon}{2} g(J_n, \theta_{n+o}) \; (mod\, 2\pi) \end{cases} \tag{2a}$$

$$\hat{T}_\iota(J_{n+o},\theta_{n+o}) = \begin{cases} J_{n+1-o} & = J_{n+o}, \\ \theta_{n+1-o} & = \theta_{n+o} + \frac{2\pi}{L}\iota(J_{n+1-o})\ (mod\ 2\pi) \end{cases} \tag{2b}$$

$$\hat{T}_-(J_{n+1-o},\theta_{n+1-o}) = \begin{cases} J_{n+1} & = J_{n+1-o} + \frac{\epsilon}{2}f(J_{n+1},\theta_{n+1-o}), \\ \theta_{n+1} & = \theta_{n+1-o} + \frac{\epsilon}{2}g(J_{n+1},\theta_{n+1-o})\ (mod\ 2\pi) \end{cases} \tag{2c}$$

where $J = \Psi$ can be associated with a radial coordinate and $\theta = \theta^*$. The functions f and g are defined by

$$f(J,\theta) = -\int_0^{2\pi/L} dv \frac{\partial \chi_1}{\partial \theta^*}(\Psi,\theta^*,v)\Big|_{\Psi=J,\,\theta^*=\theta+\iota(\Psi)v},\ g(J,\theta) = -\int_0^{\theta} d\theta' \frac{\partial f}{\partial J}(J,\theta'). \tag{3}$$

The equations (2a), (2b) and (2c) define a symplectic symmetric map and equation (3) guarantees the preservation of area.

3. Numerical Results. The calculation for the TEXTOR equilibrium has been based on the following data: the plasma current $I_p = 356\ kA$, the major radius $R = 1.75\ m$, the minor radius $a = 0.46\ m$, the resonant $\iota = 1/3$ is located at $r = 0.43\ m$. The DED coils are aligned to approximately coincide with the pitch of the field lines on the $\iota = 1/3$ rational surface [1]. The coil arrangement consists of 16 helical conductors carrying a current I_j, $j = 1,...16$. We model the current I_j as a simple trigonometric function,$I_j = cc * I_0 sin((j-1)\varphi + \pi/4t)$ with $I_0 = 7.5 kA, \varphi = \pi/4$ for the case $m/n = 6/2$ and $I_0 = 3.75\ kA, \varphi = \pi/8$ for the case $m/n = 3/1$. Consequently, the perturbed fields generated by the DED coils have a structure dominated by the $m/n = 6/2$ or $m/n = 3/1$ component where m (n) is the poloidal (toroidal) mode number.

In the Fig. 1a, we see the Poincaré section for the case $m/n = 6/2$ with $cc = 0.2$ and the formation of magnetic islands (six on the $\iota = 1/3$ surface), stochastic regions and KAM barriers. The value $J/J_{max} = 1$ corresponds to the boundary of the plasma. Fig. 1b is the same but with the configuration $m/n = 3/1$ for the perturbation.

We can study the angular dependence of the number of iterations N_ϕ for $J/J_{max} = constant$ in the mapping for open field lines while they reach the boundary of the plasma. Fig. 2a represents N_ϕ for the case $m/n = 6/2$ with $cc = 0.4$ and $J/J_{max} = 0.93$ and Fig. 2b represents the case $m/n = 3/1$, $cc = 0.4$ and $J/J_{max} = 0.95$. We show clearly a fractal structure of this quantity. It is due to the fact that the dynamics of the system is self-similar.

We expect that the radial diffusion is normal for few iterations and so the mean square radial displacement of field lines should be linear with the number of iterations. In this case, we can introduce a local diffusion coefficient D_{FL}. The profile of D_{FL} as a function of J/J_{max} is shown in Fig. 3a for the case $m/n = 6/2$ for different values of cc. We see clearly that D_{FL} increases until the value $J/J_{max} \sim 0.95$ and ~ 0.90 for the cases

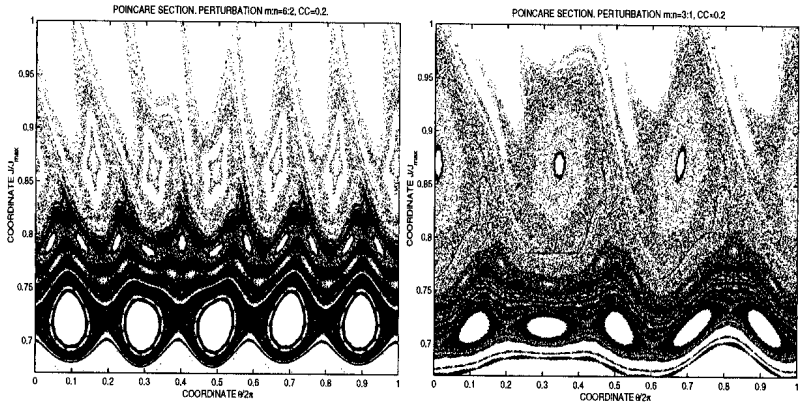

Figure 1: a) Poincaré section in $(\theta, J/J_{max})$ coordinates for the perturbation $m/n = 6/2$ with $cc = 0.2$ (left) and b) for the case $m/n = 3/1$ with $cc = 0.2$ (right).

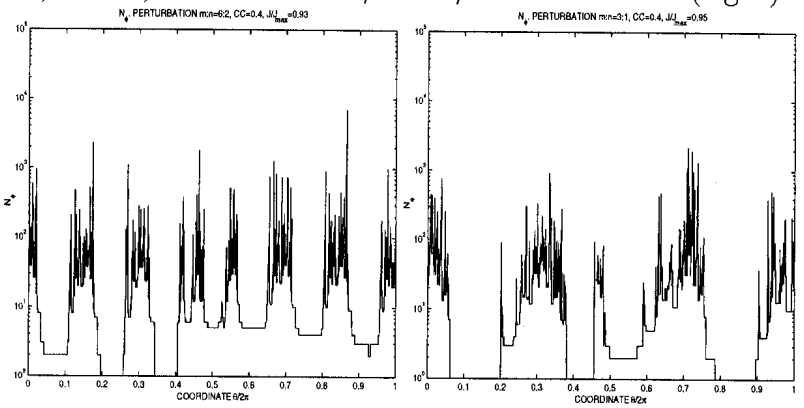

Figure 2: a) Number of iterations N_ϕ for open field lines for the perturbation $m/n = 6/2$ and $cc = 0.4$ for $J/J_{max} = 0.93$ (left) and b) for the case $m/n = 3/1$ with $cc = 0.4$ and $J/J_{max} = 0.95$ (right).

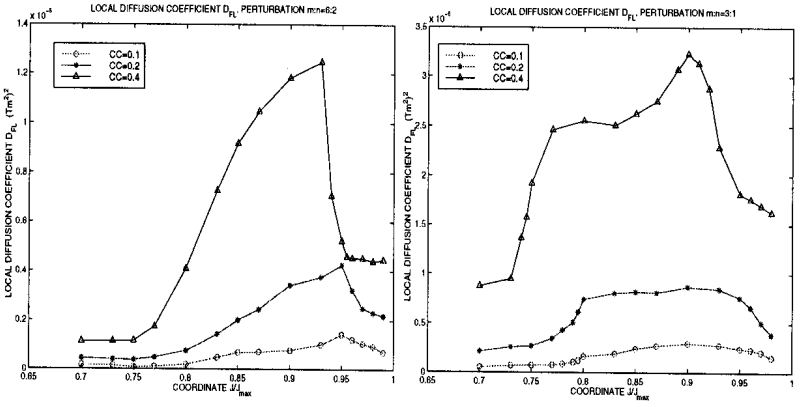

Figure 3: a) Profile of the local diffusion coefficient D_{FL} as a function of J/J_{max} for the perturbation $m/n = 6/2$ for different values of cc (left) and b) for the case $m/n = 3/1$ (right) (Circles: $cc = 0.1$. Stars: $cc = 0.2$. Triangles: $cc = 0.4$) .

$m/n = 6/2$ and $m/n = 3/1$ (Fig. 3b), respectively. After this value, the laminar process dominates on the diffusion and the coefficient D_{FL} decreases quickly.

4. Conclusion. We have studied the magnetic topology of the DED on a TEXTOR equilibrium by using a symplectic symmetric map. This map is general and the only restriction imposed is that the unperturbed equilibrium state should have nested magnetic flux surfaces. We can use this method to study more complicated system such as Stellarators. Concerning the numerical results, we have seen that the DED creates stochastic regions and the Poincaré section constitutes a very complicated KAM system: formation of magnetic islands, stochastic regions, KAM barriers, etc.. Concerning the statistical properties of the system, we have shown there exists a fractal structure for the number of iterations for open field lines. This is due to the self-similar properties. Finally, from the study of the profile of the local diffusion, we have seen that the laminar region is pushed inwards into the plasma as the structure of the perturbation is changed.

Acknowledgments. We acknowledge useful discussions with Dr. S. S. Abdullaev and we thank Dr. S.P. Hirshman for providing us with the VMEC code. This work was partially sponsored by the Fonds National Suisse de la Recherche Scientifique and by Euratom.

References

[1] Finken K H *et al Fusion Engineering and Design* **37** 1997

[2] Fischer O and Cooper W A accepted for publication in *Plasma Phys. and Controlled Fusion* 1997

[3] Fischer O and Cooper W A accepted for publication in *Plasma Phys. Reports* 1998

[4] Abdullaev S S, Finken K H and Spatschek K H submitted to *Phys. Plasmas* 1998

The Local Stability in 5-period Linked-Mirror Stellarators.

M.Yu.Isaev, W.A.Cooper*, V.D.Shafranov

Nuclear Fusion Institute, RRC "Kurchatov Institute", Moscow, Russia

* *Centre de Recherches en Physique de Plasmas, Association Euratom - Confédération Suisse, Ecole Polytechnique Fédérale de Lausanne, Lausanne, Switzerland*

1. Introduction

The comparison of different types of stellarators which can help identify the optimal system constitutes an important task of plasma theory. In this work, we explore the local stability limit which is defined by the value of $\beta = 2 < p > / < B^2 >$, where $< p >$ and $< B^2 >$ correspond to the volume averaged plasma pressure and volume averaged magnetic energy density, respectively. We look for the configurations which are stable with respect to the Mercier and ballooning modes at the maximal value of β.

Our main tools will be the three dimensional (3D) ideal magnetohydrodynamic VMEC equilibrium code (fixed boundary version) [1] and TERPSICHORE stability code [2]. Here the magnetic configurations are defined via the spectrum of the Fourier modes in the cylindrical coordinates of the boundary magnetic surface.

The TERPSICHORE code performs the transition to the special Boozer magnetic coordinates [3]. The information about the spectrum of the magnetic field strength in Boozer coordinates can predict the behaviour of a given configuration from the view point of the neoclassical losses. If this strength depends on only one variable of the Boozer coordinates on each magnetic surface (a sort of special symmetry, quasi-symmetry), the neoclassical drift equations in such magnetic configurations satisfy an additional invariant of the motion and the neoclassical losses should thus be lower. The accuracy of the quasi-symmetry condition in different systems can be characterised by the ratio X of the dominant symmetric Fourier component of the magnetic field strength in Boozer coordinates to the maximal Fourier component that violates the symmetry evaluated at the plasma boundary.

Here we are interested in 5-period systems with nonplanar magnetic axes. This allows us the possibility to compare the results that were considered for WVII-X [4]. Among the different 5-period stellarators we select Heliac-like and Helias-like cases with the dominant toroidal Fourier component of the magnetic spectra per period (0,1). We identify these systems as Linked-Mirror Stellarators (LMS).

It was shown in [5], that the 4-period LMS Heliac can achieve a limiting $\beta = 3\%$ value with respect to Mercier and ballooning modes. Numerical investigations of LMS configurations were done for Helias-like systems only in [6].

Ballooning modes that are strongly localised impose the most restrictive limits in various stellarator configurations. In this article, we attempt to increase the β value by optimising the plasma boundary shape conserving the type of symmetry. Our article consists of two main sections where we describe the local stability for linked-mirror Helias (Sec.II) and for Heliac (Sec.III) systems.

II. The Local Stability of 5-period Linked-Mirror Helias

The "Helias" magnetic configuration corresponds to the system in which the magnetic surface cross-sections lags behind the principal normal with respect to the magnetic axis.

In Helias systems, the flux surface cross sectional shape is vertically elongated at the beginning of the system period and horizontally elongated at the midperiod position. Fig. 1a displays three magnetic surface cross sections for the 5-period LMS Helias at the beginning, at one quarter and at the middle of the system period. The rotational transform ι profile varies from 1.2 on axis to 1.29 at the edge. The dominant Fourier amplitudes of B^2 in Boozer coordinates for this configuration are shown in Fig. 2a and has $X \simeq 4.4$. The Mercier criterion and the ballooning eigenvalues for this system are displayed in Fig. 3a and 3b, respectively, for a case with nearly parabolic pressure profile at $\beta \simeq 6\%$. The Mercier instability near the edge is localised about the $\iota = 5/4$ resonant surface. The region of ballooning instability concentrates in the outer 2/3 of the plasma volume. A peaked pressure profile of the form $p(s) = 0.2p_0[3(1-s)^2 + 2(1-s)^3]$ allows stability to local modes to be achieved at $\beta \geq 5.1\%$, where s is a radial variable proportional to the enclosed toroidal magnetic flux.

III. The Local Stability of 5-period Linked-Mirror Heliac

We mean by the term "Heliac" the configuration where the magnetic surface cross-section rotates simultaneously with the principal normal with respect to the magnetic axis. In Heliac systems, the flux surface cross sectional shape is vertically elongated at the beginning and at the middle of the system period. Fig. 1b demonstrates the corresponding three magnetic surface cross-sections of Fig. 1a for the 5-period LMS Heliac. This system was obtained from the 4-period LMS Heliac [5], using the optimisation towards ballooning stability.

We choose to vary the VMEC input boundary modes that describe the plasma shape as the means for increasing the ballooning stability limit. Thus, we do not impose constraints or restrictions on the magnetic field strength as we vary the plasma shaping. As a result of this optimisation, we obtain a Heliac-like magnetic configuration with large triangularity, elongation and bumpiness. The rotational transform ι changes from 2.07 to 2.46. The magnetic field spectrum (Fig.2b) has the ratio X equals to 2.5.

The β limit with respect to ballooning modes equals to 5.91% and with respect to Mercier modes is a little higher - 6.15%, consistent with results shown in Fig. 3a and 3b. The ballooning instability is supressed by the weak shear and significant magnetic well which is a characteristic feature of the Heliac-like systems. The calculations were performed with a prescribed almost parabolic plasma pressure profile.

IV. Conclusions

We have investigated the local ideal MHD stability properties of a 5-period quasisymmetric Linked-Mirror stellarator with the TERPSICHORE code. Our aim was to numerically optimise the β limit with respect to Mercier and ballooning stability. We have also tried to control the linked-mirror symmetry with moderate levels of accuracy.

As a result, two linked-mirror configurations were found. The Heliac-like LMS stellarator is stable with respect to Mercier modes up to $\beta \sim 6.15\%$ and ballooning modes impose a more restrictive limit, $\beta \simeq 5.9\%$. The LMS Helias is unstable to local modes at these values of β with a parabolic pressure profile. However, with a peaked profile it can achieve a limiting $\beta \geq 5.1\%$.

These calculations illustrate the possibility to improve the MHD stability limits and

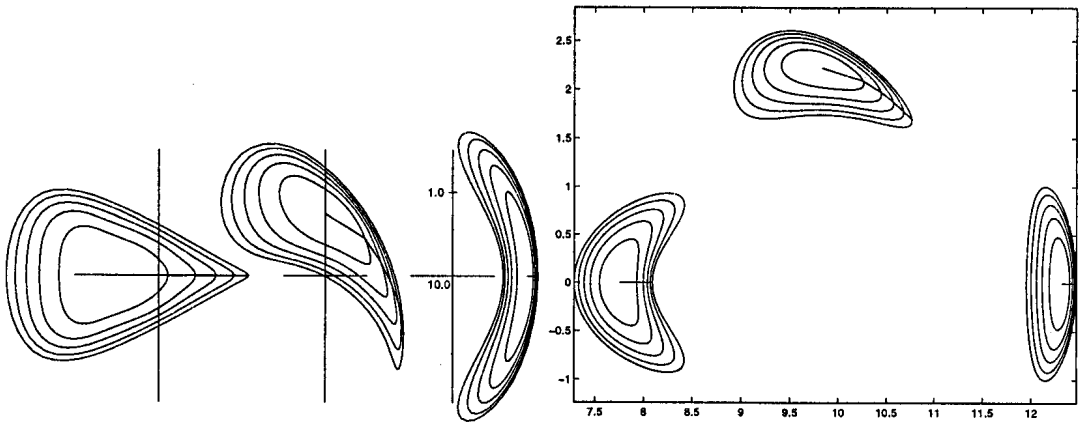

Fig. 1. (a) Magnetic flux surface cross-sections for a 5-period LMS Helias (left) and (b) Heliac (right) configuration at the beginning, at one quarter and at the middle of the period.

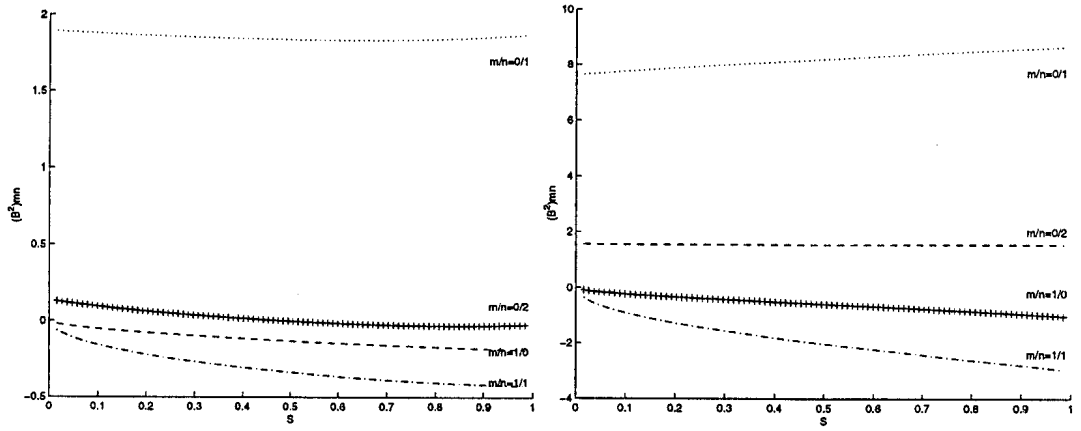

Fig. 2. The four main Fourier components of the magnetic field spectrum for the 5-period (a) LMS Helias (left) and (b) Heliac (right) configurations versus the radial variable s (proportional to the enclosed toroidal magnetic flux).

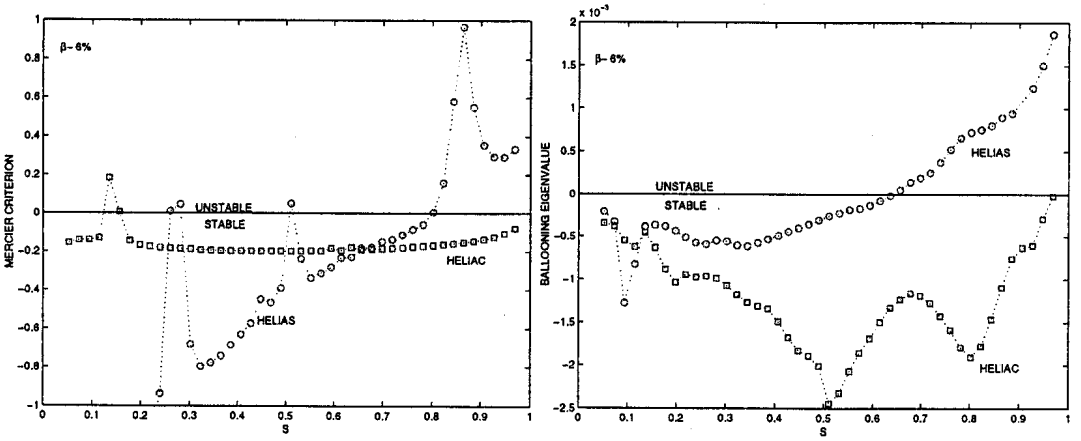

Fig. 3. (a) The Mercier criterion (left) and (b) the ballooning eigenvalues (right) versus the radial variable s for the 5-period LMS Heliac (squares) and Helias (circles) configurations at $\beta = 6\%$ with a nearly parabolic pressure profile given by $p(s) = p_0[11(1-s^2) + 9(1-s)^2]/20$. The most unstable ballooning eigenvalues lie on field lines $\alpha = \pi/10$ in the Heliac configuration and $\alpha = \pi/5$ in the Helias configuration. These field lines cross the outside edge of each flux surface at the quarter period (tip of the tear shape cross-section in Fig. 1b) and at the half period (tip of the triangular cross-section in Fig. 1a), respectively.

the transport properties of conventional Heliac systems (TJ-II [7], H-1 [8]). This improvement can be achieved by varying the modulation of the cross-sections along the toroidal angle.

Future work can be directed towards the investigation of global stability and transport properties of LMS configurations both Heliac-like and Helias-like types.

Acknowledgements

We thank Prof. F. Troyon for supporting this work and Dr. S.P. Hirshman for providing us the VMEC. This work is partially sponsored by the Fonds National Suisse de la Recherche Scientifique and by EURATOM, and by Russian Foundation for Fundamental Research, project No 97-02-17695.

References

[1] Hirshman S.P., Betancourt O.// J. Comput. Phys. **96**, 99(1991).

[2] Anderson D.V., Cooper W.A., Gruber R., Merazzi S., Schwenn U.// Scientific Computing on Supercomputers II, Plenum Press, New York, 1990, p.159; Cooper W.A. // Plasma Phys. Contr. Fusion **34**, 1011(1992).

[3] Boozer A.// Phys Fluids. **23**, 904(1980).

[4] Nührenberg J., Zille R.// Proc. of 2 Workshop on Wendelstein VII-X, Schloss Ringberg, Germany, (Commission of the European Communities, Directorate-General XII, F. Rau and G.G. Leota, editors, Brussels), 17(1988).

[5] Isaev M.Yu., Cooper W.A., Mikhailov M.I., Shafranov V.D.// Proc. of Int. Toki Conf. (1997) in J.Plasma Fus.Res.SERIES. **1**, 66(1998).

[6] Gori S., Lotz W., Nührenberg J.// Joint Varenna-Lausanne Int. Workshop on theory of Fusion Plasmas, edited by J.W.Connor, E. Sindoni, J. Vaclavik (Societa Italiana di Fisica-Editrice Compositori, Bologna), 335(1996).

[7] Jimenez J.A., Varias A., Fraguas A.L., Alejaldre C. et al// Nucl.Fus. **37**, 467(1997).

[8] Cooper W.A., Gardner H.J.// Nucl.Fus. **34**, 729(1994).

MHD Limits in Low Aspect Ratio Tokamaks with Separatrix

S. Medvedev, L. Degtyarev, A. Martynov,
Keldysh Institute of Applied Mathematics, Russian Academy of Sciences, Moscow, Russia

L. Villard
Centre de Recherches en Physique des Plasmas, Association Euratom - Confédération Suisse, Ecole Polytechnique Fédérale de Lausanne, Switzerland

T.C. Hender
UKAEA/EURATOM Fusion Association, Culham, Abingdon, Oxon, OX14 3DB, UK

1 Introduction The low aspect ratio tokamak (spherical tokamak) is an attractive concept for future volumetric neutron sources and fusion reactors. The key advantage of this concept is the high value of stable β that follows from the theoretical Troyon-Sykes scaling [1, 2] $\beta[\%] = \beta_N I_N$, $\beta_N \simeq 4$ due to higher values of normalized current $I_N = I[MA])/(a[m]B[T])$ achievable at low aspect ratio $A = R/a$, where I is plasma current, a is plasma minor radius and B is vacuum toroidal field in the plasma center $R = R_c$.

Limiting values of $\beta = 2\int pdV/(VB^2)$ and current for the aspect ratio range from 2 to 1.2 and conventional plasma shape with elongation $\kappa = 1.6$ and triangularity $\delta = 0.3$ were studied in [3]. It was found that for plasma with an axial safety factor, $q_0 > 1$, the overall β limit is set by ballooning modes in the first stability region with $\beta_N \simeq 4$. External kink modes set the limit for normalized current. The current limit corresponded to a safety factor at the plasma boundary higher than 2 for aspect ratios lower than 1.5. Nevertheless the normalized current limit was found to increase with decreasing aspect ratio.

Recent results from START spherical tokamak [5] demonstrate values of $\beta \geq 30\%$ and $I_N \simeq 8$. The value of normalized current is close or even higher than the theoretical limit set by external kink modes. However previous computations of external mode stability were performed using the ψ_{95} magnetic surface inside the separatrix as plasma boundary.

Equilibrium and stability codes CAXE and KINX [4] were used to compute the current and β limits taking into account the separatrix at the plasma boundary. It was found that the current limit for plasma configurations close to that of START can be as high as $I_N = 16$ provided that $q_0 < 1$. The aspect ratio and current profile scans lead to more general conclusion that the maximal current value achievable at low β is reached at $q_0 < 1$ and is set by "toroidal kink" mode [6]. The maximum current value is sensitive to the plasma boundary proximity to the separatrix.

The limiting values of β against both ballooning and external kink modes were found to be consistent with the results in Ref.[3] for the case of $q_0 > 1$. A typical condition for kink mode stability at $q_0 < 1$ is that the pressure gradient is low inside the $q = 1$ surface when it lies in low shear region. However in the "advanced low q" case with very low $q_{95} < 1.2$ the $q = 1$ surface is close to the plasma boundary where the shear is higher. It leads to internal kink mode stability with finite p' on it and a possibility to get very high β values against external kink modes taking into account conducting wall stabilization. For $A = 1.2$ it gives $\beta > 100\%$ in the first ballooning stability region and stable external $n = 1$ kink mode with the wall at $a_w/a = 1.5$ position.

2 The current limit at $q_0 < 1$ A starting point of the calculations of the plasma stability was a free boundary equilibrium computed with the PF coil and plasma currents corresponding to a high-β START pulse. The plasma profiles were chosen to obtain $\beta = 31.4\%$, $\beta_p = 0.25$, $I_N = 6.9$ and $q_0 = 0.8$. This is close to the corresponding equilibrium reconstruction from TOPEOL [5], which gives separatrix parameters $A = 1.35, \kappa = 1.8, \delta = 0.55$ (Fig.1).

To deal with current driven modes series of equilibria with $\beta = 0$, and prescribed averaged toroidal current density profile $I^* = dJ/dS$ (J is toroidal current within magnetic surface and S is the toroidal cross section area) were considered. For fixed boundary equilibria with the current profiles defined by $I^* = (1-\psi)^\alpha$ and $I^* = 1-\psi^\alpha$ (ψ is normalized poloidal flux) the normalized current limit was computed for a range of α's. Fig.2 shows the limiting values against $n = 1$ modes for the START aspect ratio. For the two series of current profiles the maximal value of normalized current is reached for approximately the same value of internal inductance $l_i \simeq 0.5$ ($l_i = 2\int B_p^2\, dV/(R_c I^2)$). The maximal current value is reached for $q_0 < 1$ and is set by "toroidal" kink mode with a strong coupling of surface wave components to dominating $m = 1$ poloidal harmonic. For $l_i < 0.5$ the current limit is much lower. It is reached at $q_0 > 1$ and is set by "external" kink mode with a dominating surface wave component. Similar results were obtained for aspect ratios $A = 1.2$ and $A = 2.0$ keeping the same plasma cross section shape (Figs.3-4). In the $A = 1.35$ and $A = 1.2$ cases safety factor profiles are non monotonic ($q_{min} < q_0$) for the series with flat current profile $I^* = 1 - \psi^\alpha$ at $q_{min} < 1$. Internal $m = 1$ modes can be unstable in a narrow band around $q_0 = 1$.

There is a difference between "toroidal" and "external" kink mode sensitivity to the separatrix proximity to the plasma boundary. The stability computations were redone taking the ψ_{99} surface as the plasma boundary. The obtained current limits were close to that with separatrix at the boundary for $q_0 > 1$ but much lower for $q_0 < 1$: the maximal normalized currents for ψ_{sx} and ψ_{99} at the boundary are $I_N = 23$ and $I_N = 16$ respectively for $A = 1.2$ and $I_N = 16$ and $I_N = 9$ respectively for $A = 1.35$ ($I^* = (1-\psi)^{0.4}$). This result was verified by convergence studies.

3 The β limit at $q_0 < 1$ and high I_N As shown in the previous section the current limit for low aspect ratio tokamaks is maximum for $q_0 < 1$. The ballooning β limit for such configurations has been obtained by optimisation of the pressure profile, at all radii, to ballooning modes keeping the safety factor profile. Fig.5 shows this limit for a sequence of equilibria with current and pressure profile shapes of Fig.1 and demonstrates that the conventional scaling, $\beta_N = 4$, is valid at very low $q_{95} (\simeq 1.1)$ and with p' localised near the boundary (Fig.6).

Stability against internal and external kink modes can be achieved by making the pressure gradient vanish inside the $q = 1$ surface. However this leads to quite low β values for the high maximal current case where the $q = 1$ surface is close to the plasma boundary. A possible alternative to that is to have relatively high shear at the $q = 1$ surface to stabilize the $m = 1$ mode. Let us give two examples of the "advanced low q" equilibria of this kind. The first one corresponds to the point with the highest $\beta = 65\%$ (lowest q_0) from the Fig.5 for aspect ratio $A = 1.35$. The equilibrium is stable against $n = 1$ mode with wall position $a_w/a = 1.3$. Another one is the equilibrium with safety factor profile corresponding to $I^* = (1-\psi)^{0.4}$ at $\beta = 0$ and $q_0 = 0.86$ and ballooning marginally stable $\beta = 103\%$, $I_N = 27$, $q_{95} = 1.17$. This equilibrium is stable against $n = 1$ modes with the wall at $a_w/a = 1.5$.

4 Conclusions The obtained results lead to a conclusion that the current limit is set by "toroidal" kink modes. The maximal normalized current value is reached for $q_0 < 1$ and is especially high for low aspect ratio provided that the separatrix is at the plasma boundary.

The ballooning β limit follows the conventional scaling with $\beta_N \simeq 4$, even for $q_0 < 1$ equilibria with very low q_{95}. Maximal stable β is reached for the "advanced low q" configurations with $q_{95} < 1.2$ when the shear is high at the $q = 1$ surface and taking into account wall stabilization.

This paper has demonstrated that very high β is possible at tight A, in the first stability regime. Preliminary studies show in the second stability regime, for $A = 1.4$, that high bootstrap current fraction cases ($\geq 90\%$) are possible with $\beta \simeq 50\%$, which are stable to low-n modes with a wall at $1.2a$. The influence of the separatrix on these second stability results is currently under investigation.

Acknowledgement This work was partly supported by the Swiss National Science Foundation. The UKAEA author was jointly funded by the UK Department of Trade and Industry and EURATOM.

References

[1] F.Troyon, R.Gruber, H.Saurenmann, S.Semenzato and S.Succi, *Plasma Phys. and Contr. Fusion* **26**(1984)209.

[2] A.Sykes, M.Turner, S.Patel, *Proc. of the 11th Europ. Conf. on Contr. Fusion and Plasma Phys.* **2**(1983)363.

[3] S.Bespoludennov, L.Degtyarev, S.Medvedev, *Sov. J. Plasma Phys.* **12**(1986)771

[4] L.Degtyarev, A.Martynov, S.Medvedev, F.Troyon, L.Villard, R.Gruber, *Comput. Phys. Comm.* **103**(1997)10

[5] M.Gryaznevich, T.C.Hender, M.P.S.Nightingale *et al.*, *Proc. of the 24th Europ. Conf. on Contr. Fusion and Plasma Phys.* **21A** Part I (1997)245

[6] A.D.Turnbull, F.Troyon, *Nuclear Fusion* **29**(1989)1887

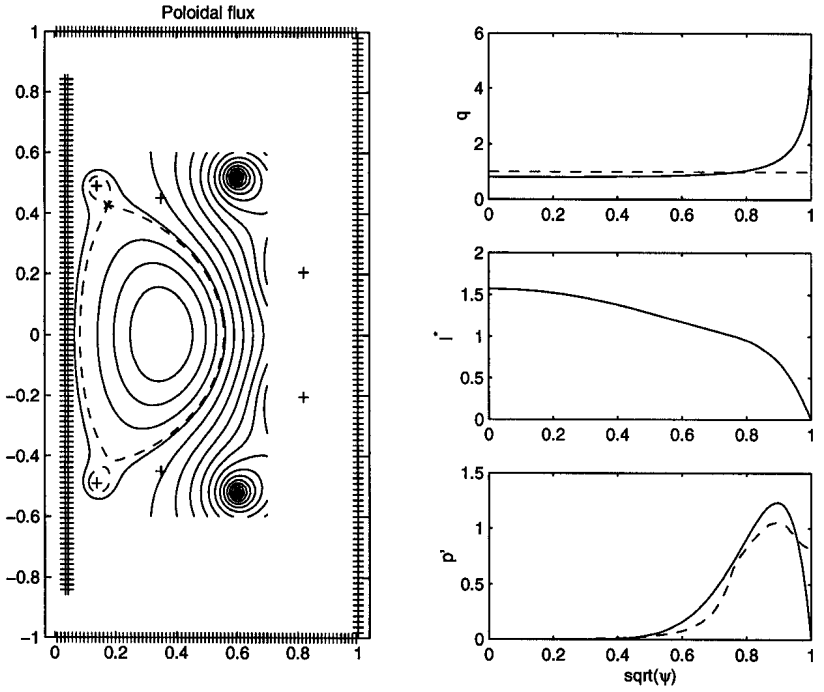

Fig.1
Free boundary equilibrium poloidal flux contours and plasma profiles. $\beta = 31.4\%$, $\beta_p = 0.25$, $I_N = 6.9$, $l_i = 0.6$, $q_0 = 0.8$, $q_{95} = 2.7$. *Ballooning marginally stable pressure gradient is shown by dashed line*

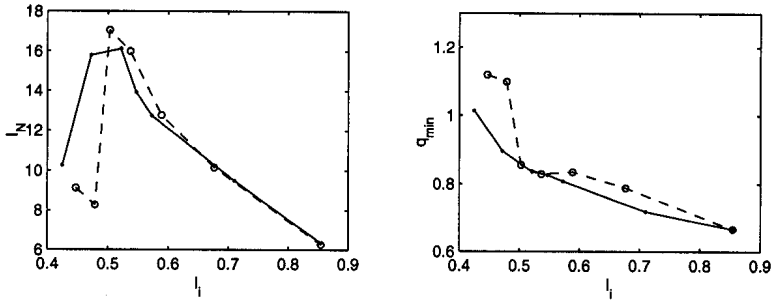

Fig.2 Limiting values of normalized current and minimal values of safety factor vs internal inductance in the equilibrium series with $I^* = (1-\psi)^\alpha$ (solid line) and $I^* = 1-\psi^\alpha$ (dashed line). $A = 1.35$

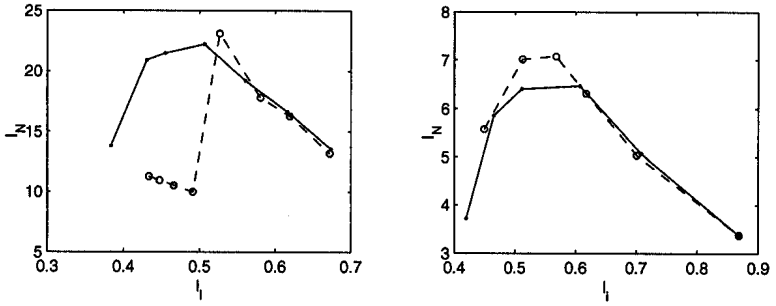

Fig.3-4 Limiting values of normalized current for $A = 1.2$ (left) and $A = 2.0$ (right)

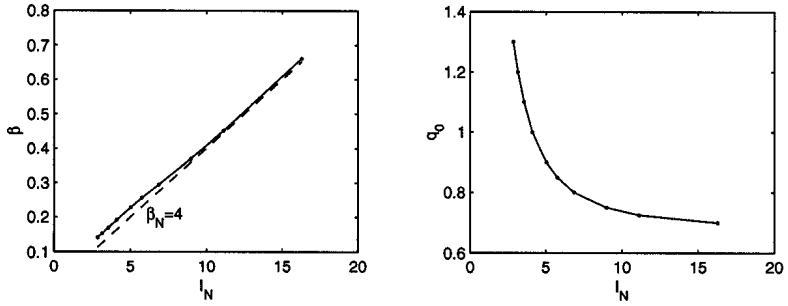

Fig.5 Limiting values of ballooning stable β in equilibria with different q_0. $A = 1.35$

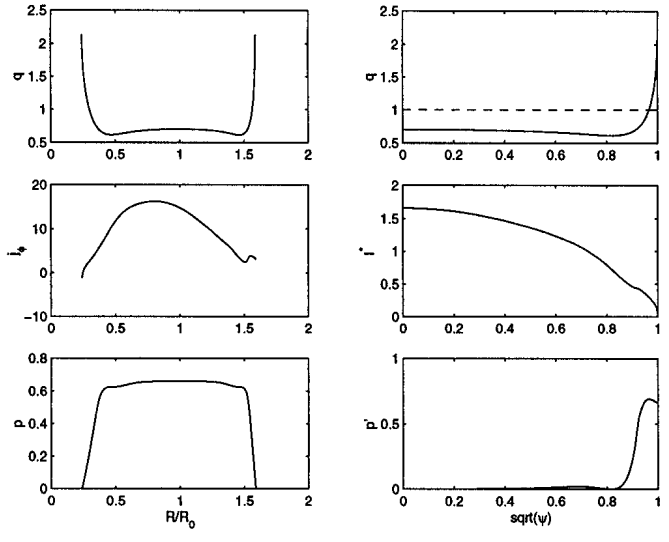

Fig.6 Plasma profiles for "advanced low q" equilibrium. $\beta = 65.5\%$, $\beta_p = 0.10$, $I_N = 16.1$, $l_i = 0.67$, $q_0 = 0.7$, $q_{95} = 1.12$.